LOW TEMPERATURE FORMATION OF ALUMINUM-CARBONATED CALCIUM SILICATE INTERPENETRATING PHASE COMPOSITES

By

TERENCE EDWARD WHALEN

A dissertation submitted to the

Graduate School-New Brunswick

Rutgers, The State University of New Jersey

In partial fulfillment of the requirements

For the degree of

Doctor of Philosophy

Graduate Program in Materials Science and Engineering

Written under the direction of

Professor Richard E. Riman

And approved by

_____

_____

_____

_____

New Brunswick, New Jersey

October, 2015

ABSTRACT OF THE DISSERTATION

Low Temperature Formation of Aluminum-Carbonated Calcium Silicate Interpenetrating Phase Composites

By TERENCE EDWARD WHALEN

Dissertation Director:

Professor Richard E. Riman

A novel, low temperature (<90˚C) process for the formation of an interpenetrating phase composite (IPC) of aluminum and carbonated calcium silicate ($CaSiO_3$) was developed. The key enabling process steps were Infiltration and subsequent hydrothermal liquid phase densification of $CaSiO_3$ in the pores of an aluminum foam. $CaSiO_3$ suspension flow was enhanced by pH adjustment and addition of a sodium polyacrylate dispersant, allowing for high solids content (58 vol%) suspensions to be used. The $CaSiO_3$ infiltrated into the aluminum foam achieved 65% relative density, comparable to control $CaSiO_3$ samples. Carbonation of the $CaSiO_3$ was conducted within a pressure steamer at 90˚C and 20psig CO_2. Extent of carbonation of the infiltrated $CaSiO_3$ was determined from mass gain, x-ray diffraction, and thermal

gravimetric analysis and averaged about 50%, comparable to control $CaSiO_3$ samples. The final bulk density of the IPC was 2.2 g/cm^3. Compression strength of the IPC exceeded that of the aluminum foam and carbonated $CaSiO_3$, greater than 110 MPa. Stress was resisted after initial failure for large strains by the IPC. These properties place the formed composite in a unique area of infiltrated Al IPC property space.

No evidence for chemical interaction between the infiltrated $CaSiO_3$ and Al foam was found. Rather, adhesion between the component-materials was determined to be limited to mechanical interlock between $CaSiO_3$ particulate and surface features of the Al foam. Surface modification of the Al foam via zeolite coating, anodizing and HCl etching was conducted to change the surface morphology of the Al. Zeolite coatings produced 50 µm thick coatings with pores ranging from 0.01-10 µm. Anodic oxide coatings produced shallow dimpling and cracking on the Al foam surface. HCl etching created muli-scale pitting with features ranging from 0.01-100 µm. IPCs were formed with the surface modified Al foams and tested in compression. Failure analysis of the Al-carbonated $CaSiO_3$ interface showed that increasing Al surface roughness led to separation between the bulk carbonated $CaSiO_3$ and the entrapped carbonated $CaSiO_3$ particles. This change in interface microstructure and failure behavior did not induce significant changes in compressive strength.

Dedication

To Stephanie, without your love, support, and patience I never would have accomplished this.

To my parents, I could not imagine a better upbringing, and whenever I feel lost, I need only look to your example for guidance.

Acknowledgements

The past five years have been tremendously valuable not only in my development as a scientist, but also in personal growth. I have received support and encouragement from many people. To all my colleagues and friends, you know who you are and you have my gratitude for helping me through this challenge.

Foremost, I thank my advisor, Dr. Richard E. Riman. He provided unwavering support and encouragement, all the while allowing me the space and freedom to choose my own research path. His ability to always see the positive, even in the face of a series of negative results, was invaluable. At the lowest points, when my confidence in being able to complete the work waned, he never failed to lift me up and push me forward.

Acknowledgements to the Army Research Laboratories for funding the work. In particular, thanks to Marc Pepi for his enthusiasm and support in generating exposure for the technology. It would be tough to find as patient and pleasant company to sit through hours of mechanical testing with.

Thanks to the post-docs and faculty researchers in the Riman research group. Their collective expertise meant I never had to go far to get help. To my officemates, thanks for all the great discussions, academic and otherwise. Working through all of our harebrained ideas was just as enriching as, and far more entertaining than any of the coursework.

Finally, thanks to all the departmental support staff. Working towards a PhD would have been doubly difficult without their aid in handling all the required paperwork.

Table of Contents

List of Tables

List of Figures

1. Introduction

1.1 Motivation

Concern over the sustainability of the planet has been an issue for many decades, but in more recent years it has become apparent across most of society.[1] Sustainability means the ability to maintain a certain level, and when used in reference to the planet implies that as humanity continues to develop it must also seek to mitigate large-scale change resulting from its activities.[2] Understanding what affects the global ecosystem requires acknowledgement that nearly every facet of society contributes in an interconnected way.[3] Clearly, there are many factors to consider, and all must be addressed to some extent for sustainability to be reached.

Perhaps the most prominent and urgent sustainability consideration is climate change. Substantial research has been conducted regarding this issue and the leading cause of global warming is attributed to excess carbon dioxide (CO_2) in the atmosphere.[4–6] Systematic tracking of the amount of CO_2 in the atmosphere since 1958 and measurements from ice cores detailing earlier concentrations have revealed a rapidly increasing trend since ~1750.[7] This rapid change is predominantly attributable to human activities, with fossil fuel burning being the majority culprit.[8] Recent United States Environmental Protection Agency (EPA) reports break down the source of human generated CO_2 accordingly: 38% electricity, 32% transportation, 14% industry, 9% residential & commercial, and 6% other.[9] The EPA has consequently pushed for government-sponsored strategies for emission reduction, focusing on increasing energy

efficiency, energy conservation, alternative fuel utilization, and carbon capture and sequestration.

The US military has similarly begun to focus more attention towards increasing sustainability. Early perspective was primarily focused on maintaining combat effectiveness with reduction in resources.[10] More recently, the Department of Defense has taken a broader stance, looking to shrink its footprint, with reduction of CO_2 emissions as a key goal.[11] Much of the focus has been on conservation of energy by increasing logistics efficiencies, but technological solutions that may help mitigate energy demand and CO_2 emissions are being funded as well. For instance, reclamation of energy from waste on forward operating bases (FOBs) is being actively researched and implemented.[12]

Another research initiative associated with the sustainability goal is to improve or replace structural materials on FOBs with lower CO_2 emitting materials. Concrete is a mixture of large and small aggregate such as pebbles and sand with a hydraulic binder. It is used extensively on larger FOBs, both in the form of precast standoff barriers and cast-in-place structural components, and is thus a good target for replacement. The binding component of concrete is cement, which has a CO_2 intensive production pathway with about a ton of CO_2 emitted per ton of cement produced.[13] On a global scale, cement production contributes about 5% of man-made CO_2 emissions.[14] Clearly substitution of the cement in concrete with a less environmentally impactful material fits well with the sustainability goal.

Substitute materials should also improve upon FOB structural material properties. Consider standoff barriers which are intended to protect from projectiles and blasts. Improvement may come in many forms, such as providing the same compressive strength at comparatively smaller size. Increased ductility is also a target property for structural materials subject to damaging events. These properties are often at odds with each other, such that increasing one leads to the reduction of the other in a monolithic material. As such, replacement materials will need to be composite structures to attain multiple contrasting properties.

1.2 Composites

A composite, by definition, is a material made up of two or more distinct parts. In the realm of materials engineering, the purpose of combining different component-materials is to attain a property that a single material cannot provide. The concept was illustrated by Ashby and Brécht in a schematic depicting the possible attainable properties from the combination of two materials. In Fig. 1.1,[15] (A) represents an ideal scenario where each base material provides its best property to the composite. (B) is the ideal rule of mixtures combination where the resultant behavior is an average of the parent material properties. (C) denotes combinations that lie below the rule of mixtures prediction, and (D) is the worst case scenario, in which the beneficial properties of both materials are lost in the composite material.

Surveying a large number of materials and composites based on two chosen properties allows for the creation of a materials-property chart.[16] This visualization of

property relations is helpful in finding areas of property pace that cannot be satisfied by a known material or composite. These empty areas might be filled by a composite comprised of combinations of the materials bordering them.(Fig. 1.2)

In Figure 1.2, there are significant gaps in property space that might be attainable by a novel composite material. Low density materials (foams) can be filled via its pores with a high stiffness material (ceramics). The ideal case would suggest the best properties of both would be present, resulting in a composite with lower density than the bulk ceramic, while maintaining a high elastic modulus. In reality, this scenario may not be feasible, yet a small shift towards lower density without much sacrifice in strength could nonetheless be beneficial.

Along with the choice of component-materials, the volume fraction, connectivity, and morphology of those component-materials have an important influence on the composite properties. First consider the addition of metal particles into a ceramic. In small volume fraction, the metal particles might have a small effect on the composite toughness, but not one that is nearly representative of a bulk piece of metal. For some applications this might be sufficient, but suppose the composite must have bulk properties closer to that of the metal. There will be a threshold in which the volume fraction of metal particles spread throughout the ceramic matrix has hit a critical concentration, such that there is connectivity across the matrix. At this point, the metal component-material property becomes much more apparent in the composite bulk properties.[17] Eventually, both component-materials will have equitable volume fraction. Newnham's classification is useful in visualizing the different

connectivity which component-materials may have within a composite.(Fig. 1.3)[18] Totally dispersed, discrete component-materials results in a 0-0 classification. Orientation allowing continuous contact along one dimension for each component-materials results in a 1-1 classification. Increasing continuity along the other dimensions increases to 2-2 for planar orientations and 3-3 for bi-continuous orientations. Cases also exist where the connectivity of each component-material is different, due to orientation or disparity in volume fraction.

1.3 Technical Barriers of Composite Processing

Conventional manufacture of composites require many energy intensive processing steps. Common processing conditions for composites with low connectivity (0-3) of one component-material, MMCs and CMCs, as well as equitable connectivity (3-3) of both component-materials, IPCs, will be reviewed. These conditions will be considered as technical barriers that must be overcome by a novel process in order to shift the composite manufacture paradigm.

MMCs

Various metal matrix composite (MMC) processing techniques have been developed to achieve desired properties for different applications. While the method and end goal of these manufacturing routes differ, they can nonetheless be categorized by the temperature of the matrix during processing. Liquid-phase processes, solid-phase processes, deposition techniques, and in-situ processes make up these categories.[19]

Liquid phase processes introduce molten metal into ceramic particulate. The melt is then cast into a specific shape or a billet for further manipulation. Due to the requirement of metal melting, aluminum is commonly employed at its 660˚C melting point. Other engineering metals such as iron and titanium have melting points of 1538 and 1668˚C respectively, and are thus more costly to process. In addition to high temperature, effort must be put towards ensuring good mixing and contact of the ceramic phase with the metal. Since most ceramics are not wetted by a molten alloy, wetting agents are required.[20] This is a problem for adding particulate, melt infiltration, melt oxidation, and pressure infiltration. Control is needed upon cooling to mitigate stress caused by mismatched coefficients of thermal expansion (CTEs). For example, alumina and aluminum have CTEs of ~7.3 x 10^{-6} and ~29 x 10^{-6} K^{-1}. In a melt infiltration of alumina powder by molten aluminum, the metal contracts to a much greater extent than the ceramic upon cooling, leading to large residual stresses in the composite.[21] If the rate of temperature change is too large, separation between the phases and cracking are both possible. Additionally, shrinkage of the overall material often necessitates machining in order to meet product dimensional and shape specifications.

Solid phase processes utilize mixing of metal and ceramic powders prior to consolidation. Diffusion bonding between the powders is then be carried out by heating. This requires temperatures approaching the melting point of the metal used. In the case of aluminum, temperatures over 500˚C are typically needed.[22] External pressure is usually applied, varying in magnitude and duration depending on the particular system. In a silicon carbide (SiC) and aluminum composite, 2.5 MPa pressure

was applied for 30 min in an argon atmosphere at 475˚C in order to diffusion bond the phases.[23] In another study, joining of bulk aluminum was performed at even lower temperature, but with higher pressure (10 MPa) and longer duration (3 h) to compensate.[24] Multiphase metallic systems are also utilized in which one phase is brought to a liquid state, allowing for joining of the still solid components. Again, processing costs remain high due to the need of maintaining melting temperatures and inert atmosphere.

Deposition techniques coat ceramic particles with metal. The coated particulate can then be consolidated in similar fashion to the above liquid and solid phase processing routes. Coating techniques such as electroplating, spray deposition, and chemical vapor deposition (CVD) are all used. These processes often include toxic and difficult to handle chemical precursors which represent an additional cost on top of the others already discussed. For example, titanium coatings may be deposited via decomposition of titanium chlorides.[25] The titanium chloride is passed over a reactive substrate at elevated temperatures (>1000˚C) with hydrogen gas.[26] The titanium deposits at the surface, while the chloride reacts with the flowing hydrogen. The resulting hydrochloric acid and vapor must be contained carefully.

In situ processes rely on the formation of the ceramic phase within the metal as opposed to adding it directly. Direct metal oxidation (DIMOX) is an example of an in situ process in which the oxidation of the molten metal is controlled in order to form metal oxides within the matrix. The liquid metal oxidizes rapidly with reaction product growing outward from the initial contact point. Continued oxide growth is mediated by

wicking of molten metal through the product oxide pores.[27] The process terminates when the oxide product becomes an inhibiting barrier to the molten metal. Aluminum/alumina composites have been made in this manner, with flowing oxygen atmosphere provided at temperatures of 1000-1400˚C. Processing time ranged from 3-20 h depending on required coating thickness and temperature. [28]

Each MMC process requires atmospheric control. For example, high temperature melting or diffusion bonding can create oxidation problems.[29] High vacuum or inert gas atmospheres are often employed to avoid this.[30, 31] Another difficulty lies in material shrinkage during cooling due to high coefficients of thermal expansion. Over-sized casting molds and post machining are necessary to compensate for this. Overall, conventional MMC processing requires many costly steps. High temperature, control of atmosphere, harmful chemicals, mitigation of thermally induced internal stress and shrinkage, and post-process machining are major hurdles to overcome. Adoption of novel metal ceramic processing techniques that avoid these hurdles is clearly desirable.

CMCs

Ceramic matrix composite (CMC) processing may broadly be thought of as ceramic powder consolidation. This is achieved through application of high temperatures and/or pressures, chemical reaction between the composite phases, or a mixture of the three. Some important examples within the thermal/pressure powder consolidation routes are cold pressing/sintering and hot pressing, and reaction bonding.

Chemical reaction processes include chemical vapor deposition and polymer infiltration and pyrolysis.

Cold pressing and sintering involves mixing the ceramic matrix powder with the additive phase, pressing into a shape, and then heating the sample at high temperature for densification. Sintering temperatures for ceramics are quite high, with required temperatures of 0.5-0.9 times the material's melting point. For example, alumina is commonly sintered within the range of 1400-1650˚C.[32, 33] Depending on the heating schedule, elevated temperatures must be maintained for hours. Introducing another phase into the ceramic presents a number of issues. Many metals will melt, volatilize, oxidize, or diffuse before the sintering temperature is reached, and thus are not suitable for composite processing. Second phase additives that can withstand the temperature needed for densification of the matrix must also have appropriate CTE. An additive CTE very different from that of the matrix can lead to stress concentrations and cracking.[19, 29] For example, $TiTaAl_2$ and W have a disparity in CTE's, of about $6 \times 10^{-6} K^{-1}$, which is large enough to induce cracking in the composite.[34, 35] At elevated temperature, chemical reactions between two component-materials and/or the atmosphere occurs, which also causes internal stress and cracking. Fiber/particulate pre-coating, inert atmosphere, and vacuum are commonly needed to avoid the reactions. Fibers and particulate must also be kept deagglomerated throughout the mixing steps in order to create a well dispersed composite. Also, the addition of particulate or fibers often cause the sintering process to be inhibited by causing internal stresses that counteract surface energy minimization.[36] Increases in temperature, pressure, and process time are often

necessary to combat the reduction of densification rate.[37] Shrinkage during processing makes forming net-shape and net-size products difficult, and thus post-machining is frequently necessary. This represents a significant cost, as the desirable properties of many CMCs, increased toughness and wear resistance, are inhibitors of machining.[38] Additionally, defects introduced by machining can be a source for composite failure.

Hot pressing adds pressure to the sintering step which increases the rate of densification. This in turn can lower the required temperature. Often better resultant density can be achieved in a shorter time with this method.[19] While the reduction in temperature and time are attractive, the same difficulties mentioned for cold pressing/sintering exist when adding in the second phase. The pressure applied must also be carefully controlled such that the reinforcing phase is not damaged. Damage to alumina fibers during hot isostatic pressing has been observed, especially prevalent early in the process when fibers have less contact with the surrounding matrix.[39] Breaking the fiber during hot pressing would severely reduce the fiber's tensile and crack mitigating abilities of a ceramic matrix fiber composite.

In both of the above processes, reaction of the added phase with the matrix or with the atmosphere can be deleterious to the final product. As a result, a lot of effort is put into avoiding these interfacial reactions. Reaction bonding conversely uses the reaction of the additive to the advantage of the product.[40] For example, a mix of alumina and aluminum can be densified by controlling temperature and atmosphere of the system, leading to oxidation of the aluminum. The oxidation in this case amounts to

28% volume expansion (Al to Al_2O_3) and is beneficial in terms of mitigating the shrinkage of sintering.

CVD processing for CMCs is much the same as that for MMCs. A chemical precursor is decomposed to create a vapor which yields the desired ceramic matrix coated on and in between a fiber or particulate scaffold. Temperatures required for the decomposition are usually lower than those required for conventional pressing and sintering. Unfortunately, this advantage is countered by the need to use a large volume of vapor to achieve densification as growth of the reaction product is very slow. As such, long cycle times of vapor infiltration are required resulting in increased processing costs.[25]

Polymer infiltration and pyrolysis is another chemical process that is comparatively attractive to conventional sintering due to lower temperatures. Broadly, it involves the shaping of polymer precursors, usually silicon based, followed by crosslinking and pyrolysis to yield crystalline ceramic structures. Temperatures in the 1000-1700˚C with an inert atmosphere are commonly employed.[41] Unfortunately, the technique has some critical issues that counteract the lower temperature benefit. Care must be taken to allow escape of evolved gases as internal pressure build up can lead to cracking. Also, carbon contamination from pyrolysis is difficult to avoid, resulting in lower purity products. Lastly, multiple cycles are also necessary to reduce product porosity, as each pyrolysis step has a low product yield.[42, 43]

IPCs

Interpenetrating phase composites (IPCs) are MMCs or CMCs in which the matrix and the added phase are both present and continuous along all dimensions, 3-3. The phases in IPCs are often more equal in concentration, whereas MMCs and CMCs usually have much higher matrix concentrations. In general, an IPC can be made by addition of a phase into another continuous phase or by pre-mixing of both phases such that both are continuous throughout the material upon consolidation.

The most prevalent process for IPC formation is melt infiltration.[44–46] Liquid metal is poured into a porous ceramic structure and infiltrates either by capillary pressure or with externally applied pressure. An example of this is alumina/aluminum IPCs. Initially a porous structure of alumina is formed by sintering alumina spheres. Molten aluminum is then poured into the structure.[47] Processing conditions require high temperature, 1400-1650˚C, for the ceramic sintering step, and then maintained elevated temperatures, >660˚C, during the molten metal infiltration step. Similar to MMCs, wetting of the ceramic by the metal is an issue, and without consideration can lead to separation between the component-materials. For alumina/aluminum, it was found that a 3% of Mg into the Al melt reduced the metal to ceramic contact angle from 104˚C to 84˚.[48] This allowed for reduced infiltration times and fewer pores and voids between the component-materials.

Other techniques used to form IPCs include DIMOX, Reaction Bonded Ceramics (RBC), Reactive Melt Penetration (RMP), Self-propagating High Temperature Synthesis (SHS), and Reactive Hot Pressing (RHP). In the first three methods (DIMOX, RBC, and RMP) liquid metal is added into a compact.[48–52] SHS and RHP both have the metal

already located within the compact, and utilize heating to form a metal melt in situ.[40, 53, 54] In all cases high temperatures must be used.

Paradigm for Improved Process

As seen previously, there are many different processing routes conventionally used to produce metal-ceramic composites. Within each route more differentiation occurs as the process is tailored to a specific materials system. None-the-less, some common characteristics can be associated with all the processes.

- Temperature

Conventional processing routes for metal-ceramic composites require a high temperature step for ceramic sintering, metal melting, or both depending on the manner of material addition. In the case of ceramic powder added to a metal matrix, sintering is required to strengthen the ceramic. In the case of liquid metal added to a ceramic matrix, temperatures above the melting point of the metal must be maintained for infiltration. These high variations in temperature throughout the process cause large volume changes, internal stress and cracking from mismatch of CTEs, and detrimental reactions between component-materials. Thus, high temperature processing steps are energy demanding and costly.

- Atmosphere

Conventional processing routes for metal-ceramic composites require inert atmosphere and vacuum to mitigate metal oxidation and to promote ceramic wetting by liquid metal. In the case of sintering a ceramic powder within a metal matrix,

degradation of the metal through oxidation or phase change is problematic. Control of atmosphere is necessary to mitigate this issue, with reduction of O_2 partial pressure to 10^{-10} atm or lower commonly needed.[55] In the case of liquid metal infiltration wetting of the ceramic by the metal is non-trivial. Vacuum must be maintained to prevent oxidation of the melt and additives are usually necessary to allow for wetting. Maintaining an inert atmosphere or vacuum are energy intensive and costly.

- Size and Shape

Conventional processing routes for metal-ceramic composites rarely are net-shape and net-size. Both ceramic sintering and metal melt solidification result in substantial shrinkage. In particular, the high CTE of aluminum results in 0.5mm change per meter of material when taken over a 500˚C change. Size reduction of intertwined component-materials having differing coefficients of thermal expansion leads to internal strains that cause cracking. Additionally, when complex shapes and structures are required, post-machining is needed to shape products to specification. Compensation for shrinkage and machining are expensive fabrication issues.

A process paradigm is needed for a metal-ceramic composite that follows from these technical barriers. A process with less or lower high temperature steps, that does not require inert atmosphere or vacuum, and that results in a net-size, net-shape metal-ceramic composites would be a significant advancement in terms of reduced cost and energy consumption. One such process that potentially fits the paradigm is hydrothermal liquid phase densification.

1.4 Hydrothermal Liquid Phase Densification

A novel process for low temperature hardening and solidification of ceramics, reactive hydrothermal liquid phase densification (rHLPD) was recently developed by Riman and Atakan.[56, 57] The method involves a porous, solid matrix having continuous interstitial pores which are transformed into a sintered ceramic by action of a liquid phase infiltrating medium. The density of the product is determined by the ratio of molar volumes of the porous matrix and the formed product. This concept was further extended to include gas assisted reactive hydrothermal liquid phase densification (g-rHLPD), in which a gas passed through the porous matrix delivers reactants to a wetted matrix surface.

Carbonation of $CaSiO_3$ porous compacts has been demonstrated with this method.[56, 58] The chemical reaction of $CaSiO_3$ with CO_2 forms calcium carbonate ($CaCO_3$) and silica (SiO_2), which fill some of the porosity of the initial compact and act as binders. (Eqn. 1.1)

$$CaSiO_3 + CO_2 \rightarrow CaCO_3 + SiO_2 \quad \text{(Eqn. 1.1)}$$

The process is completed at low temperatures (<100˚C) using gaseous CO_2 mixed with water vapor, and results in strong, monolithic ceramics. The carbonated solids exhibited bulk density of about 2.2 g/cm^3 and compressive strengths in the 100-200 MPa range. These values suggest this material would make a good replacement for conventional cement, which has typical density 2.2-2.5 g/cm^3 and compressive strength of 40-60 MPa after sufficient curing time.[59] As previously mentioned, the replacement material

should also have toughness and damage tolerance. The carbonated $CaSiO_3$ material does not inherently possess these qualities. Thus combining it with a low weight metal, such as aluminum (Al), may yield a novel metal-ceramic composite.

The low temperature and penetrative nature of the g-rHLPD process affords an advantage towards forming a metal-ceramic composite. Tortuous metal scaffold geometries may be infiltrated by $CaSiO_3$ suspensions, and the ceramic can subsequently be strengthened via g-rHLPD. Since the high temperatures and pressures of conventional ceramic hardening techniques are avoided, the scaffold material will not be damaged. It follows that any shape of infiltrateable metal could be used, thus also allowing the conceived process to produce net-shape, net-size products. The resulting IPCs should have the compressive strength properties of the carbonated $CaSiO_3$ and the toughness and damage tolerance of the metal. These characteristics are ideal for the replacement/improvement of structural materials on FOBs.

From the sustainability perspective a metal-ceramic IPC formed via ceramic infiltration into a metal scaffold and subsequent strengthening via g-rHLPD succeeds in two manners. First, the lower processing conditions, relative to conventional composite processing, require far less energy, and thus less CO_2 will be generated during production. Second, the mechanism of strengthening the ceramic traps CO_2 in the form of $CaCO_3$. This represents a negative CO_2 emission or a sink and is an important consideration towards reducing the impact of producing structural materials.

1.5 Objective

The aim of this dissertation is to produce and characterize an Al-carbonated $CaSiO_3$ metal-ceramic IPC using processes that fit the new fabrication paradigm. Four overlapping studies will be conducted. First, a novel process for fabrication of metal-ceramic IPCs will be covered, detailing the creation of $CaSiO_3$ suspensions, infiltration of Al foams, and carbonation of the composite. Second, the mechanical behavior and interface characteristics of the formed IPCs will be examined. Third, modification of the Al foam surface will be performed with the aim of improving the metal-ceramic interaction of the IPC. Finally, the effect of Al modification on mechanical behavior and interface characteristics of the IPC will be evaluated. From the results of these studies, conclusions will be reached on the validity of the novel process, the location of the formed IPC in Al-infiltrated IPC property space, and the ability of surface modification of the Al component to effect the IPC mechanical properties.

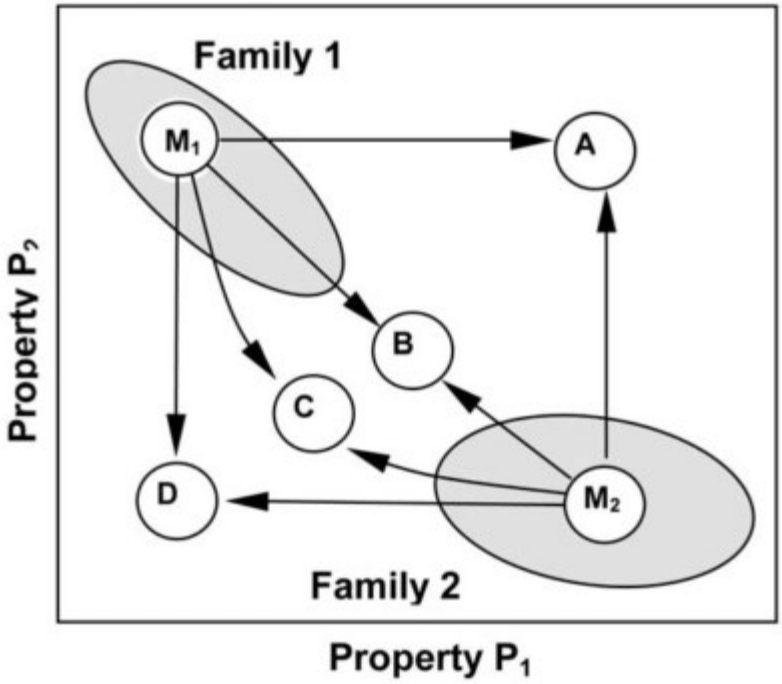

Figure 1.1. Schematic of possible property combinations attainable (A, B, C, D) from the combination of two materials (M1 and M2).[15]

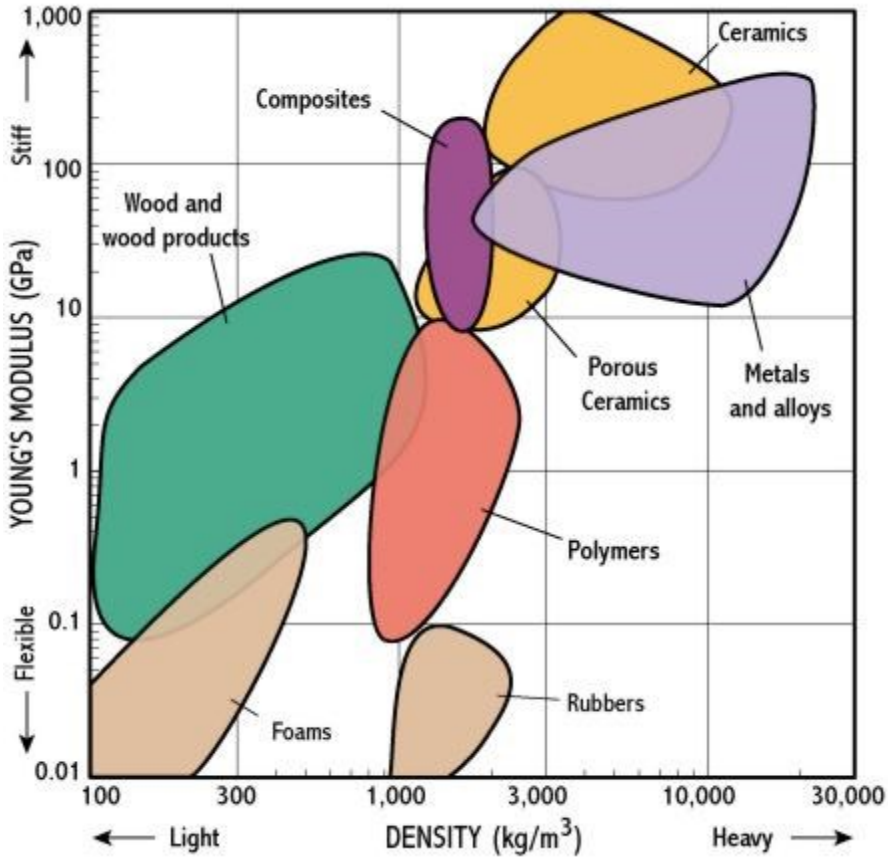

Figure 1.2. A materials property chart depicting the property space of Young's Modulus vs Density.[60]

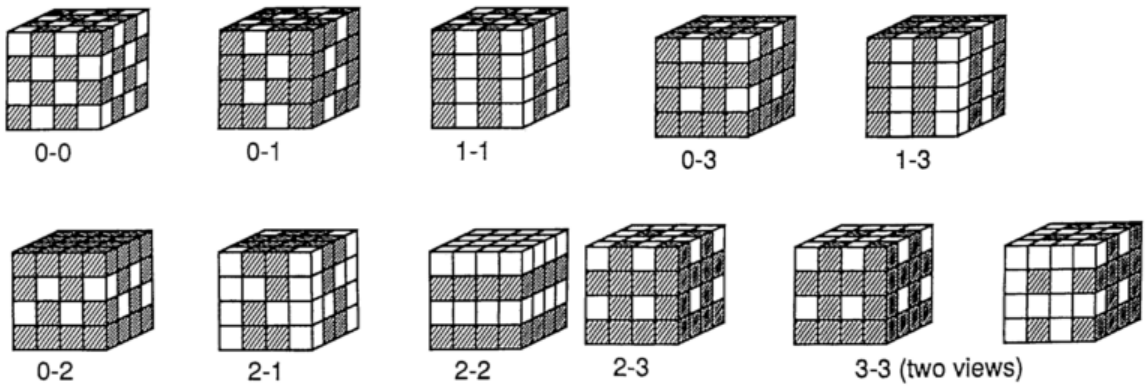

Figure 1.3. Newnham's classification depicting the various states of connectivity between two discrete phases.[44]

2. Novel Process for IPC Fabrication

2.1 Introduction

Demand for a wider variety of materials properties is ever increasing as technological challenges become more complex. Novel designs frequently call for properties that conventional materials simply cannot meet. Achieving one required design parameter is usually at the detriment of another necessary property. Composites can mitigate this tradeoff, allowing the best assets of its components to be utilized in a single bulk material.[61] Traditional approaches have predominantly focused on addition of small amounts of one material into the bulk of another, such as in metal matrix and ceramic matrix composites.[20, 62–66] These composites usually see a significant improvement of the target property, but limits on the amount of added material prevent the full extent of compositional variation to be realized. New processing approaches have enabled the components of a composite to be continuous throughout all dimensions, leading to multifunctional characteristics. Such composites are known as interpenetrating phase composites (IPCs), sometimes referred to as interpenetrating networks, or co-continuous composites. An IPC has the potential for each of its components to contribute their unique property to the macroscopic property of the composite. As a result, IPCs have shown better strength, toughness, and wear resistance compared to other composite structures.[44, 67, 68] For example, aluminum – alumina IPCs have been shown to possess 760 MPa fracture strength will also having 5.8 MPa $m^{1/2}$ fracture toughness.[47]

Many types of IPCs exist but the most ubiquitous and relevant to this work are those formed by infiltration. Within this distinction metal-ceramic IPCs, where the metal portion is Al, are considered. The Al is melted for infiltration due to its relatively lower melting point compared to the ceramic. A minimum processing temperature of 660˚C is required to reach its melting point. Atmospheric control, either vacuum or inert gas, is commonly needed to prevent oxidation of the molten metal.[37] Wetting agents are used to mediate the infiltration and even then high pressures may be needed to complete the process. Also, care must be taken regarding thermal gradients and cooling.[45] One common ceramic scaffold infiltrated by aluminum is sintered alumina. In this system, the mismatch of coefficients of thermal expansion (CTE) is large, alumina ~7.3 x 10^{-6} and aluminum ~29 x 10^{-6} K^{-1}. Delamination and stress cracking occurs if the rate of temperature change is too large.[21] Additionally, shrinkage of the entire structure must be accounted for, making complex shapes difficult to achieve without post-machining. Thus there exists a need for a fabrication process requiring sub metal melting point temperatures without the need for controlled atmosphere, wetting agents, and applied pressure.

g-rHLPD can potentially enable such a low temperature processing route without the need for controlled atmosphere, wetting agents, and applied pressure. It has been shown previously that a carbonation reaction can be carried out at low temperature (<100˚C).[69] Thus, if a powder that can be carbonated, such as $CaSiO_3$, can be placed within a metal scaffold, it can then be subsequently strengthened via g-rHLPD to form a metal-ceramic IPC. Infiltration of a $CaSiO_3$ suspension into an Al scaffold is the simplest

solution, assuming the flow properties of the suspension can be manipulated sufficiently. Suspension infiltration also fits the mild, low temperature processing paradigm.

The objective of this chapter is to detail the engineering of $CaSiO_3$ suspensions to fully infiltrate the torturous porosity of Al foams. Subsequent carbonation g-rHLPD will then be carried out to ensure that the entire proposed fabrication process is viable.

2.2 Experimental

Experimental Strategy

Suspensions of $CaSiO_3$ will be prepared. pH will be adjusted and dispersants added in order to optimize the suspensions flow behavior. Viscosity, surface charge, and green density will be monitored. Al foam will then be infiltrated with the optimized $CaSiO_3$ suspensions. Infiltration time and green density of the ceramic component will be recorded. Finally, the g-rHLPD carbonation process will be applied. Reaction completion will be observed.

Materials

Mineral wollastonite, NYAD® 400 (NYCO Minerals Inc., Willsboro, NY) was used as the $CaSiO_3$ source. Bone-dry carbon dioxide, CO_2 (CAS# 124-38-9, Airgas, Waterford, CT) was used for the g-rHLPD carbonation step. Water was filtered through a Progard® 2 and Q-guard® 1 purification system (EMD Millipore, Billerica, MA) prior to use. Potassium hydroxide, KOH (CAS# 1310-58-3, Fischer Scientific, Pittsburgh, PA) was used for pH adjustment. A 3500 molecular weight sodium polyacrylate solution, Darvan®

811(R.T. Vanderbilt Co, Inc., Norwalk, CT) was used for stabilizing the dispersion of wollastonite suspensions. 4L polypropylene wide mouth jars(# 4322T6, McMaster-Carr, Robbinsville, NJ) contained the suspensions. Aluminum foam (Duocel® Alloy 6101-T6, ERG Materials and Aerospace Corp., Emeryville, CA) of 5 PPI (pores per inch), 10 PPI and 20 PPI and relative density 10-12% served as the aluminum scaffold for infiltration. Figure 2.1 shows SEM images of the as-received $CaSiO_3$ and Al foam.

Suspension Processing

$CaSiO_3$ suspensions were created by batching powder $CaSiO_3$ into wide mouth jars and adding filtered water to attain the desired solids content. The mixture was then transferred to a jar rolling mill (#JRM, Paul O' Abbe, Little Falls, NJ) and allowed to roll for a minimum of 24 h. In the case of higher solids content suspensions, longer mixing times were allowed until the suspension appeared 'flowable' from visual inspection. Briefly, suspensions were considered 'flowable' when all surface appeared wetted and the material would uniformly flow when vibrated.

Due to the high solids content of the considered suspensions, it was difficult to mix in additives post formation. Thus new batches were formed including the desired additive as opposed to attempting to add to existing suspensions. In the case of increasing pH, KOH was added into the filtered water and mixed until completely dissolved. This pH adjusted solution was then added to the batched solids until the desired solids content was reached. Addition of dispersant was done in the same

manner. Darvan® 811 was added to the filtered water and mixed. This solution was then added to powder $CaSiO_3$ until the desired solids content was attained.

Infiltration

Aluminum foam cubes were placed within a custom made stainless steel cubic mold with dimensions 40 x 40 x 80 mm. The $CaSiO_3$ suspension was then poured over the aluminum with the assistance of a vibratory table running with approximately 1/20" amplitude at 3600 vpm (Syntron®, FMC Technologies, Inc., Houston, TX). Pouring ceased once the required suspension mass was reached. The extra height of the mold allowed for the suspension to be contained while infiltration occurred. Once the suspension head ceased to lower, additional vibration was applied to remove entrained air. The cast samples were dried at ambient conditions for 24 h then moved to a 50˚C mechanical convection oven (model# MO1440C-1, Lindberg/Blue M, Asheville, NC) for an additional 24 h. Once dried, the green composite samples were removed from the mold. Samples were cast with 4 different compositions: only $CaSiO_3$ (Pure), $CaSiO_3$ infiltrated 5 PPI Al foam (5PPI), $CaSiO_3$ infiltrated 10 PPI Al foam (10PPI), and $CaSiO_3$ infiltrated 20 PPI Al foam (20PPI).

Carbonation

The green composite samples were moved into a pressure steamer (All American #75x, Wisconsin Aluminum Foundry Co., Manitowoc, WI) with CO_2 gas input and propeller stirring to mix the CO_2 gas and water vapor. The samples sat elevated above a water immersed heating coil. A fill and purge operation was performed three times

using CO_2 to remove excess air from the reactor. Then the reactor was brought to 90˚C and 20 psig CO_2 with a propeller speed of 500 RPM and held for a minimum of 19 h. After reaction, the samples were dried at 50˚C for 24 h.

Characterization

The pH of the suspensions was recorded using an Orion 320 pH meter (Thermo Fischer Scientific, Pittsburgh, PA.). The pH meter was calibrated prior to each use with 3 point calibration using pH 4, 7, and 10 buffer solutions (Fischer Scientific, Pittsburgh, PA). Mixing via an electric mixer with stainless steel propeller (#3522K41, McMaster-Carr, Robbinsville, NJ) was applied for the lower solids content suspensions during the measurement. At the higher solids content the impeller motor could not provide enough torque. In this case, the pH probe was gently agitated to maintain suspension consistency at the tip.

Zeta potential of dilute $CaSiO_3$ suspensions was calculated via electrophoretic mobility measurements using a ZetaPALS (Brookhaven Instruments, Holtsville, NY) to infer the magnitude and sign of the particles' surface charge. The ZetaPALS used a phase analysis of light scattering to determine electrophoretic mobility. Briefly, a laser beam was passed through the dilute $CaSiO_3$ suspension, and the frequency of scattered light was compared to that of the incident light. The scattered light maintains the same frequency as the incident light when the particles are stationary. When the particles move, the scattered light frequency changes. Applying a variable electric field across the suspension causes charged particles to move, and the resulting change in frequency can be detected, giving rise to a phase change between signals. This shift can then be

related to the mobility of the particles for the known, applied electric field. With mobility, μ, known, zeta potential, ζ, can be calculated from the following expression:

$$\mu = \zeta \frac{\varepsilon}{\eta} f(\kappa a) \qquad \text{eqn. 2.1}$$

Where ε is the dielectric constant and η is the viscosity of the suspending liquid. f(κa) accounts for the electric double layer to particle ratio and the Smoluchowsky approximation was used (f(κa)=1.5) since the system was aqueous with micron sized particles. In order to more closely approximate the conditions of a high solids suspension, liquid from an 58 vol% $CaSiO_3$ suspension was extracted with 0.2 μm filter syringes(Cameo IIS, Micron Separations Inc., Westborough, MA). 10^{-3} M KNO_3 was then added as an indifferent electrolyte to stabilize the ionic concentration in order to keep the double layer of added particulate relatively constant. This solution was then used to create a 1 mg/ml $CaSiO_3$ suspension. $CaSiO_3$ powder was added with magnetic stirring. KOH was added drop-wise while continuously monitoring the suspension pH with an Orion 320 pH meter (Thermo Fischer Scientific, Pittsburgh, PA.) in order to iteratively increase pH. Effect of Darvan 811 was observed by adding in the dispersant to the extracted solution prior to adding of the $CaSiO_3$ powder. Estimated double layer thicknesses from expected ionic concentrations per addition of KOH decreased as pH was increased. This suggested that the apparent mobility and thus zeta potential should have also decreased in magnitude per increase in pH assuming no change in surface charge. Thus, an increase in zeta potential magnitude with increasing pH was associated with an increase in surface charge, overcoming any apparent reduction due to double layer compression.

Suspension rheology was measured using a Gemini Rotary Rheometer (Malvern Instruments Ltd., Worchestshire, UK) with vane and cup, and bob and cup geometries. At low shear rates, <100 1/s, the suspensions appeared to remain cohesive between the cup wall and spindle. However, at increasing shear rates, >100 1/s, cohesion between the surfaces became uncertain and the suspension appeared to separate with longer run times. This brought the absolute values of instantaneous viscosity into question, but the relative values between the varying suspensions was still useful for comparative purposes.

Given the difficulties encountered with conventional rheometry, a simpler test was performed to gauge the 'flowability' of each suspension. A setup was constructed mimicking the infiltration method used for forming the composites. An aluminum foam piece, 5 PPI, with bulk dimensions, 40 x 40 x 20 mm, was placed within a cube mold. The exact amount of suspension needed to fully infiltrate the aluminum porosity was then placed on top of the aluminum and vibration via the vibration table was applied to the assembly. The time required for the suspension to fill the aluminum foam was recorded. The end condition was taken as the point in which the suspension and upper surface of the aluminum became flush.

Density was calculated simple by dividing sample mass by volume. Mass of samples was measured via scales. Volume was calculated from caliper measurements of sample dimensions. The procedure for calculating the green density of $CaSiO_3$ within the pores of the Al foam was as follows: First, the mass of $CaSiO_3$ in the composite was determined by subtracting the mass of the foam from the mass of the composite. Then

the volume of the foam was calculated by multiplying the foam mass by the theoretical density of Al, 2.7 g/cm^3. Next, the $CaSiO_3$ volume was found by subtracting the foam volume from the caliper measured bulk volume. Finally, the $CaSiO_3$ mass was divided by the $CaSiO_3$ volume to yield the green density within the Al pores.

After carbonation, the extent of reaction was monitored via mass change, X-ray diffraction (XRD), and Thermal gravimetric analysis (TGA). Mass gain of each sample set, Pure, 5PPI, 10PPI, and 20PPI, was recorded after carbonation. This quantity was solely attributed to the uptake of CO_2 during carbonation reaction, as shown in Eqn. 2.2

$$CaSiO_3(s) + CO_2(g) \rightarrow CaCO_3(s) + SiO_2(s) \quad \text{(Eqn. 2.2)}$$

Thus the percent of $CaSiO_3$ carbonated was determined by Eqn. 2.3.

$$Rxn.Completion = \left(1 - \frac{\frac{m_i}{M_{CaSiO_3}} - \frac{\Delta m}{M_{CO_2}}}{\frac{m_i}{M_{CaSiO_3}}}\right) \times 100 \quad \text{(Eqn. 2.3)}$$

$m_i = initial\ CaSiO_3$

$\Delta m = mass\ gain$

$M_{CaSiO_3} = molecualr\ mass\ of\ CaSiO_3$

$M_{CO_2} = molecular\ mass\ of\ CO_2$

XRD was performed using a Bruker D8 Discover (Bruker AXS Inc., Karlsruhe, Germany) with CuKα radiation (λ = 1.514 Å), parallel beam in the range 10-80˚ (2θ) with a 0.018˚

step size and 1s dwell time. TGA was performed on TA Q500 (TA Instruments, New Castle, DE) from 0-800˚C at a rate of 5˚C/min under 20 ml/min flowing nitrogen.

2.3 Results

Suspension and infiltration

Initial trials showed the maximum achievable solid content of an unaltered $CaSiO_3$ and water suspension to be about 58 vol%. Batches with solids loading greater than 58 vol% failed to become a cohesive suspension after extended periods, > 168 h, of jar rolling. Qualitatively, the suspensions poured quickly with acceptable fluidity between 26-34 vol%. From 34-44 vol%, pour speed decreased, and a thickening was noticeable. From 44-51 vol%, the suspension poured very slowly, and appeared as a slowly deforming, semi-plastic solid. At 58 vol%, the suspension would not pour without vibration, and when vibration ceased, it appeared to hold it shape.

Samples cast from additive-free suspensions ranging between 26-58 vol% displayed an increase in green density of 1.58-1.79 g/cm^3 as the solids content increased (Fig. 2.2). At 26 vol% solids content, the mold was filled in under 10 sec. Processing times greater than 5 min were required 58 vol% solids content suspensions to fully fill the mold. Thus, the trend was believed to not continue past the 58 vol% point. A higher green density was deemed favorable, as these suspensions produced samples with the highest compressive strength, both for the green samples and post g-rHLPD samples. Therefore, the need for improving the high solids content suspensions flow

behavior was necessary. Also, infiltrating a 58 vol% suspension into Al foam and achieving a green density of at least 1.79 g/cm^3 was set as a target.

An increase of the surface charge of the powder was attempted for enhancing suspension flow. Adjustment of suspension pH into the basic region was performed via addition of KOH. Adjustment of the water pH in the acidic region was avoided due to the expected dissolution of the $CaSiO_3$. The natural pH (pH of unadjusted DI-water and $CaSiO_3$) of the suspension was about 9-10 pH, and use of pH 8-10 adjusted water during batching had little effect. (Fig. 2.3) Increasing the batched water's pH > 11 lead to a stable increase in the suspension pH, as repeated measurements over many days did not show significant change. Viscosity was measured for each of the increasing pH suspensions. (Fig. 2.4) It decreased with each subsequent incremental increase in pH, with the most pronounced change, 0.23-0.03 Pa·s, occurring from pH 10-12 respectively. After 12, the change between each pH step was relatively small, 0.03-0.015 Pa·s. These results corresponded with qualitative evaluations. The data was fitted with an exponential, $y=3.79*10^5 *\exp(-x/0.69)-2.89*10^{-2}+2.59*10^{-3}$ x with an R-square value of 0.9998.

Zeta potential calculations were recorded for the same pH steps. (Fig. 2.5) Initially, a -33 mV zeta potential was recorded at the suspension's natural pH. A minima of -45 mV appeared in the pH 11-12 region, identifying the greatest zeta potential magnitude. This might be one factor in the unaltered suspension's ability to flow at high solids contents, as high magnitudes of the zeta potential are associated suspension stability.[70] As pH was increased further the magnitude decreased back to -30 mV. A

sodium polyacrylate dispersant was then added to further enhance the apparent surface charge of the $CaSiO_3$ particles. In the pH 10-11 range, the magnitude followed that of the unadjusted suspension, about -30 to -45 mV respectively. The dispersant added sample then had a significant increase in magnitude to about -60 mV at pH 12.5. Further increasing pH past 12.5 appeared to reduce the zeta potential magnitude. These findings indicated that the best conditions for high surface charge, and thus suspension stability from repulsion, lie in the greater than pH 12 range with added dispersant.

The time required for infiltration into Al foam for three $CaSiO_3$ suspensions, $CaSiO_3$ in water, $CaSiO_3$ in pH adjusted water, and $CaSiO_3$ in pH adjusted and Darvan 811 added water, were 452, 372, and 128 s respectively. As expected, time required for the suspension to fully infiltrate the Al scaffold decreased with each change. (Fig. 2.6) This result demonstrated that the previously set target of improved ease of processing was achieved.

The green density of the $CaSiO_3$ portion of each sample set was recorded to ensure that infiltration across the pore sizes was comparable. (Fig. 2.7) All composites reached similar ceramic green densities, 1.88, 1.79, 1.81, and 1.88 g/cm^3 for Pure, 5PPI, 10PPI, and 20PPI samples respectively. These results showed that the engineered suspension allowed for comparable and better green densities to be achieved even after infiltration into small pore scaffolds. Thus, the optimal suspension composition was determined to be 58vol% $CaSiO_3$ with 42vol% pH12 water with about 0.5% Darvan 811.

Carbonation

The phase composition of the ceramic before and after carbonation was determined using x-ray diffraction (Fig. 2.8). Before carbonation only $CaSiO_3$, PDF#97-020-1537, was observed. $CaCO_3$, PDF#97-015-8257, was observed in the pattern after reaction, most notably from the appearance of the $CaCO_3$ primary peak at 29.3˚ 2θ. This result suggested that the mass gain was indeed due to carbonation. SiO_2 was not identified in the post-reaction pattern, indicating a non-crystalline structure for that compound. As a double check, TGA was also performed on powder before and after reaction (Fig. 2.9). The $CaSiO_3$ powder lost less than 1 wt% throughout the temperature range. The majority of the 1 wt% loss appeared to correspond with the carbonate decomposition region of 550-700˚C, indicating that the as received mineral composition contained a small amount of $CaCO_3$. The carbonated powder lost about 22 wt% throughout the temperature range. The initial 2 wt% mass loss in the <300˚C region was attributed to water. The remaining 20wt% loss occurred predominantly in the 550-700˚C range, indicating that a significant portion of the sample's composition was $CaCO_3$. Mass gain from carbonation of cast samples was used to calculate reaction completion as well, 46, 47, 52, and 37% for Pure, 5PPI, 10PPI, and 20PPI respectively (Fig. 2.10). The smallest pore size, 20 PPI did not carbonate as well as the other three types. This was believed to be partially due to the smaller channels within the Al foam, but also due to likely deviations in the carbonation reactor such as heat and gas gradients, or pore saturation from water vapor condensation. It was expected that with repeated trials and a greater sample set that all sample types would have similar extent

of reactions. The bulk density for the 5, 10, and 20PPI composites varied little at 2.18, 2.21, 2.20 g/cm^3 respectively.

2.4 Discussion

Initial observation of the un-altered suspension show a surprisingly high solids content of about 58 vol%.(Fig. 2.2) Paired with the pH profile shown in figure 2.3, some inferences may be drawn about why. The pH of the suspension does not deviate below pH 10. This may be indicative of unequal dissolution of Ca-O and Si-O at the $CaSiO_3$ surface, which has been found to be very prevalent at low pH (<5).[71–73] At higher pH, the mechanism is less clear, with some evidence for more equal dissolution of Ca-O and Si-O.[73] Re-precipitation of Si-O at the particles surface has also been suggested, which would result in a net loss of Ca at the particle surface even if the initial dissolution was equal.[74] The resulting surface would have to balance its charge with proton absorption, leading to increased pH. This fits with the pH of the suspension remaining above 10 when the solution pH used was between 7-10. Beyond pH 10, the increase was most likely dominated by KOH. The high initial solids loading may then be made possible by the Ca depleted $CaSiO_3$ surface having an effective charge. Repulsion between particles would lead to a more stable suspension with improved flow. Zeta potential calculations support this concept, with about -33 mV found at pH 10 and literature values also put report zeta potential of wollastonite in the -30 – 40 mV range at pH 10.[75]

Addition of sodium polyacrylate dispersant was shown to significantly increase the calculated zeta potential of $CaSiO_3$ particles.(Fig. 2.5) The flow of high solids $CaSiO_3$

suspensions were also found to improve dramatically when the dispersant was incorporated.(Fig. 2.6) These findings follow mineral wollastonite supplier suggestions that sodium polyacrylate will improve flow behavior of high solids content slips.[76] Given the likelihood of a more silica dominant surface characteristic of the particles due to the previously discussed unequal dissolution, it would appear that the anionic polymer must absorb onto a silica site. However, literature suggests that little adsorption of sodium polyacrylate will occur on silica surfaces due to like charge repulsion.[77, 78] Rather, it was found that the dispersant preferentially adsorbs on calcium ions and that increased calcium concentration might hinder any weak adsorption on silica.[79] This suggests that the surface interaction between the $CaSiO_3$ particles and sodium polyacrylate is more likely due to the presence of calcium at the surface, and perhaps mediated by calcium ions in solution. Further, the improved surface charge was found to be at pH 12-12.5. At this pH range it was noted in the literature that the dissolution of Ca-O was diminished compared to lower pH. At pH 11, it was noted that Ca loss was only 2-3 atoms/nm^2 greater than Si loss.[75] Thus, while the surface of the $CaSiO_3$ particles may indeed have a higher Si-O concentration, there is likely still enough calcium present to provide adsorption sites for the dispersant.

The pH adjusted, sodium polyacrylate added suspension infiltrated all of the Al foam types with no substantial difference in resulting green density compared to $CaSiO_3$ only samples.(Fig. 2.7) This result showed that the interaction between the Al surface and the infiltrating suspension was not inhibiting, as the smaller PPI Al foam effectively have greater surface for the suspension to contact. Carbonation was also successful for

all samples, confirmed through mass gain, XRD and TGA.(Figs. 2.8-10) Thus, the resulting IPCs across all Al foam types were considered ready for mechanical testing.

2.5 Conclusion

High solids (58 vol%) $CaSiO_3$ suspensions with flow properties suitable for pressureless infiltration were formed. Subsequent infiltration into Al foam yielded comparable green density (~1.8 g/cm^3) and carbonation (~45%) to ceramic only samples. This total process was conducted at temperatures ≤ 90˚C, no applied pressure, and ≤ 20 psig CO_2 reactor pressure. Thus, the high temperatures, high pressures, wetting agents, and stringent atmospheric control normally associated with infiltration formed metal-ceramic IPCs were avoided and the process fit the paradigm for more sustainable IPC fabrication.

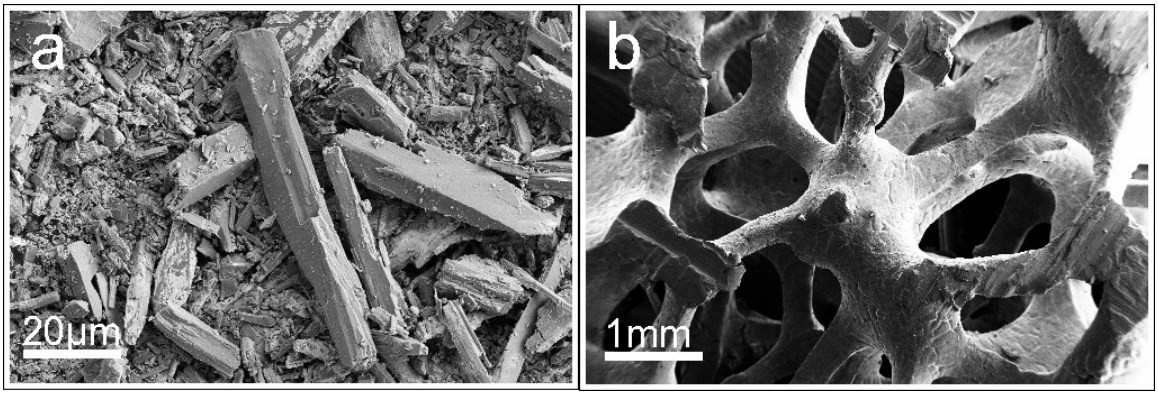

Figure 2.1. As-received materials. a) Acicular wollastonite mineral particles. b) Aluminum foam struts showing surface pitting and roughness.

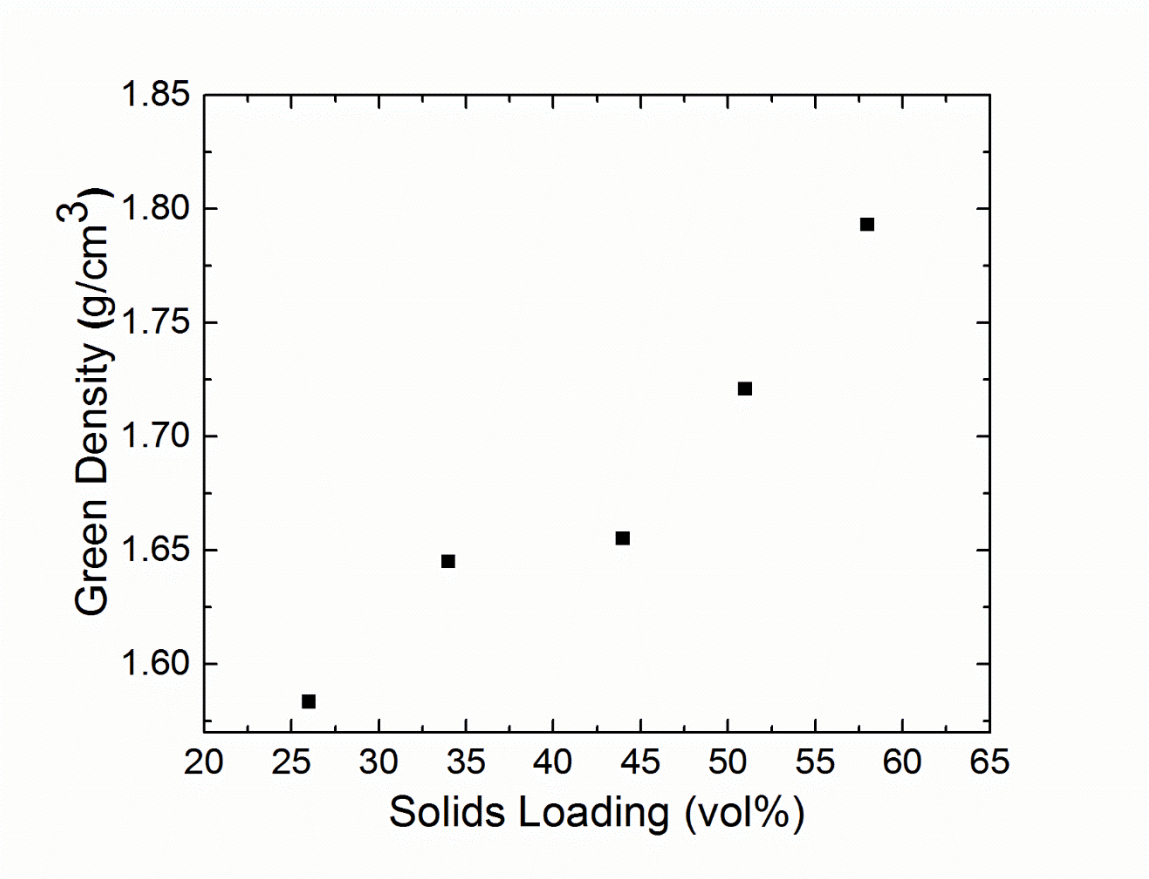

Figure 2.2. Green density as a function of solids loading. Suspensions could not be formed above 58vol% solids.

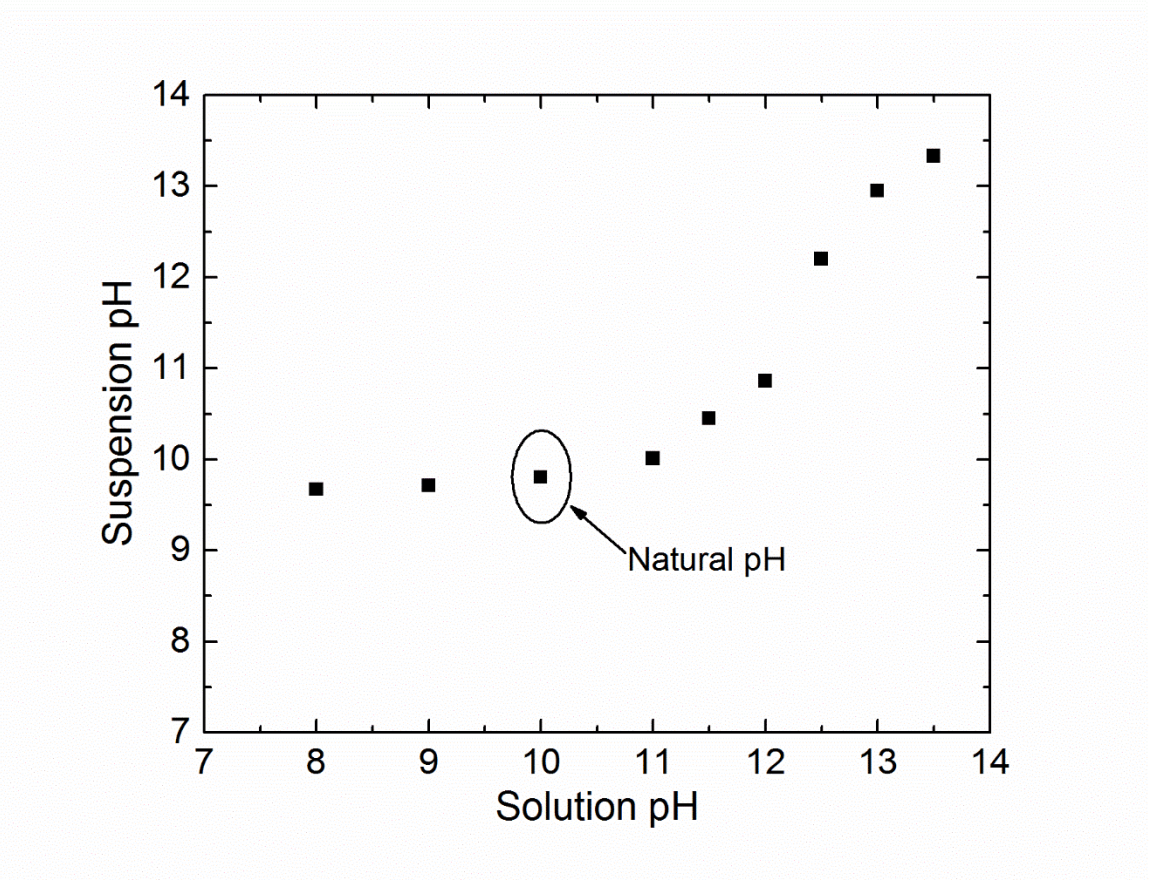

Figure 2.3. Suspension pH as a function of the starting solution pH.

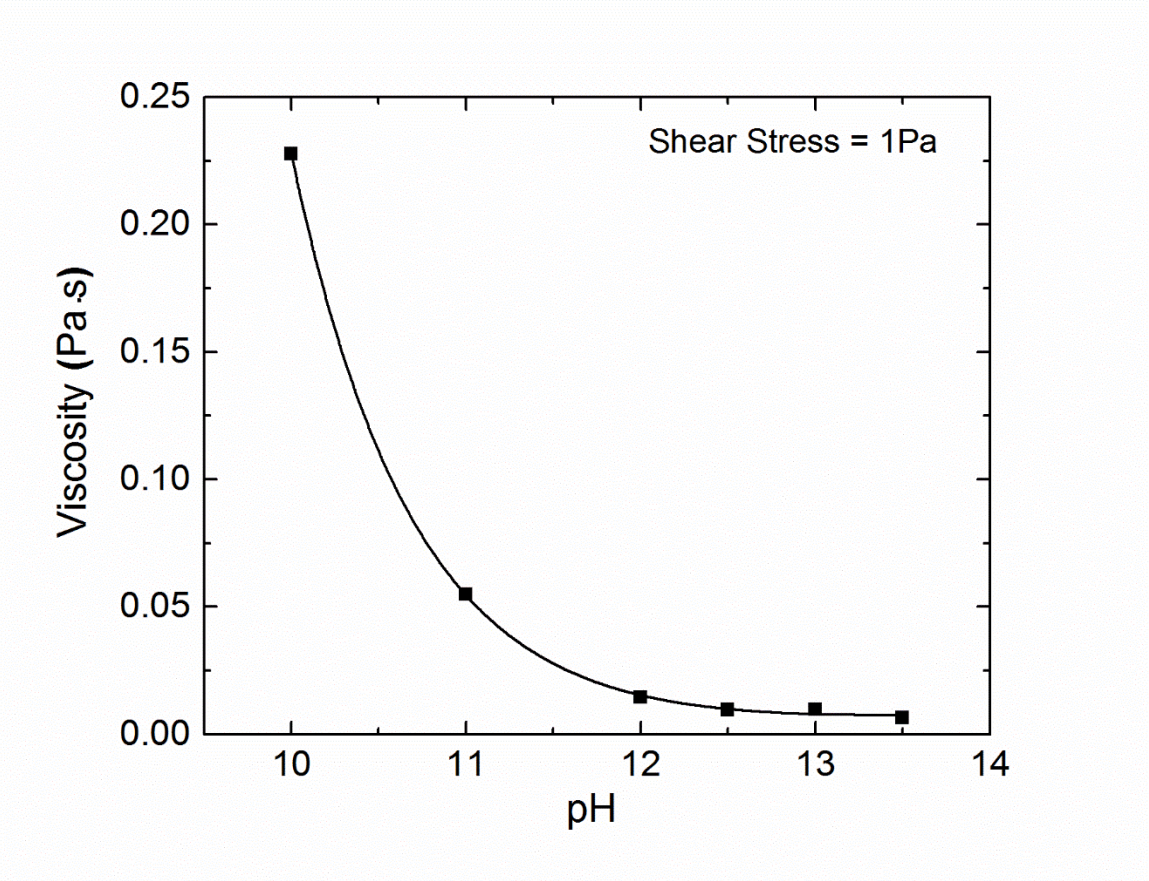

Figure 2.4. Viscosity as a function of pH for applied shear stress of 1 Pa.

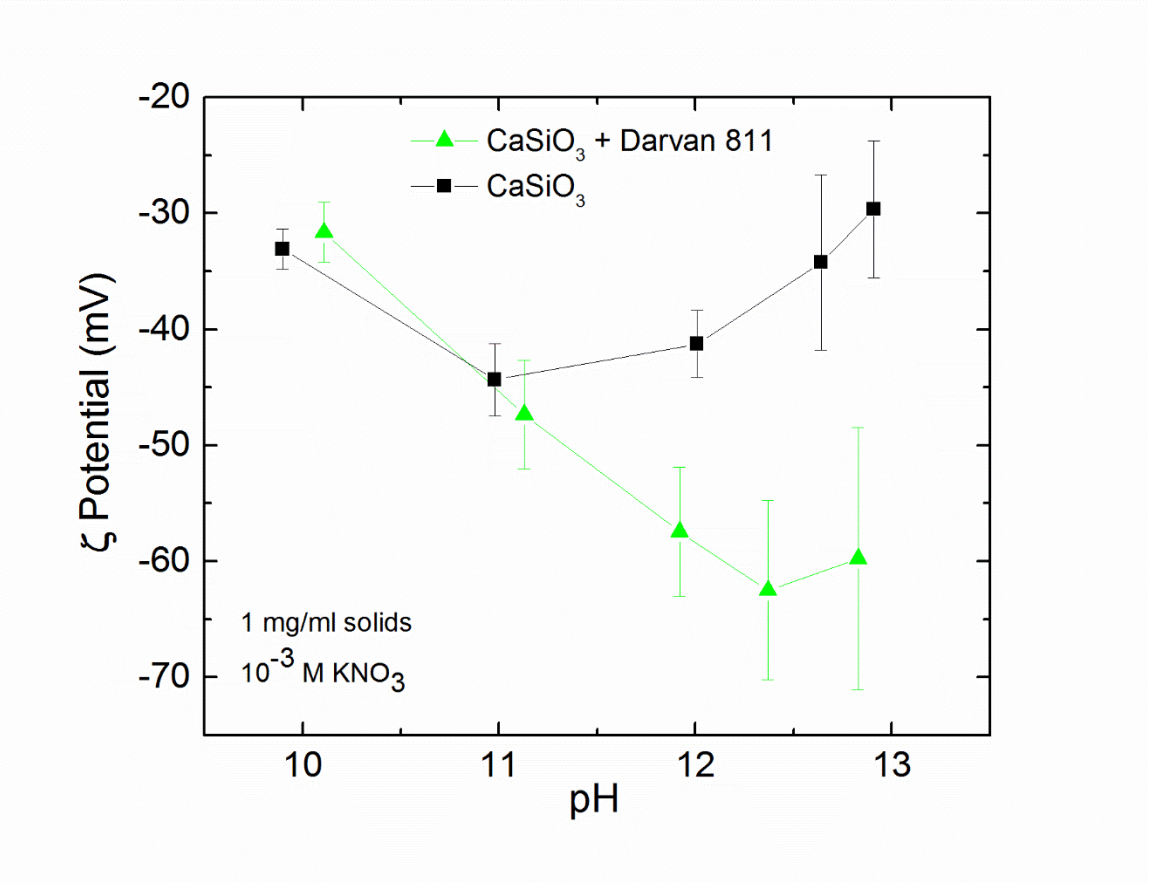

Figure 2.5. Zeta potential as a function of pH for $CaSiO_3$ suspensions with and without Darvan 811 dispersant. Dilute suspensions at 1 mg/ml solids with 10^{-3}M KNO_3 indifferent electrolyte added were used.

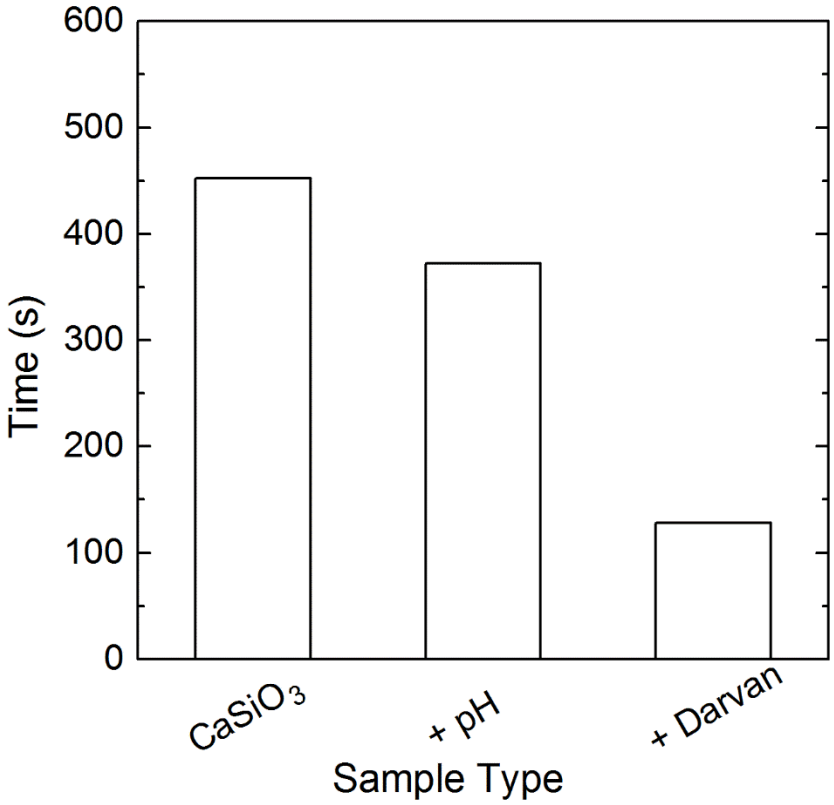

Figure 2.6. Infiltration times of 58 vol% CaSiO3 suspensions. 10-2 M KOH was added to adjust pH and 1wt% Darvan 811 was added for dispersion.

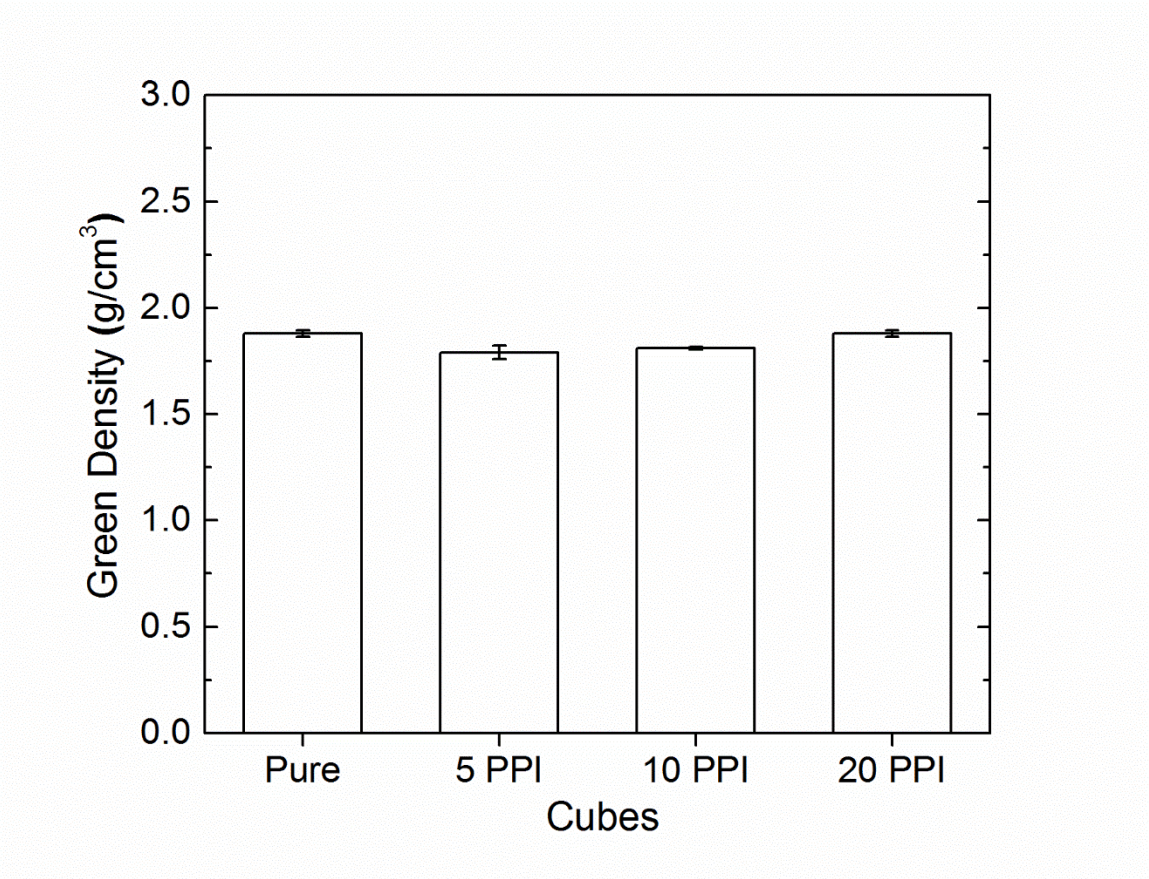

Figure 2.7. Ceramic green density of Pure, 5 PPI, 10 PPI, and 20 PPI samples, formed via casting of pH adjusted and Darvan 811 added 58 vol% $CaSiO_3$ suspension.

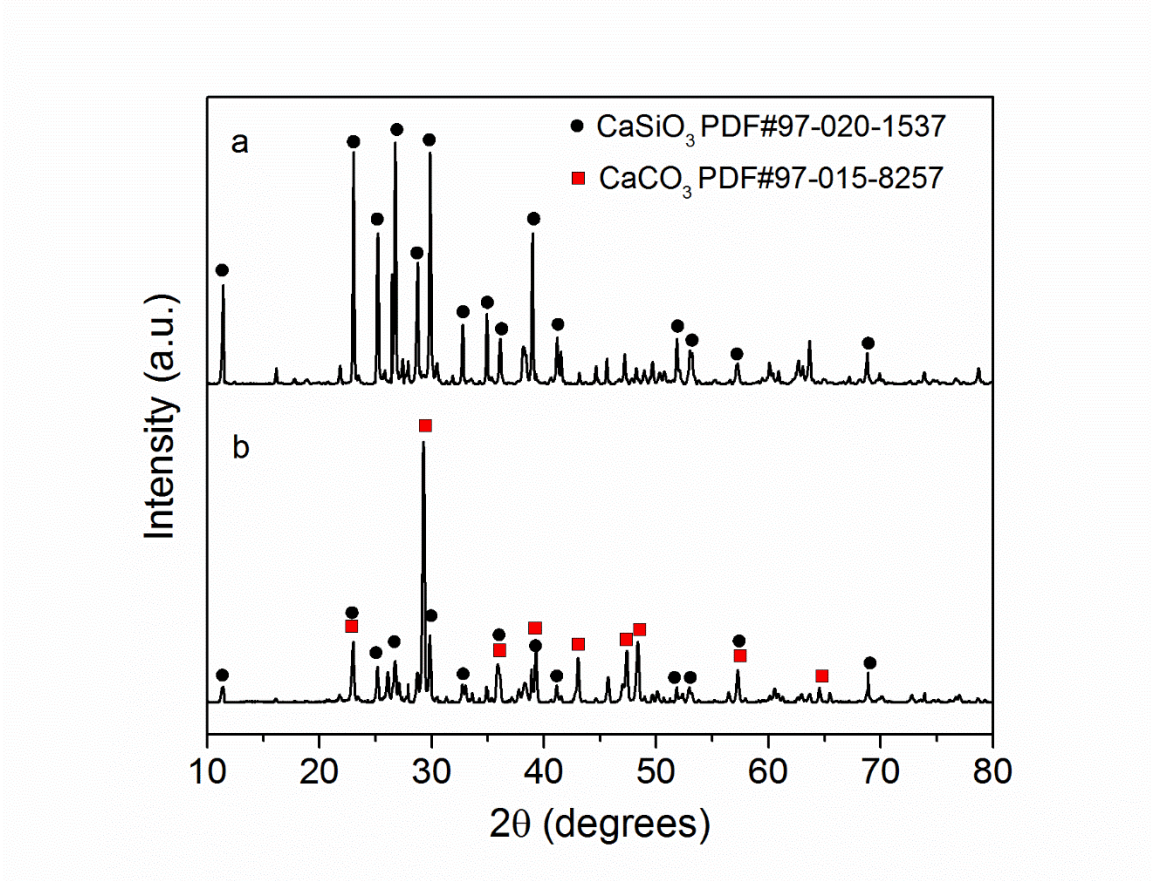

Figure 2.8. XRD patterns showing phase composition a) before and b) after carbonation.

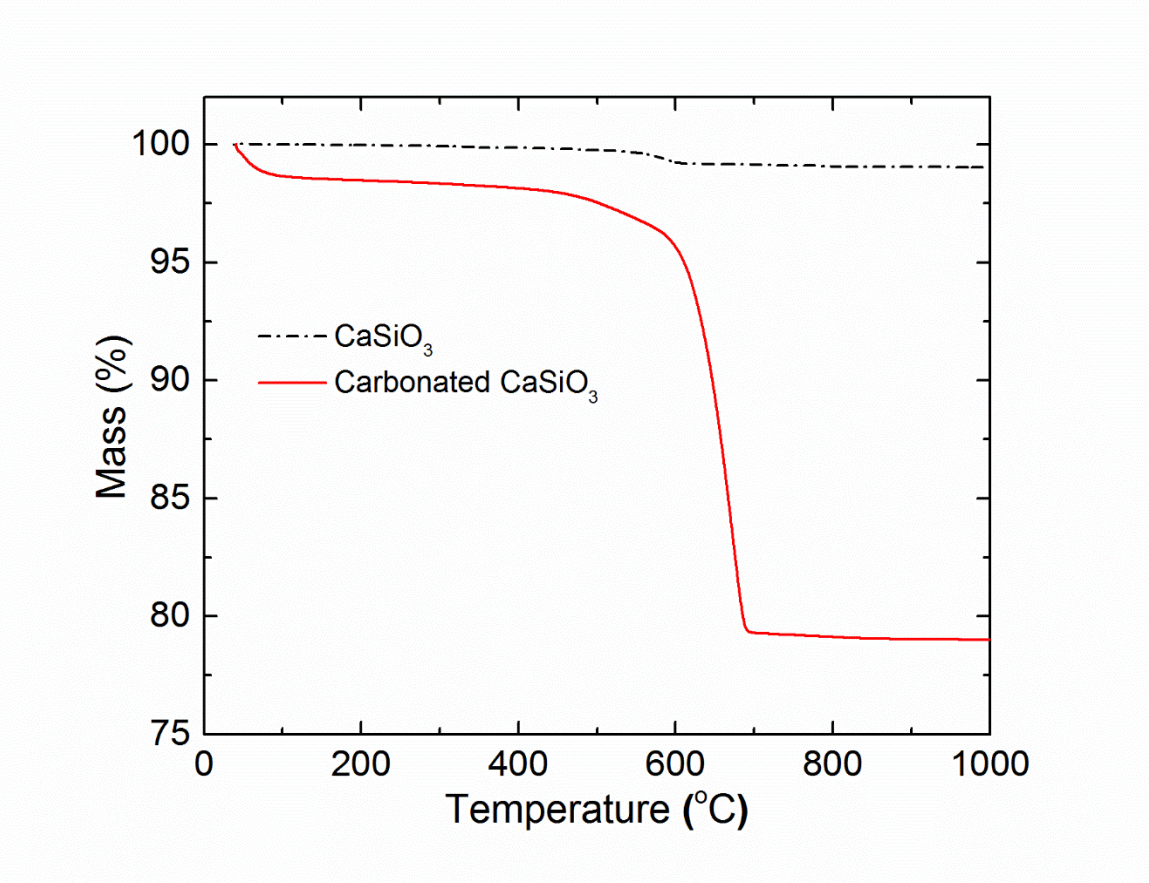

Figure 2.9. TGA comparison of $CaSiO_3$ and carbonated $CaSiO_3$ showing mass loss as a function of temperature.

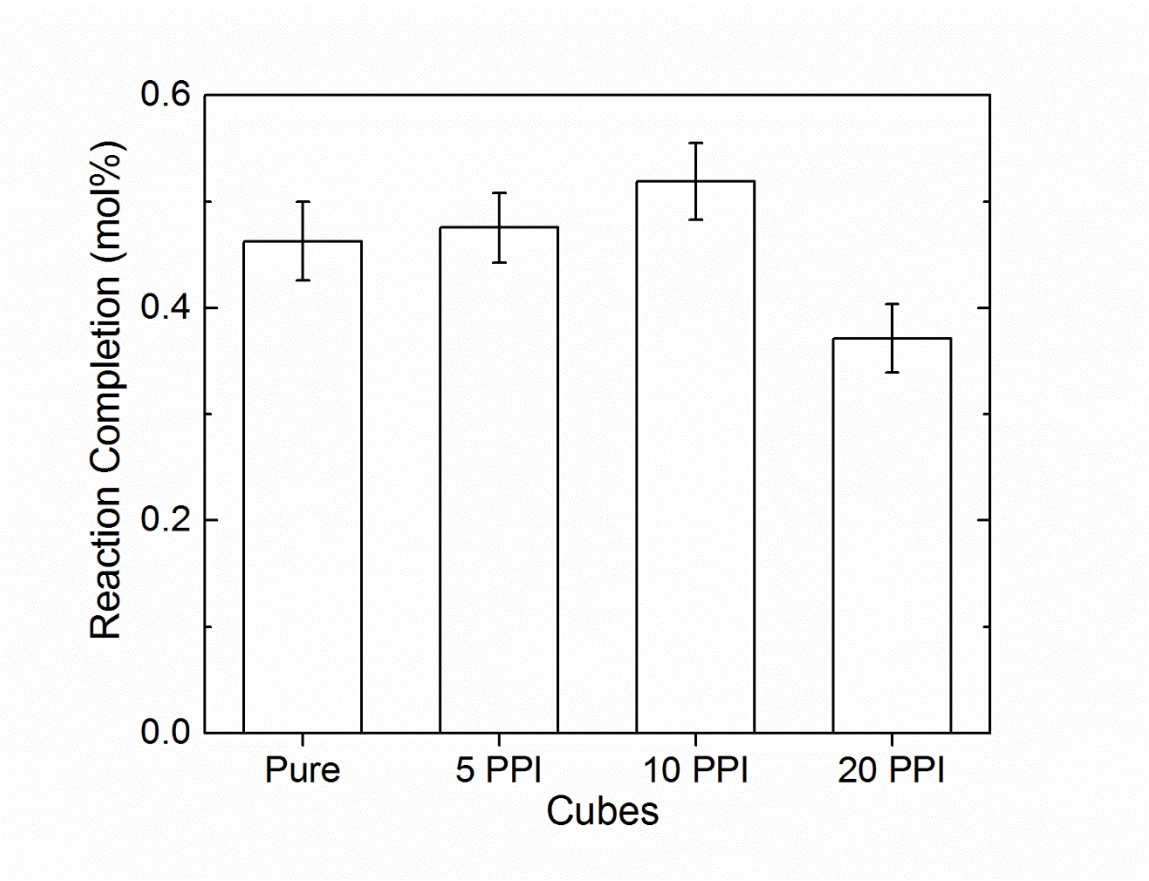

Figure 2.10. Reaction completion for each sample type.

3. Al-Carbonated $CaSiO_3$ IPC Mechanical Properties and Structure-Property Relationships

3.1 Introduction

Recent progress in composite fabrication has enabled more and more complex combinations of materials. The ability to produce materials in which multiple components are intertwined and continuous along all dimensions has led to interesting multifunctional properties which are not attainable in single materials. Such IPCs can potentially have each of its components contribute their unique property to the macroscopic properties of the composite. Thus IPCs have shown better strength, toughness and wear resistance compared to other composite structures. [44, 67, 68]

IPCs in which the metal phase is Al and formed via an infiltration process are relevant examples to consider. Metal-ceramic IPCs are frequently produced via Al melt infiltration into a ceramic scaffold. Metal-polymer IPCs are produced by the melt infiltration of a polymer to a metal scaffold, as polymers melt at temperatures far lower than metals. Composite density and strength for aluminum-ceramic/polymer IPCs from the literature are shown in Fig. 3.1.[30, 80–85] Aluminum-polymer IPCs have lower density with accompanying lower compressive strength compared to the higher density and strength aluminum-ceramic IPCs. For example, polymethyl methacrylate (PMMA)/Al IPC has a density of 1.65 g/cm^3 and compressive strength of 67 MPa whereas the Ti_2AlC/Al IPC has density of 3.55 g/cm^3 and compressive strength of 560 MPa. This comparison

shows a gap in material properties, where a middling density (1.5-3 g/cm^3) and middling compressive strength material (75-550 MPa) could fit, such as an aluminum-ceramic IPC with lower density than that of those in Figure 3.1, but with higher strength than the polymer-metal IPCs. New approaches to IPCs formed via infiltration can help fill this property space.

As reported in Chapter 2, infiltration and subsequent carbonation via g-rHLPD of a $CaSiO_3$ suspension within the pores of Al foam is possible. The carbonated $CaSiO_3$ exhibits bulk density of about 2.2 g/cm^3 and has been shown to have strength in the 100-200 MPa range. [56–58, 69] These properties place the carbonated $CaSiO_3$ in the open property space of infiltrated Al IPCs. Thus, combining carbonate $CaSiO_3$ with Al foam should produce a strong, yet tough material. Beyond the direct ductility contribution of the Al foam, crack bridging and blunting is likely, as well as lateral confinement of the brittle ceramic.[30, 47, 86–89] Both these concepts may allow the effective compressive strength of the IPC to exceed that of stand-alone carbonated $CaSiO_3$ and provide stress resistance at increased strains. Such properties would suggest that the Al-carbonated $CaSiO_3$ IPC may be suitable for use in damage prone structures.

The objective of this chapter is to determine the mechanical properties of the Al-carbonated $CaSiO_3$ IPCs. Following destructive testing, investigation of the metal-ceramic interface will be carried out. This will shed light on the nature of the interaction between the metal and ceramic, and subsequently provide insight into the stress resistance and failure mechanism of the IPC.

3.2 Experimental

Experimental Strategy

Al-carbonated $CaSiO_3$ IPCs will be made by infiltrating $CaSiO_3$ suspensions into 3 different pore size Al foams according to the process detailed in Chapter 2. Large samples will be formed in order to provide better comparison to conventional FOB materials. Cubes will be made for compression testing and tiles for flexural testing. Mechanical response will be recorded for each test type and analyzed. The interface between the Al and carbonated $CaSiO_3$ will then be observed prior to and after failure. Chemical mapping and elemental state at the interface will also be studied.

Materials

Mineral wollastonite, NYAD® 400 (NYCO Minerals Inc., Willsboro, NY) was used as the $CaSiO_3$ source. Bone-dry carbon dioxide, CO_2 (CAS# 124-38-9, Airgas, Waterford, CT) was used for the g-rHLPD carbonation step. Water was filtered through a Progard® 2 and Q-guard® 1 purification system (EMD Millipore, Billerica, MA) prior to use. Potassium hydroxide, KOH (CAS# 1310-58-3, Fischer Scientific, Pittsburgh, PA) was used for pH adjustment. A 3500 molucular weight sodium polyacrylate solution, Darvan® 811(R.T. Vanderbilt Co, Inc., Norwalk, CT) was used for stabilizing the dispersion of wollastonite suspensions. 4L polypropylene wide mouth jars(# 4322T6, McMaster-Carr, Robbinsville, NJ) contained the suspensions. Aluminum foam (Duocel® Alloy 6101-T6, ERG Materials and Aerospace Corp., Emeryville, CA) of 5 PPI (pores per inch), 10 PPI and

20 PPI and relative density 10-12% served as the aluminum scaffold for infiltration. Figure 2.1 shows SEM images of the as-received $CaSiO_3$ and Al foam.

Processing

Samples were produced via the procedure detailed in chapter 2. Custom steel molds were procured to fit the Al foam and allow for drying of the infiltrated $CaSiO_3$ suspension. Compressive testing sample dimensions were approximately 40x40x40 mm cubes. Bend test samples were also prepared as 12x50x200 mm tiles. These relatively large sample size were used to provide better comparison to FOB structures. Care was taken during processing to produce near parallel sample surfaces, and when needed post-machining was performed with a precision cutter (PICO 155 precision cutter, PACE Technologies, Tucson, AZ).

Samples were prepared for imaging and chemical analysis via polishing. Representative pieces of samples were first cut to small size using the precision cutter. After drying, the samples were placed in 1" diameter cylindrical molds and infiltrated with mounting epoxy (EpoThin 2 Epoxy System, Buehler, Lake Bluff, IL). Vacuum was then pulled on the freshly poured epoxy/sample containing molds using a Cast N' Vac 1000 Vacuum Impregnation System (Buehler, Lake Bluff, IL) for ~5 min, then left in ambient conditions for 24 h to harden. The hardened epoxy mounted samples were then ground and polished on an EcoMet 250 Grinder-Polisher (Buehler, Lake Bluff, IL). The typical polishing schedule used was as follows: 1) 320 grit SiC paper, 30 1/s head speed, 240 1/s base speed, complementary head/base direction, 5 min. 2) 6 µm

polycrystalline diamond suspension (DIAMAT, Pace Technologies, Tucson, AZ) on Tri-Dent cloth (Buehler, Lake Bluff, IL), 30 1/s head speed, 150 1/s base speed, complementary head/base direction, 6 min. 3) 3 µm polycrystalline diamond suspension (DIAMAT, Pace Technologies, Tucson, AZ) on Tri-Dent cloth, 30 1/s head speed, 150 1/s base speed, complementary head/base direction, 4 min. 4) 0.05 µm polycrystalline diamond suspension (DIAMAT, Pace Technologies, Tucson, AZ) on Micro-Cloth (Buehler, Lake Bluff, IL), 30 1/s head speed, 150 1/s base speed, contra head/base direction, 2 min. After polishing, the epoxy was cut away from the samples.

Interface Chemistry Simulation

OLI Systems stream analyzer software (*Treatment Simulation*

OLI Systems stream analyzer software (ver.9.0, OLI Systems, Inc., Cedar Knolls, NJ) was used to model each treatment reaction. The software used thermodynamic parameters obtained by analysis and regression of reported primary experimental results. Publications regarding thermodynamic modeling provide examples for this procedure.[90–94] Chemical surveys were generated to observe the relative change in solid species concentration as a function of CO_2 concentration. Precursor inputs for this simulation were as follows: 55.5 mol/L H2O, 1 mol/L $CaSiO_3$, 1 mol/L Al, and 0.1 – 1 mol/L CO_2 varied in 0.1 mol steps. Pressure was set to 2 atm (30psi) and temperature was held at 90˚C. After identifying all equilibrium solid products, yield diagrams were generated to highlight feasible ranges of formation. The same precursor concentrations

were input as above. Pressure was set to 2 atm, and the temperature was varied from 25-100˚C in 10˚C steps.

Mechanical Testing

Reacted cube samples were tested in compression. A 200 kN load cell equipped test frame (Instron, Norwood, MA) was used at a strain rate of 2 mm/min. End conditions were set to a displacement of 50% of total height or surpassing of the load cell capacity (F > 200 kN). High strain end conditions were chosen to allow observation of residual stress resistance of the composite after initial failure. Due to slight differences in sample pre-loading, all strain values were normalized to ensure that the stress vs. strain plots were comparable. The elastic modulus for each sample was determined by selecting a linear portion of its the stress vs strain plot, applying a linear fit, and taking the resulting slope as the elastic modulus. In all cases the adjusted R-square of the fit was greater than 0.995.

Reacted tile samples were tested in 3-point bending. A 20 kN load cell equipped test frame (Instron, Norwood MA) was used at a rate of 0.5 mm/min. The span between the lower support pins was 150 mm with the pins contacting the sample 25 mm from the edge. End conditions were set to 5 mm displacement and tests were manually stopped if samples separated completely before 5 mm was reached. Stress vs. strain plots were normalized based on specimen pre-loading.

Characterization

Sample microstructure at fracture surfaces and polished sections were observed by field emission scanning electron microscopy (FESEM) using a Zeiss Sigma FESEM(Carl Zeiss, Oberkochen, Germany) at 5kV. Sample surfaces were sputter coated with 10 nm thick gold coatings (Electron Microscopy Sciences, model# EMS 150T ES, PA) using a sputtering current of 20 mA for 5 min. Energy dispersive spectroscopy (EDS) was also used to ascertain chemical composition of the observed surfaces. Accelerating voltage was increased to 10kV to increase the collected counts/sec and the aperture was widened until ~1000 counts/sec was attained. Typically, data was collected for ~10 min prior to compiling elemental maps.

X-ray photoelectron spectroscopy (XPS) was performed using a K-Alpha™ Photoelectron Spectrometer (Thermo Scientific, Inc., Pittsburgh, PA) to examine the surface and interfacial chemistry. A monochromated Al K-α source was used with a 30 μm spot size and 0.25 eV binding energy resolution. Spectra were collected from ceramic, aluminum, and ceramic-aluminum interface regions. Peak analysis and fitting were performed using Avantage Data System Software (Thermo Scientific, Inc., Pittsburgh, PA). Doublets were applied to the 2p peaks for each element, and peak width and the Gaussian/Lorentzian ratio were manipulated to reduce the residual error between the resulting fit envelope and the corresponding raw data. For presentation and comparison, each spectra was normalized to the adventitious carbon 1s peak. Subsequently, Ca 2p peaks, Si 2p peaks, and Al 2p peaks were overlaid in order to assess any prevalent peak shift from one sample location to the next. A shifted peak would

indicate a change in the chemical bonding environment for the element in question, and thus suggest the presence of a different interfacial compound.

3.3 Results

Mechanical Properties

Compressive strength tests on Pure samples showed brittle behavior with a steep decline in stress after ultimate strength was reached. (Fig. 3.2) The average ultimate strength of Pure samples was 68 MPa with a 14 MPa standard deviation. Prior to ultimate strength and failure, some samples displayed steep drops in stress followed by a regaining in strength. Compression tests on aluminum foam samples showed ductile behavior with no apparent failure point. (Fig. 3.3) There were three distinct regions of the stress vs. strain curve for the foams, 1) initial elastic region with a steep increase in stress to 1.5-3 MPa, 2) plastic deformation attributed to cell collapse appearing as near constant stress between 5-35% strain, and 3) densification of the structure after cell collapse completes appearing as increasing stress at >35% strain. Composite compression ultimate strength for the three different foam pore sizes exceeded that of the Pure samples. (Fig.3.4) Average ultimate strengths for the 5PPI, 10PPI, and 20PPI samples were 108, 123, and 116 MPa with standard deviations of 10.4, 0.5, and 3.8 MPa respectively. In some cases, the samples resisted enough stress to exceed the capacity of the load cell, and thus did not fail. In particular, the 10 PPI samples all exceeded the load cell capacity. In the instances where samples did fail, an extended region of stress resistance after failure was observed out to about 35% strain.

The average elastic moduli of the components and composite was reported in Fig. 3.5. 5PPI, 10PPI, 20 PPI aluminum foam had average elastic moduli of 1.08, 1.02, and 1.37 GPa and standard deviations of 0.07, 0.19, and 0.05 GPa respectively. $CaSiO_3$ samples had an average elastic modulus of 26 GPa with a standard deviation of 3.95 GPa. 5PPI, 10PPI, and 20PPI infiltrated composites had 28, 36, and 31 GPa average elastic moduli and 2.08, 1.35, and 1.01 GPa standard deviations respectively.

Three point bending on Pure samples showed that the carbonated $CaSiO_3$ does not possess ductility, as all samples failed completely immediately after ultimate flexural strength was reached. (Fig. 3.6) The average flexural strength for the Pure samples was 20 MPa with a standard deviation of 4.3 MPa and failure occurring at approximately 0.3 mm deflection. Al Foams in three point bending displayed no failure over the 5 mm displacement tested. Rather, the amount of flexural stress resisted appeared to plateau and the average for the apparent horizontal limit was 2.8 MPa. (Fig. 3.7) Al-carbonated $CaSiO_3$ composite tiles failed at about the same displacement as the ceramic tiles, but did not cease to resist load immediately afterwards. (Fig. 3.8) The average maximum flexural strength across all three composite sample types was about 17.8 MPa with a standard deviation of 2.7 MPa.

Interface

Simulations were conducted to predict if compounds other than that presented in Eqn. 2.1 and aluminum/alumina may have formed at the $CaSiO_3$ - Al interface. (Fig. 3.9) Surveying over increasing concentrations of CO_2, $CaCO_3$ and $Al_2Si_2O_5(OH)_4$ were

expected at the high end of CO_2 concentration. The chemical diagram, considering the Al subsystem, indicated that possible solid species may precipitate when concentrations of interacting Al and $CaSiO_3$ are available. At the lower concentrations (mol/L<10^{-6}) of $CaSiO_3$ and Al, no solid precipitate was predicted.

Optical and SEM images of polished cross-sections showed good contact between the aluminum and ceramic material. (Fig. 3.10, a&c) In the optical image, Fig. 3.10 a, a disproportionate amount of fine $CaSiO_3$ particles, ~1 μm diameter, appear near the Al surface compared to the larger, ~10 μm diameter, particles in the bulk ceramic region. At the interface, the two regions are in continuous contact, with some evidence of pullout from polishing. The SEM image of the polished interface, Fig. 3.10 c, more clearly showed that the majority of ceramic contacting the Al appears to be from the reaction products, $CaCO_3$ and SiO_2. The fracture surface optical image, Fig. 3.10 b, showed separation between the ceramic and metal, a crack within the ceramic, and some material adhered to the metal. SEM investigation of this region, Fig. 3.10 d, confirmed that the material was crystalline ceramic. Chemical maps via EDS showed abrupt boundaries between the metal and ceramic phase. No evidence of aluminum in the ceramic region or calcium or silicon in the metal region was observed. (Fig. 3.11)

Comparative XPS spectra at the interface, within only the ceramic region, and within only the aluminum region also did not show evidence of the predicted interface products. (Fig. 3.12) The Al 2p, Si 2p, and Ca 2p peaks did not show appreciable shift between the scanned regions. Peaks in the Al 2p spectra were attributed to aluminum and alumina.[95] The peaks in the Si 2p spectra was attributed to both SiO_2 and $CaSiO_3$

due to very similar binding energies of those two states.[96] Ca 2p peaks also appeared to be a likely combination of $CaCO_3$ and $CaSiO_3$, as their respective binding energies are known to overlap.[97] A comparison of the doublet fitting for the Si 2p spectra was also provided in the bottom right of Fig. 3.12.

3.4 Discussion

Ultimate compressive strength of the composites exceeded that of the $CaSiO_3$ only and the Al foam samples for every aluminum foam size. (Fig. 3.2-4) This was notable from a bulk properties standpoint, as the composite strength would normally be expected to lie between that of the individual components. The likely explanation for this behavior was due to containment of the ceramic by the aluminum during loading, as similarly observed in other IPCs, as well as in confined concrete.[30, 87, 88, 98, 99] Comparing the linear portion of the stress vs strain curves for carbonated $CaSiO_3$ only with that of the composites showed that both systems have similar elastic moduli. (Fig. 3.5) This implied that in the linear elastic region, the carbonated $CaSiO_3$ was bearing most of the load. As the axial dimension decreased due to the applied compressive stress, an increase in the lateral strain must have occurred in accordance with the material's Poisson's ratio, effectively applying tension laterally across the carbonated $CaSiO_3$. In the carbonated $CaSiO_3$ only samples, a critical lateral strain was reached leading to cracking and failure. In the composite samples, this onset of cracking of the ceramic was delayed due to the inhibition of lateral strain by the surrounding Al. Thus, higher ultimate strengths were observed in the composite samples.

Additionally, this confinement lead to gradual failure of the composite samples with residual stress resistance at increased strain. The extended stress resistance indicated that the composite can dissipate an appreciable amount of energy as the material fails. The behavior is somewhat different than that of the Al foam, where 3 distinct regions exist. Rather, the composite's stress vs strain behavior showed 4 distinct regions. First, an elastic region, same as the foam. Second, an ultimate strength followed by quickly diminishing stress, not seen in the foam behavior due to the absence of a brittle phase. Third, a continued stress resistance for extended strain, as the outer portions of the composite fail and spall off. This region for the Al foam was represented by collapsing of the foam cells. Finally, complete destruction of the composite, whereas the foam plastically densifies. [30]

Both properties, compressive strength and stress resistance after initial failure (energy absorption) place these composites in unique spot amongst the IPC literature. The strength is considerably lower than that of advanced sintered ceramic systems, but better than most polymer infiltrated IPCs. The composite density, ~2.2 g/cm^3, also falls between that of polymer and sintered ceramic IPCs. Additionally, the stress resistance after failure is better than that of most advanced sintered ceramics, but fails at high strains where some polymer infiltrated IPCs survive. This combination suggests the material would be well suited for structural applications where a minimum strength is needed, but where damaging events frequently lead to conventional material failure. For example, a conventional concrete partition used on highways might only be capable of withstanding a single collision before requiring replacement. The presented

carbonated $CaSiO_3$-Al IPC could persist after the imposed strains of a collision, because the Al would contain the failing ceramic, effectively localizing the damage. Another envisioned application is impact and blast resistant standoff walls for government, embassy and military FOBs. Conventional concrete is prone to cracking and spalling during explosions or small arms fire. The presented IPC demonstrates superior strength and much more graceful failure, thereby avoiding the danger of spalling shrapnel.

Bending tests did not display the same ultimate strength enhancement seen in compressive loading. Improvement was obtained in the form of load resistance after initial failure. This was likely due to the Al foam retaining the carbonated $CaSiO_3$ within its pores after the ceramic cracks. In turn, the crumbling ceramic inhibits the cells of the foam from collapsing. Again, the ability of the composite to bear load after peak failure increases the amount of energy the material can dissipate through a damaging event, further supporting its potential use on FOBs.

Ceramic-Metal Interface

The presence of an interlayer product between the ceramic and metal regions could potentially create more intimate joining to improve the mechanical properties of the composite. Thermodynamic simulation provided an inclination that certain solid phases might be stable given the processing conditions. Notably, $Al_2Si_2O_5(OH)_4$ was predicted at elevated concentrations of CO_2. (Fig. 3.9) To check this prediction, optical and SEM images and EDS chemical maps of the interface were collected. (Fig. 3.10-11). From the optical image of the polished interface, continuous contact between the Al

and ceramic was apparent. A finer particle size also seemed to be concentrated closer to the Al then in the bulk of the ceramic region, potentially allowing for particles to become entrapped in the Al surface roughness. The SEM image also showed near continuous contact between the two regions, except for some particle pullout attributed to polishing. The fracture interface had a few notable observations. First, the optical image showed that the two material regions had separated during destructive testing. The entire length of the Al foam strut was separated from the ceramic. A crack into the ceramic region was also apparent. Closer inspection on the SEM image revealed ceramic still adhered to parts of the Al foam strut. In particular the ceramic clusters are present in the Al surface pores and defect sites. This suggested that any adhesion between the two components was likely due to mechanical interlocking between the surface roughness of the Al and the carbonated $CaSiO_3$ particles. Chemical mapping across the interface did not show Al comingled with Ca, Si elements. This put the formation of an aluminum silicate species at the interface into doubt. XPS results supported the EDS findings, suggesting that an interlayer product did not exist even in small concentrations. Spectra collected at Al only, ceramic only, and the interface did not show any appreciable comparative chemical shift for the Al, Si, or Ca.(Fig. 3.12) Since the binding energies were the same at the interface as in the component regions, the only compounds present at the interface must have been the same as those in the bulk regions.

From the optical, SEM, EDS and XPS results, the interaction between the ceramic and Al appeared to be mechanical only. As previously mentioned, it was believed that

the ceramic portion bears the majority of the applied stress, and the Al acts to confine the ceramic's lateral expansion. This coupled with the microstructure observations, suggested the following failure mechanism. First, the ceramic cracked as peak stress was approached. Continued application of load then led to separation of the two components by splitting of the bulk ceramic from the small ceramic protrusions within the Al pores. Finally, the portions of the composite split off as some of the Al struts failed in tension, applied by the crumbling ceramic within the pores.

The discrepancy between experimental observation and thermodynamic simulation was attributed to two considerations. First, the predicted solid phases may have been thermodynamically stable at the input conditions, but the kinetics of the situation might not have been favorable. Literature for hydrothermal synthesis of $Al_2Si_2O_5(OH)_4$ stated that a minimum of 150˚C and 5 bar over 24 h was needed.[100] Increased temperature and pressure, with longer periods of time, might have yielded the predicted solid, but this would also affect the carbonation reaction. Second, the processing occurred in steps which made the real situation differ from the modelled one. For example, during infiltration, the Al was exposed to elevated pH $CaSiO_3$ suspension, likely increasing the passivating Al_2O_3 layer thickness. Al_2O_3 might have then been less susceptible to dissolution during the carbonation step, reducing the likelihood of Al containing products. Another potential discrepancy could be attributed to the location of water during the carbonation reaction. Water was believed to mediate the carbonation reaction. Briefly, the $CaSiO_3$ surface becomes wetted by water vapor, allowing carbonic acid to form at the ceramic surface. The leached calcium from

the $CaSiO_3$ allowed for reaction with dissolved CO_2, forming $CaCO_3$. It is possible that this reaction had a much greater driving force than the corresponding interaction at the Al surface. In effect, the incoming CO_2 might have preferentially reacted with the $CaSiO_3$, and once that reaction pathway became closed off due to product formation, there would no longer be dissolved calcium or silicon for the Al to interact with.

3.5 Conclusions

Compression strength averaged ~116 MPa across the three IPC types and load was resisted after failure past 35% strain. Both properties were markedly improved over the individual composite components. With average bulk density of 2.2 g/cm^3 and 116 MPa strength, the IPC fit between Al-polymer and Al-ceramic IPC property space. Evidence of chemical interaction between the aluminum and carbonated wollastonite was not found, suggesting that any adhesion was mechanical in nature.

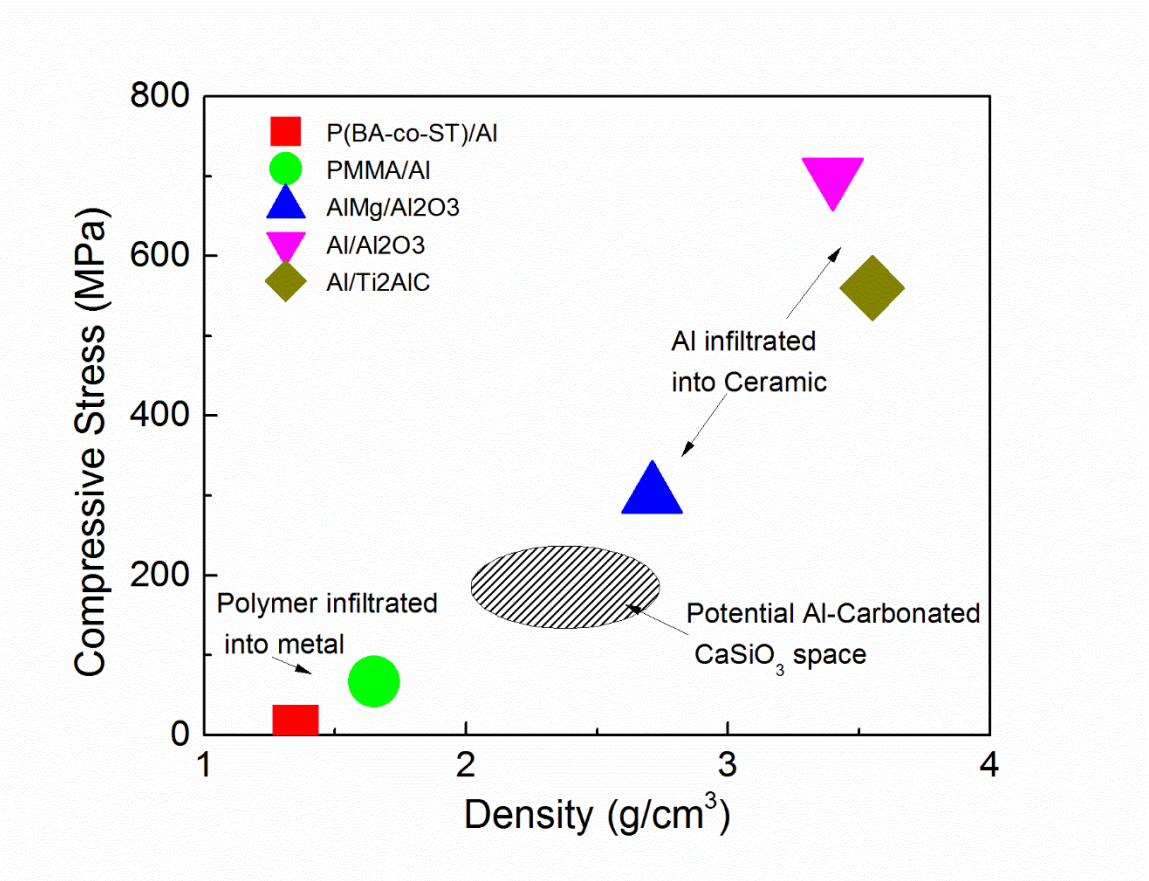

Figure 3.1. Al infiltrated IPC property space showing strength and density for polymer infiltrated into Al scaffold and Al infiltrated into ceramic scaffold IPCs. The crosshatch region denotes the target property space for an Al-carbonated $CaSiO_3$ IPC.

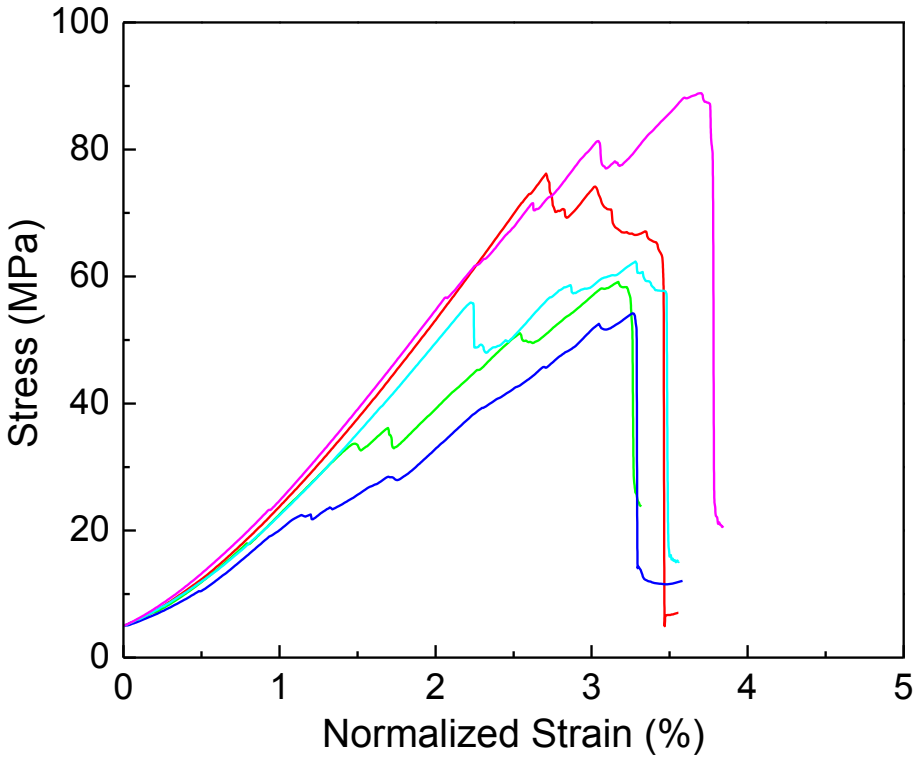

Figure 3.2. Compressive stress vs. strain for Pure samples.

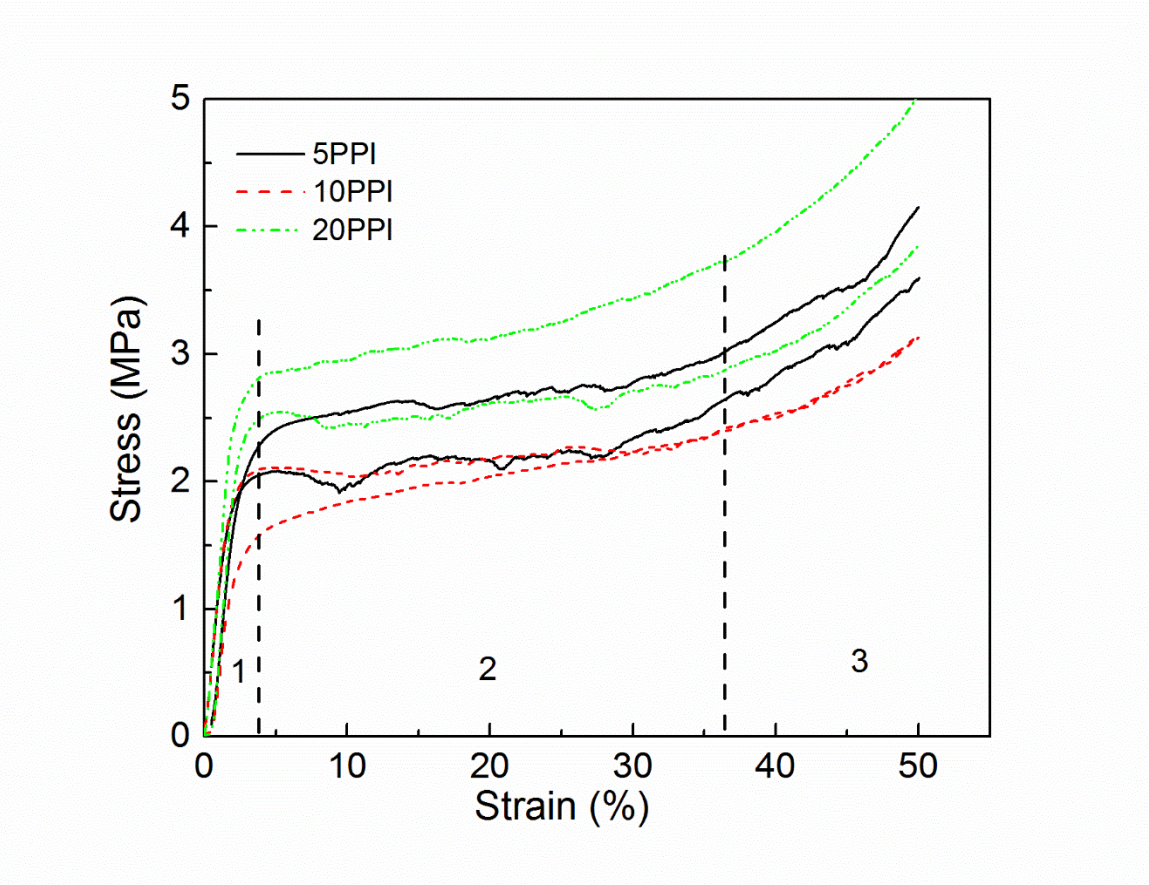

Figure 3.3. Compressive stress vs strain for Al foams, 5PPI, 10PPI, and 20PPI. Three distinct regions were observed, 1) an initial elastic region, 2) a deformation region associated with collapsing of the cells, and 3) a densifying region where the metal begins impinging upon itself.

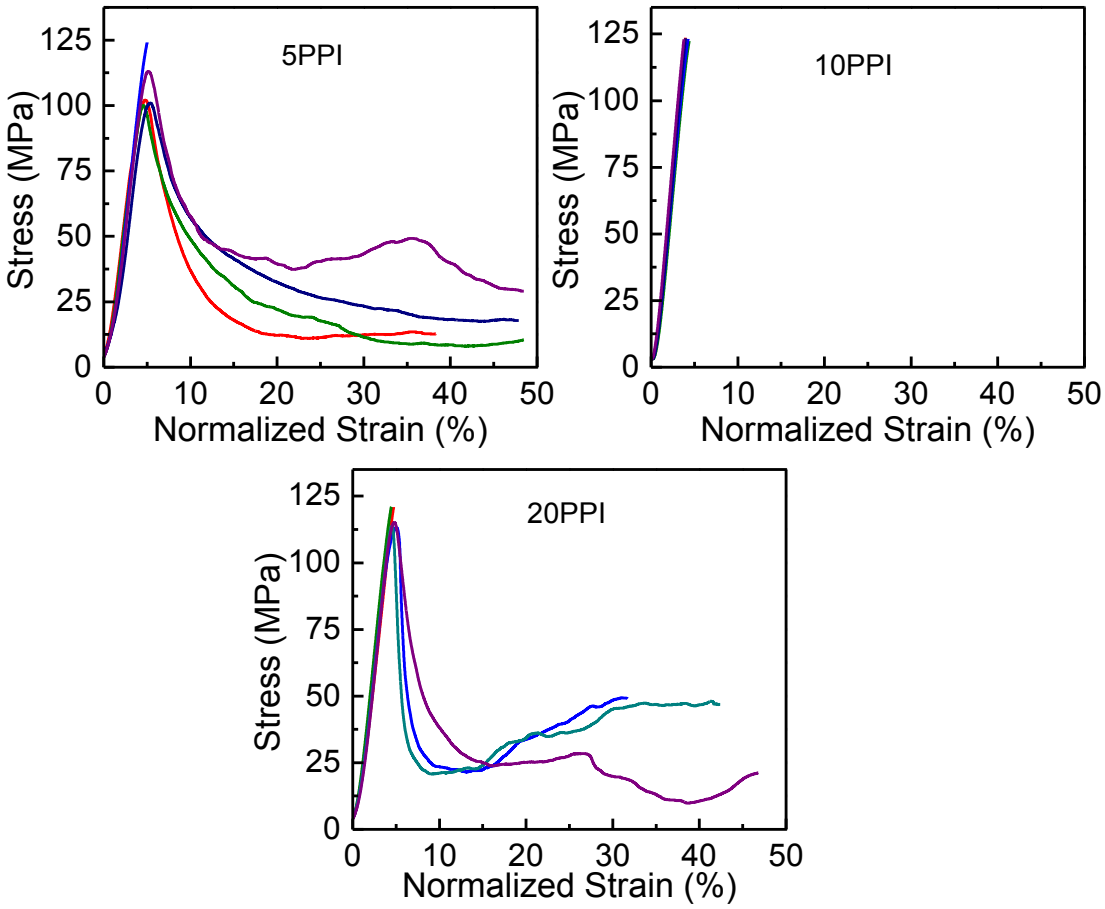

Figure 3.4. Compressive stress vs strain for 5PPI, 10PPI, and 20PPI composites. The 5 PPI and 20 PPI samples displayed stress resistance after failure. The 10 PPI samples all exceeded the capacity of the testing load cell.

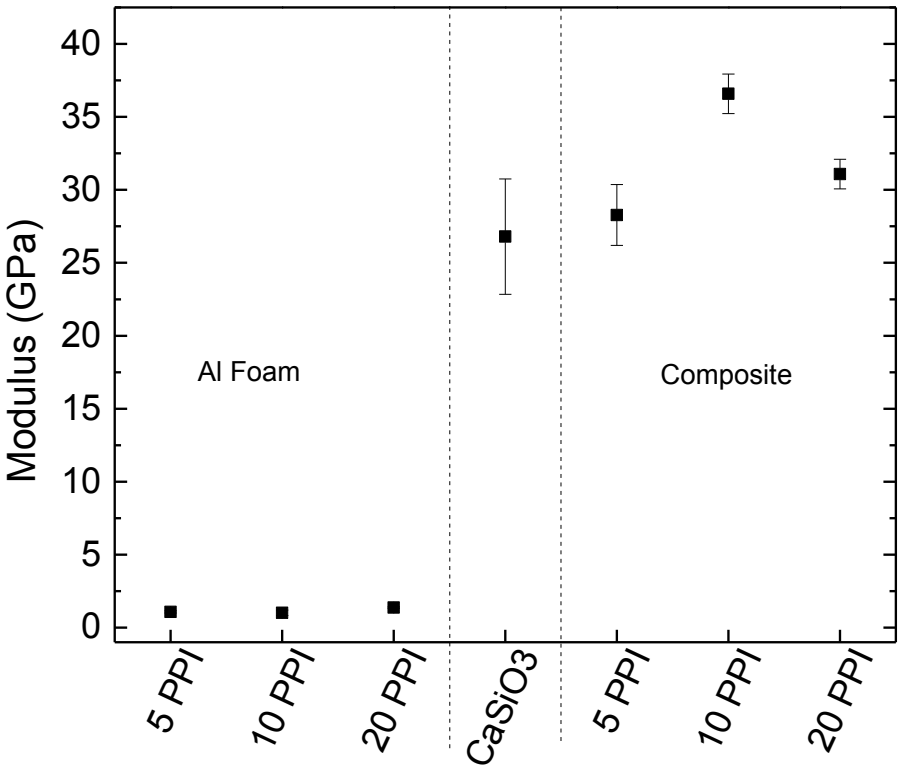

Figure 3.5. Average elastic modulus for components and composite samples.

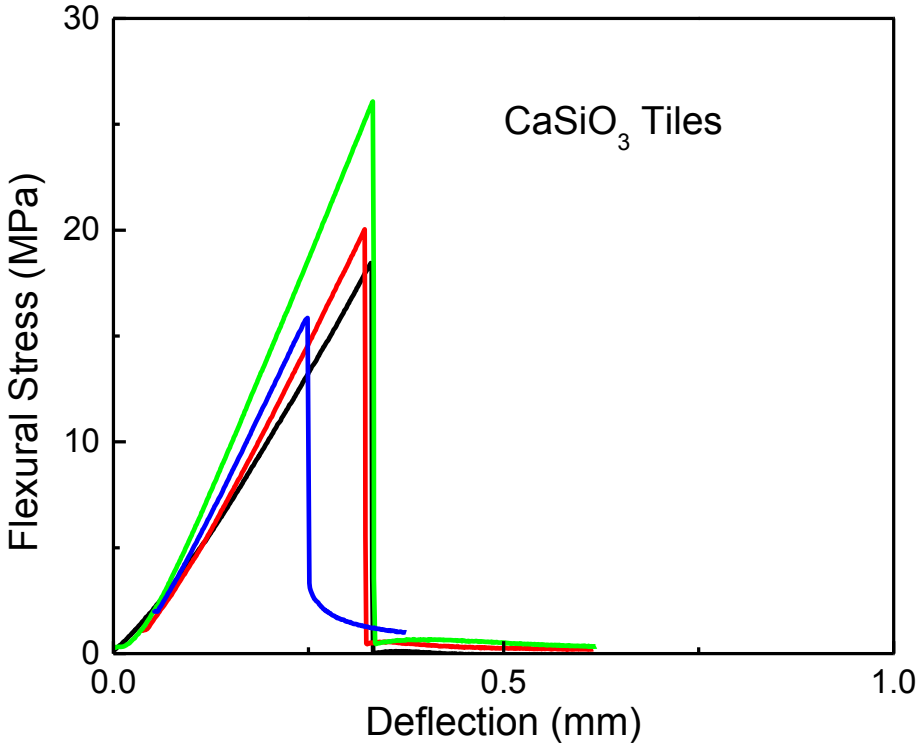

Figure 3.6. Flexural strength of carbonated $CaSiO_3$ tiles.

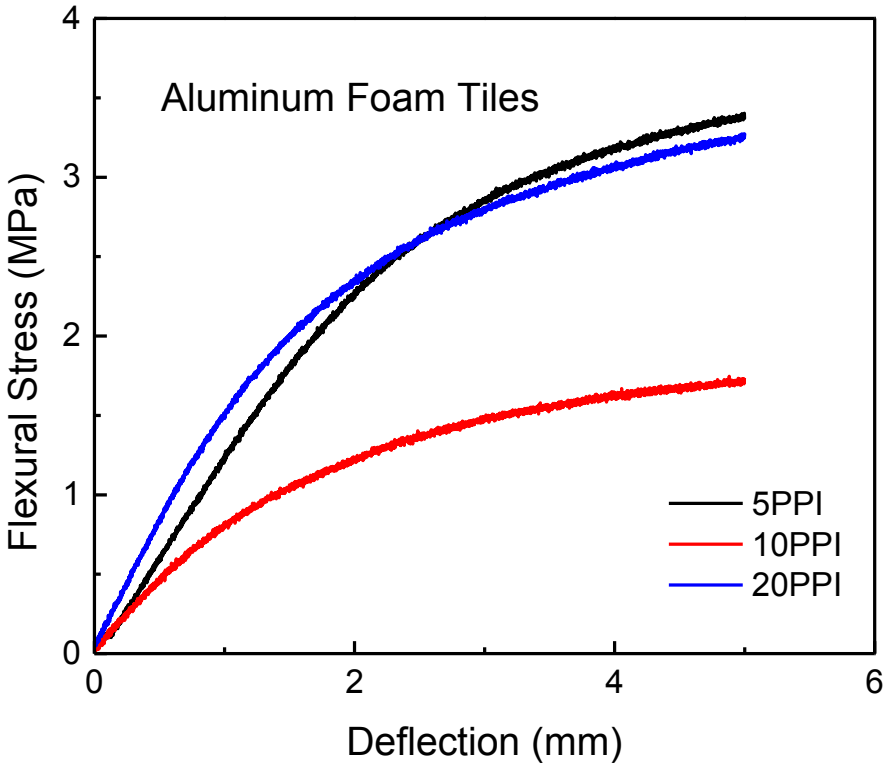

Figure 3.7. Flexural strength of Al foam.

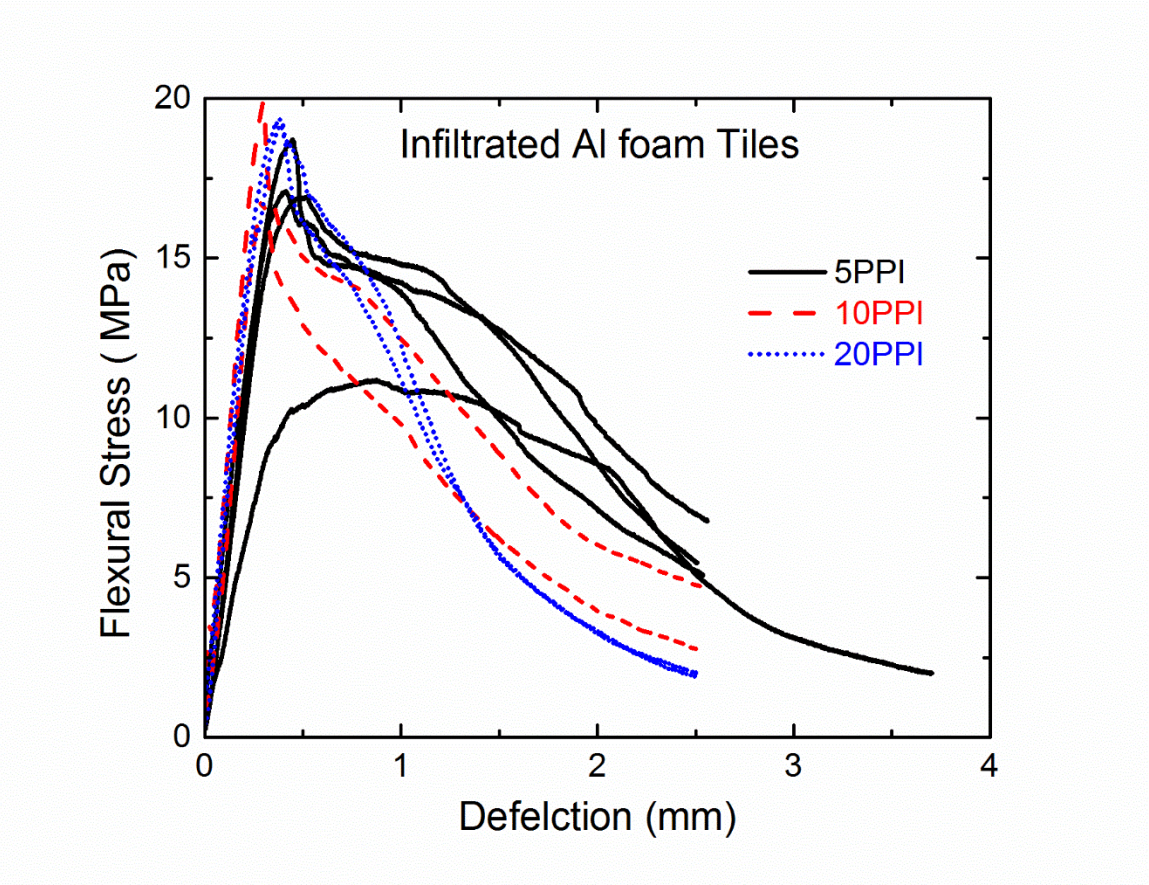

Figure 3.8. Flexural strength of Al – Carbonated $CaSiO_3$ composites.

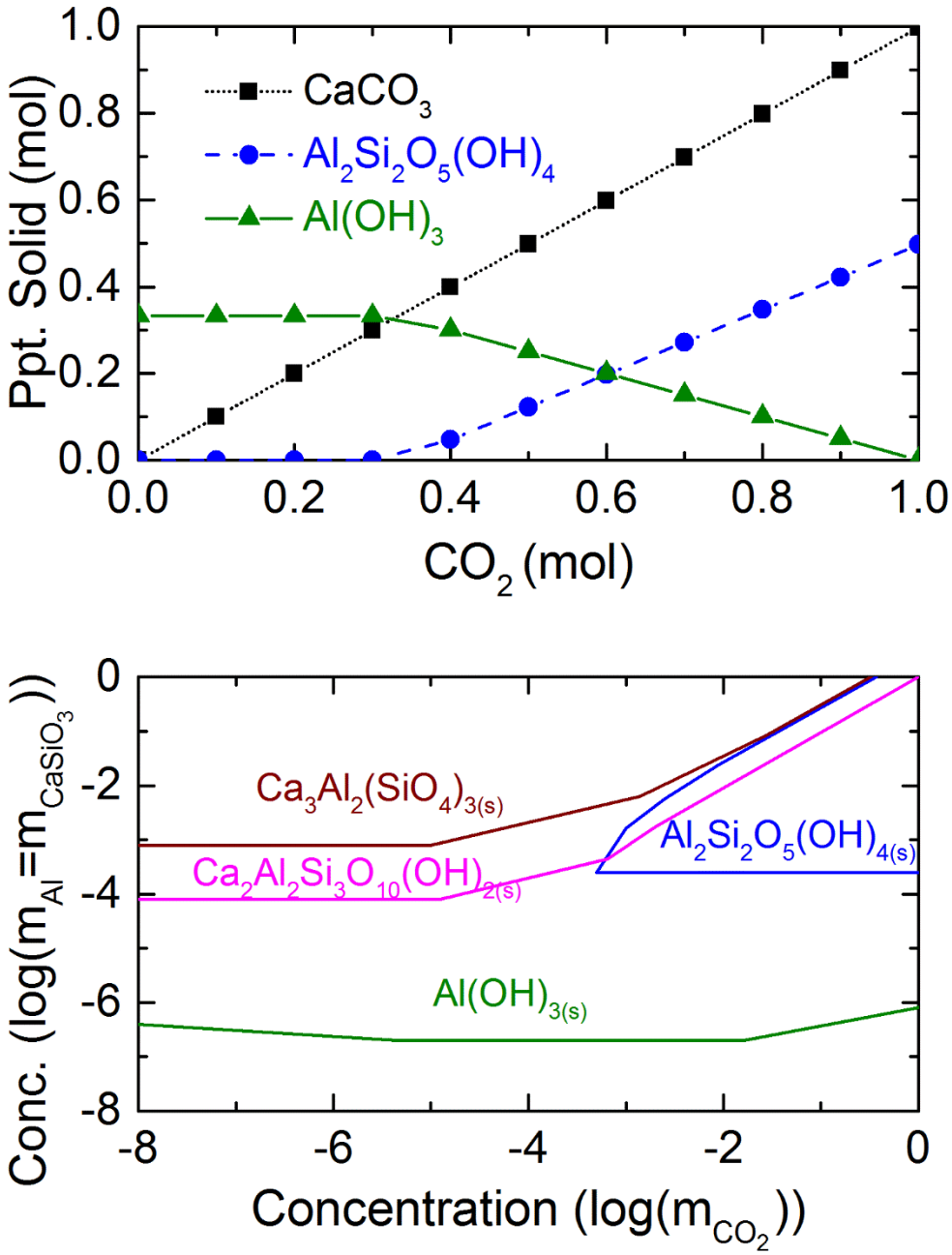

Figure 3.9. Survey (top) and chemical diagram (bottom) of the $CaSiO_3$ – Al system. The survey shows how precipitate yield is expected to change with CO_2 concentration. The chemical diagram details how the concentration of $CaSiO_3$=Al affects expected solids yield.

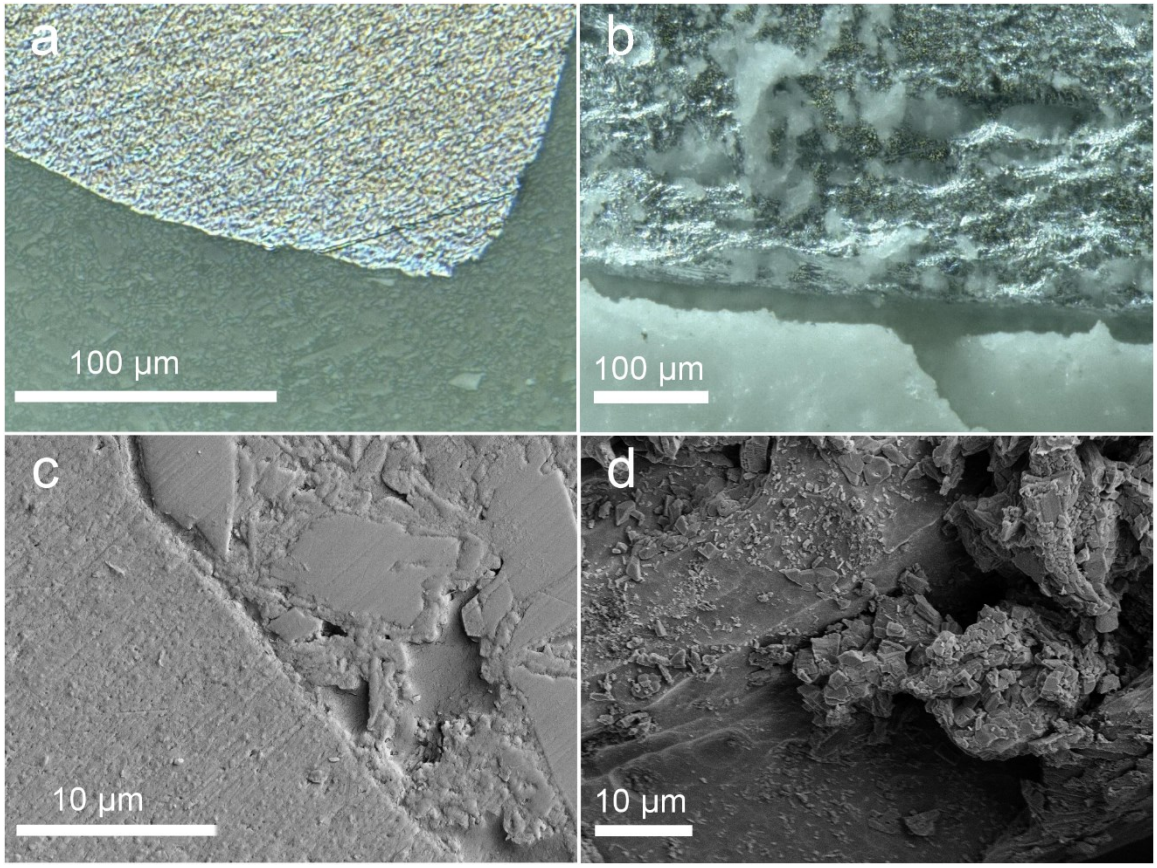

Figure 3.10. Optical images of polished (a) and fracture (b) surfaces of the composite interface and SEM images of the polished (c) and fracture (d) surface of the IPC interface. The polished interface indicated that there was good contact between the ceramic and metal portions of the composite. The fracture surface displayed evidence of separation of the ceramic and metal, cracking in the ceramic, and some ceramic separating from the bulk to remain adhered to the metal.

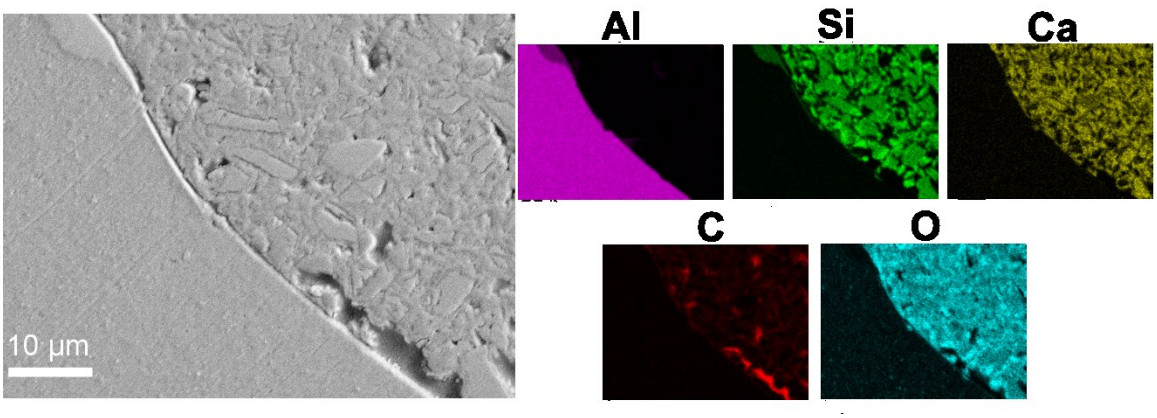

Figure 3.11. EDS chemical map of the composite interface. A clear division between Al and all the ceramic elements, Ca, Si, C, O, indicated that there was not an interface product.

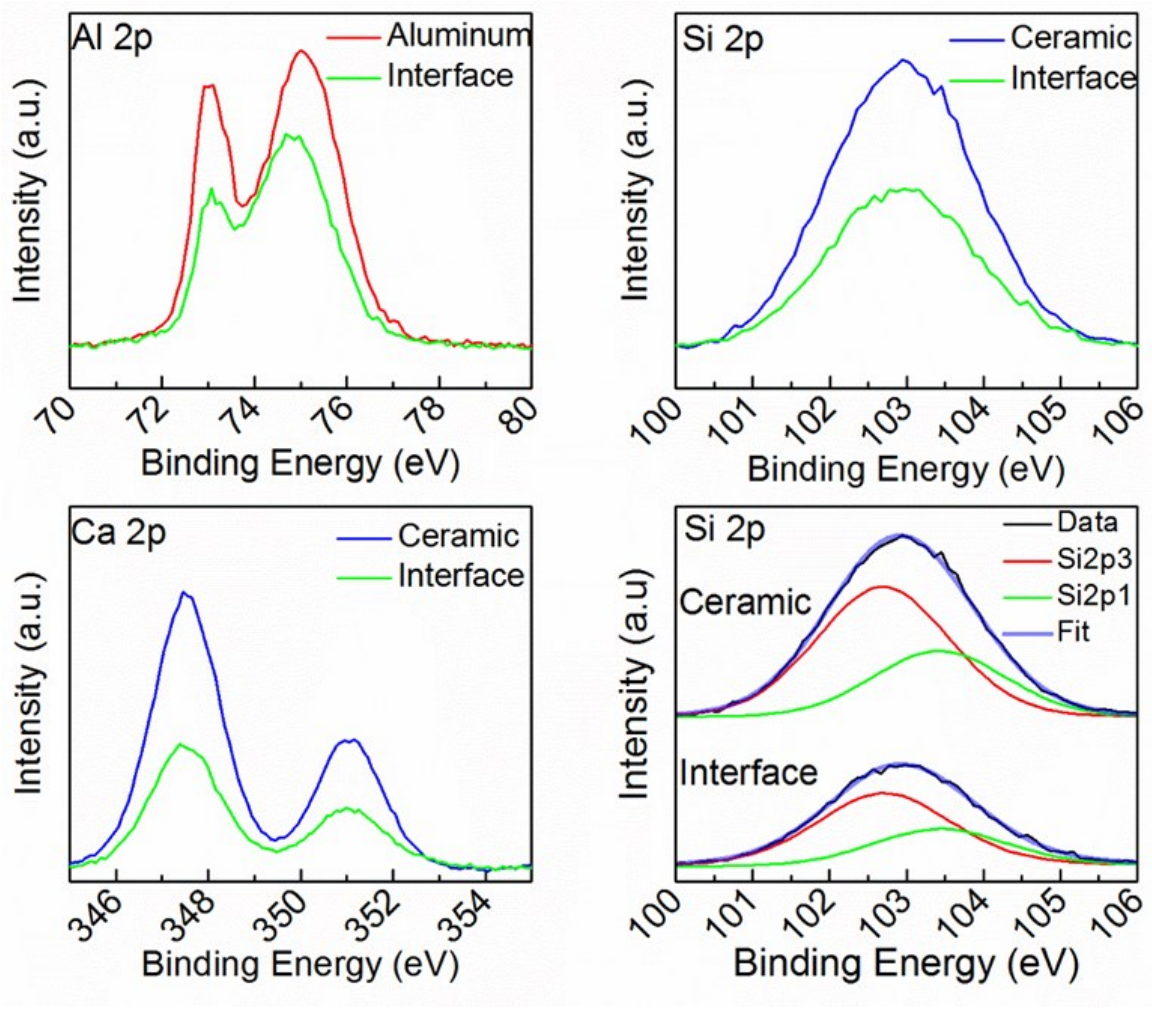

Figure 3.12. Comparison of XPS spectra taken from three regions in the composite, 1) ceramic, 2) aluminum, and 3) interface. No significant peak shifts in the interface region relative to respective bulk regions suggest no presence of unique interface compound. The lower right quadrant shows the matched doublet Si 2p3 and Si2p1 and resulting fit for the Si 2p spectra.

4. Al Foam Surface Treatment and Coating

4.1 Introduction

A novel metal-ceramic IPC fabrication route detailed in Chapter 2 and 3 represents a potential paradigm shift in composite manufacturing. The g-rHLPD process enables a wide range of materials combinations that were previously unobtainable by conventional processes due to its comparably mild conditions. These mild conditions provide the additional benefit of energy consumption reduction, CO_2 emission reduction, and overall cost reduction. This intersection of sustainability and process simplification is attractive, but the achievable properties of these IPCs must be improved if adoption is to occur. Thus, manipulation of the metal surface will be considered to improve interaction with the ceramic. This structure manipulation is anticipated to result in improvement of the bulk mechanical behavior of the composite.

Improving adhesion between the Al foam and carbonated $CaSiO_3$ within the IPC can be accomplished via chemical bonding or mechanical bonding. Chemical bonding was defined as the presence of a continuous region at the interface of the two component-materials of the composite that contained elemental composition of both component-materials. Mechanical bonding was defined as elementally discrete regions at the interface of the component-materials that were spatially interlocked, such that separation was not possible without significant deformation or destruction of one or both of the component-materials. As previously investigated in chapter 3, the interaction between the two component-materials appears to be mechanical. Since the

g-rHLPD process occurs in-situ, adding an additional step to provide chemical bonding is non-trivial. Any proposed chemistry would need to be compatible with both the particle suspending solution and the carbonation process. Thus, due to this anticipated complexity, only mechanical bonding enhancements will be considered.

From an energetics standpoint and assuming uniform contact at the interface, interaction between the Al and carbonated $CaSiO_3$ adds to the mechanical properties of the bulk due to the work required to separate them.[101] This fracture energy can be considered a combination of surface energy and energy absorption, with the surface energy term being dependent on the area of interaction.[102] It follows that increasing the area of interaction between two surfaces should thus increase the energy needed for fracture. The IPC will then be able to take in more energy before interface failure. This mechanically manifests itself as an increase in ultimate strength and/or an increase in strain prior to initial failure.[103]

The area of interaction between the Al and carbonated $CaSiO_3$ can be increased by either adding a higher roughness coating onto the Al or removing material from the Al surface to increase its inherent roughness.[104, 105] Many techniques exist for applying coatings on Al, such as spray coating, swab application, and immersion coating. Due to the structure of the Al foam, spray and swab applications were not considered. Within the bounds of immersion type processes, much of the literature focuses on inhibiting corrosion.[106–123] Typically the most important factor for protecting against corrosion is to form a continuous, dense coating. Most of these coatings do not provide a significant increase in roughness, and in some cases are smoother than the covered surface. Thus,

the literature was surveyed for coatings exhibiting comparatively higher roughness from the standpoint of its porosity and surface area. Zeolite coatings met this criteria, potentially providing a large increase in surface roughness compared to the untreated Al surface. Anodized coatings were also selected, representing a small change from the roughness of the untreated Al surface. To test increasing surface roughness through material removal, HCl etching was selected.

Zeolite coatings exist in many chemistries with processing pathways ranging between low temperature sol-gel to elevated temperature and pressure hydrothermal methods. Commonly, zeolites are used for filtering and catalytic applications due to their tunable molecular porosity. Recently, some effort has been spent towards utilizing zeolite coatings as corrosion and abrasion protection.[124–130] The coatings typically do not consume any of the substrate material. Good adhesion between Al substrates and the formed coatings has been reported.[126, 127, 129–132] Additionally, multiple layer growth has been reported, suggesting that the zeolite coating can both completely cover the Al substrate with an initial layer and provide large pores suitable for entrapment of the $CaSiO_3$ particels from subsequent layer growth.[124, 133] Synthesis conditions are typically below 200˚C temperature and utilize relatively benign chemical precursors such at silica and alumina with sodium or potassium hydroxide. Thus, a zeolite coating can potentially provide the needed increase in surface roughness while still fitting the sustainable processing goal mentioned in Chapter 1.

Anodizing Al is a common practice performed for corrosion and abrasion protection.[134] It is a conversion coating, consuming part of the Al substrate to form the

coating. The process typically creates a thick oxide layer with periodic porosity reaching through to the Al surface. Unfortunately, these pores are nanometer or smaller in diameter, which are too small to be useful for particle entrainment.[135] However, an increase in surface roughness might still be achieved by applying an incomplete anodized coating. It has been found that the coating grows from many simultaneously nucleated sites, then spreads to cover the surface.[136] Thus, short applications of electrical potential produces discontinuous coatings of isolated Al_2O_3 growths. Depending on morphology, porosity, and spacing of the Al_2O_3, anodizing could provide interlocking structure suitable for entrapment of $CaSiO_3$ particles. Increased porosity and surface roughness might also be achieved by prolonging the exposure of the formed oxide layer to the electrolyte solution after removal of the electric field, as dissolution of the oxide will occur.[137] The processing conditions needed for anodizing can be tailored to create a sustainable process. First, temperature is usually maintained near ambient, ~20˚C, requiring some form of heat dissipation to combat resistive heating of the solution. Second, the applied electric field must be controlled to reduce energy consumption. Constant current density throughout the process is needed for quality coatings, thus higher surface and larger components could also increase energy demands. Finally, even if both these issues can be accounted for, long processing times would result in unacceptable energy requirements. Thus, anodizing may be a suitable process for increasing the Al surface roughness if the desired morphology can be achieved in a short processing time.

HCl etching is commonly performed as a pre-treatment for subsequent coatings on Al.[138–143] Generally a simple immersion in concentrated HCl solution at ambient to slightly elevated temperature (30-50˚C) for a few minutes is sufficient to create a significant increase in surface roughness. Li et al. showed that in as little as 6 min in 4M HCl, the entire surface of the treated Al was covered with interconnecting roughness and pits. It was also noted that the roughness was more than superficial, extending into the substrate about 20 μm.[138] Initial surface features such as scratches, voids, etc. of the Al were also found to influence the nature of the etched surface.[140, 141] In particular, HCl was found to mainly attack dislocation sites on the Al surface.[144] Thus the Al foams, having inherent high surface, should be etched easily by HCl, providing a rough surface.

The objective of this chapter is to adapt processing routes for roughening the Al foam surface of an Al-carbonated $CaSiO_3$ IPC using three established methods. The three chosen methods are: (1) zeolite growth, (2) anodizing Al, and (3) HCl etching. Zeolite growth is a surface coating with the potential for greatly increasing the surface roughness of the Al foam. Anodizing is a conversion coating, and will create a smaller change in surface roughness. HCl etching is a mass removal process, and will create a significant change in surface roughness of the Al foam. Coating adhesion will be evaluated and the developed surface microstructure will be observed. The ability of the treated surfaces to promote a mechanical bond with infiltrated $CaSiO_3$ will be considered.

4.2 Experimental

Experimental Strategy

The three chosen methods of surface modification, zeolite growth, anodizing Al, and HCl etching will be applied first to Al 6101 squares in order to identify the best process conditions to later apply to Al foams. Thermodynamic simulation will provide predictions of solid precipitates for the zeolite, and estimates of corrosion rates of Al in the acids used in anodizing and etching. Mass change will be observed as process variables are changed for each treatment. Coating adhesion will be evaluated by a simple tape peel test. The developed surface microstructure will be observed optically and via SEM. The ability of the treated surfaces to promote a mechanical bond with infiltrated $CaSiO_3$ will be considered. These observations of treated Al squares will determine the best processing conditions for Al surface modification. The treatments will then be applied to Al foams and the resulting surface microstructure will be observed, noting any surface features suitable for entrapping infiltrated $CaSiO_3$ particles. Conclusions will be drawn about the potential for the surface treatments to improve mechanical interlock within the formed IPC.

Materials

Aluminum alloy 6061 1/8” thick sheet stock (McMaster-Carr, Robbinsville, NJ) was cut into 3/4”x 3/4” squares to serve as test surfaces for the applied coatings and cut into 2” x 6” pieces to serve as anodizing cathodes. Aluminum foam (Duocel® Alloy 6101-T6, ERG Materials and Aerospace Corp., Emeryville, CA) of 5 PPI and 10 PPI with relative

density 10-12% was used with the selected surface treatments. Water was filtered through a Progard® 2 and Q-guard® 1 purification system (EMD Millipore, Billerica, MA) prior to use. Sodium silicate solution (CAS# 6834-92-0 & CAS# 7631-86-9, Sigma Aldrich, St. Louis, MO) was used as a colloidal and polymeric silica source and a sodium source. Sodium hydroxide, NaOH (CAS# 1310-73-2, Fischer Scientific, Pittsburgh, PA) was as an additional sodium source and for pH adjustment. Alumina, Al_2O_3 (CAS# 1344-28-1, Sigma Aldrich, St. Louis, MO) was used as an aluminum source. Triethanolamine, TEA (CAS# 102-71-6, Fischer Scientific, Pittsburgh, PA) was used as a structure directing agent. Sulphuric acid, H_2SO_4 (CAS# 7064-93-9, Sigma Aldrich, St. Louis, MO) was used for the anodizing bath solution. Hydrochloric acid, HCl (CAS# 7647-01-0, Fischer Scientific, Pittsburgh, PA) was used for the etching solution.

Treatment Simulation

OLI Systems stream analyzer software (ver.9.0, OLI Systems, Inc., Cedar Knolls, NJ) was used to model each treatment reaction. The software used thermodynamic parameters obtained by analysis and regression of reported primary experimental results. Publications regarding thermodynamic modeling provide examples for this procedure.[90–94] A chemical diagram was generated to observe the possible thermodynamic products from the zeolite synthesis solution. Precursor inputs were as follows: 300 mols H_2O, 5 mols Na_2O, 1 mol Al_2O_3, 10 mols SiO_2, and 5 mols TEA. Pressure was set to 1 atm and temperature was varied from 25-100 ˚C. Corrosion rates were also simulated for 2 M H_2SO_4 and 4 M HCl to study the effect of the anodizing and etching solutions on the Al surface. Temperature was varied from ambient up to 100˚C.

Al Square Surface Preparation

Pre-coating treatments were performed to ensure that the Al square surface was relatively consistent between coatings. After cutting to size, the Al squares were washed with a Citranox® detergent (Alconox, White Plains, NY) solution in an ultrasonic bath (#FS60D, Fischer Scientific, Pittsburgh, PA) for 1 h. Then the squares were thoroughly rinsed with DI water and allowed to dry under ambient conditions. Prior to coating, the squares were submerged in 1M NaOH solution for 1 min, rinsed with DI H_2O, and allowed to dry in ambient conditions for approximately 10 min. The squares were then promptly placed in the treatment solution.

Zeolite Coating

Reaction solution for zeolite coating deposition was prepared as follows: A stock solution was produced in the following manner. First, 16 g NaOH was mixed with 370 g DI H_2O until dissolved. 9.4 g of Al_2O_3 was then added and stirred for approximately 5 min. After the Al_2O_3 appeared dispersed, 202 g of sodium silicate and 69 g of TEA were added. The resulting precursor solution had cation ratios corresponding to the following molar empirical formula: $5Na_2O:Al_2O_3:10SiO_2:300H_2O$:5TEA. The solution was covered and allowed to mix via magnetic stirring for a minimum of 24 h before use.

Coatings were applied in 100 and 300 ml perfluoroalkoxy alkane (PFA) containers (Savillex, Eden Prairie, MN), with 50 and 250 ml of reaction solution respectively. This amount was sufficient to completely cover the Al surface. Al squares and foams were placed on PFA supports (Savillex, Eden Prairie, MN) inside the PFA containers. Once the

reaction solution was added, a vacuum was pulled for about 5 min to ensure any trapped air was removed from the square surface and pore structure of the foams. The PFA containers were then sealed and placed in either a mechanical convection oven (model# MO1440C-1, Lindberg/Blue M, NC) or in a temperature controlled water bath (Buchi Labortechnik AG, Switzerland). Various temperatures (25-200˚C) and durations (0.5-8 h) were used to as shown in Table 4.1. After treatment, samples were rinsed in flowing DI-H_2O for 2 min then dried at 85˚C.

Anodized Coating

A Type II anodizing approach was used.[145] H_2SO_4 was added into DI H_2O to form a 2 M solution. A 1 L solution was placed in a PFA container, and then placed in a 20 ˚C water bath. A PFA impeller was used to agitate the anodizing solution. A 6061 aluminum alloy 1/8" thick sheet was used as a cathode material and it was cut to enable a 1:3 cathode:anode surface area ratio, which was needed for Type II anodizing. The cathode was attached with clip leads to the negative terminal of a variable DC power supply (XPower DC Power Supply 305D). The Al square to be coated was attached with a clip lead to the positive terminal of the power supply and immersed in the stirred anodizing solution. Current density was set at 1.2, 1.5, and 1.8 A/dm^2 and the immersion time was chosen as 5, 15, 30, and 60 min. After treatment, the samples were rinsed in flowing DI H_2O for 2 min and placed in an 85˚C drying oven for a minimum of 30 min prior to measurement. For the Al foams, the greatly increased surface area and bulk size required much greater current and potential than that needed for the Al squares and resulted in excessive heat generation. To maintain temperature at 20˚C,

the H_2SO_4 solution was cycled through a chiller (Refrigerated Circulator, model #F32 Eh, Julabo, Germany).

Acid Etch

HCl was added into DI H_2O to form a 4 M HCl solution. The solution was magnetically stirred and used at ambient temperature. Five Al squares were placed on PFA supports and submerged in the solution for 1, 2, 3, 4, and 5 min. After etching, samples were immediately immersed in a 5 L water bath for 2 min, then rinsed with flowing DI-H_2O for 1 min. Samples were then dried at 85˚C for a minimum of 30 min before subsequent measurement. The mass loss and surface change was observed to identify the appropriate etching time for the Al foams.

Characterization Sample Preparation

Samples were prepared for imaging and chemical analysis via polishing. Representative pieces of samples were first cut to small size using the precision cutter. After drying, the samples were placed in 1" diameter cylindrical molds and infiltrated with mounting epoxy (EpoThin 2 Epoxy System, Buehler, Lake Bluff, IL). Vacuum was then pulled on the freshly poured epoxy/sample containing molds using a Cast N' Vac 1000 Vacuum Impregnation System (Buehler, Lake Bluff, IL) for ~5 min, then left in ambient conditions for 24 h to harden. The hardened epoxy mounted samples were then ground and polished on an EcoMet 250 Grinder-Polisher (Buehler, Lake Bluff, IL). The typical polishing schedule used was as follows: 1) 320 grit SiC paper, 30 1/s head speed, 240 1/s base speed, complementary head/base direction, 5 min. 2) 6 μm

polycrystalline diamond suspension (DIAMAT, Pace Technologies, Tucson, AZ) on Tri-Dent cloth (Buehler, Lake Bluff, IL), 30 1/s head speed, 150 1/s base speed, complementary head/base direction, 6 min. 3) 3 µm polycrystalline diamond suspension (DIAMAT, Pace Technologies, Tucson, AZ) on Tri-Dent cloth, 30 1/s head speed, 150 1/s base speed, complementary head/base direction, 4 min. 4) 0.05 µm polycrystalline diamond suspension (DIAMAT, Pace Technologies, Tucson, AZ) on Micro-Cloth (Buehler, Lake Bluff, IL), 30 1/s head speed, 150 1/s base speed, contra head/base direction, 2 min. After polishing, the epoxy was cut away from the samples.

Characterization

Mass change was recorded for each coating attempt. Crystalline surface phases were identified using XRD performed on a Bruker D8 Discover (Bruker AXS Inc., Karlsruhe, Germany) with CuKα radiation (λ = 1.514 Å), parallel beam in the range 0-80˚ (2θ) with a 0.018˚ step size and 1s dwell time. Optical microscopy using a VHX-1000 digital microscope (Keyence, Elmwood Park, NJ) was used to ascertain the properties of the coating. Field emission scanning electron microscopy (FESEM) (Carl Zeiss, Oberkochen, Germany) was used to closely inspect the surface microstructure and to observe polished cross-sections of coating/aluminum interface. Sample surfaces were sputter coated with 10 nm thick gold coatings (Electron Microscopy Sciences, model# EMS 150T ES, PA) using a sputtering current of 20 mA for 5 min. Energy dispersive spectroscopy (EDS) was also used to ascertain chemical composition of the observed surfaces. Accelerating voltage was increased to 10kV to increase the collected counts/sec and the aperture was widened until ~1000 counts/sec was attained.

Typically, data was collected for ~10 min prior to compiling elemental maps. Adhesion of the coatings was qualitatively evaluated via ASTM D3359 Standard Test Methods for Measuring Adhesion by Tape Test following test method B – Cross-cut Tape Test.[146]

4.3 Results

Zeolite Coating

Thermodynamic simulation suggested solid precipitates of various Al:Si ratios were possible given the precursors input. (Fig. 4.1) At the synthesis pH ~12.2, three solids were predicted, $NaAlSi_3O_8$, $NaAlSi_2O_8$, and $Na_2Al_2Si_3O_{10}*2H_2O$. Up to ~75˚C, a mix of $NaAlSi_3O_8$ and $NaAlSi_2O_8$ was expected. Between 75-80˚C only $NaAlSi_2O_8$ was suggested, and at temperature between 80-100˚C only $Na_2Al_2Si_3O_{10}*2H_2O$ was expected. If the pH was increased greater than ~13, $NaAlSiO_4$ and $Al(OH)_3$ both became viable precipitates.

Table 4.1 details the run progression leading to optimal coating conditions. Initial attempts (Zeo1 and 2) at 100 and 200˚C for 8 h failed to produce a well adhered coating, instead significant mass was lost, -2.82 and -20.83% respectively, and flaking/spalling of the reaction products was observed. Milder conditions were subsequently applied (Zeo3 and 4) via 95˚C for 2 and 5 h with mass gain of 0.67 and 3.01% respectively. Complete coverage of the surface was observed, but an easily removed second layer of product also formed. (Fig. 4.2. Zeo3 and 4) Shorter durations were used in an attempt to only create the single, better adhered layer. Runs at 0.5 and 1 h (Zeo5 and 6) had 0.32 and 0.68% mass gain and showed complete and near-

complete single layer coverage respectively. (Fig. 4.2. Zeo5 and 6) Both these coatings qualitatively appeared ideal for mechanical interlock, as large spaces and pores, 10-100 µm in diameter, were present for infiltrated $CaSiO_3$ particles to embed in. Two runs were carried out at room temperature (Zeo7 and 8) as a check that ambient conditions could not be used. No appreciable mass change, 0.02 and 0.01%, or visual surface change was observed.

Heating rate of the reaction solution was considered, as it was unlikely that the solution would reach the oven set point during the 0.5 and 1 h runs. A reaction container with 50 ml of water was placed in the 95˚C oven and the water temperature was measured periodically. After 150 min the solution had still not reached the desired set point. (Fig. 4.3 95˚C Oven) The measuring procedure likely inhibited the heating, but it was still believed that greater than 1 h was needed to reach set temperature within the convection oven. Thus, the actual temperature for the reaction was closer to 40-60˚C, and subsequent short duration runs were set with that range in mind. To achieve better temperature control for short reaction durations a water bath was used. The higher thermal mass of the water relative to air allowed for much faster and uniform heating of submerged containers. (Fig. 4.3 70˚C Bath) A set point of 70˚C was reached in less than 35 min. Two runs using the 70˚C water bath were conducted (Zeo9 and 10) for 0.5 and 1 h. Mass gain, 0.64 and 0.67%, was on par with and that of the same duration in the 95˚C oven. (Table 4.1) Coating coverage appeared greater for Zeo9 and 10 compared to Zeo5 and 6, likely due to the faster heating rate. In other words, even

though the temperature set point for Zeo5 and 6 was higher, the actual temperature was likely far lower, in accordance with Fig. 4.3, resulting in a slower coating growth.

XRD on the Zeo4 was conducted to determine the phase of the formed coating. (Fig. 4.4) The dominant peaks at 38, 44, 64 and 78 2-theta were attributed to Al, matching PDF#97-024-0129. The minor peaks at 18, 20, and 40 2-theta matched Al(OH)3, PDF# 97-003-8108. The low angle minor peaks at 10, 11, 16, 23, 26, and 31 2-theta matched Zeolite Y, PDF# 97-004-0927.

The 0.5 h samples (Zeo5 and 10) coating coverages were compared at high magnification using FESEM. (Fig. 4.5) Zeo5 had areas of exposed Al about 50 µm across between clumps of adhered coating. (Fig. 4.5 a) At higher magnification, within areas of near complete coating, spacing greater than 10 µm between coating clumps was also seen. (Fig. 4.5 b) Zeo10 did not have significant exposed Al areas, displaying near complete coating. (Fig. 4.5 c) Higher magnification revealed some open spacing between coating agglomerates, with the greatest gap being less than 5 µm. (Fig. 4.5 d)

Adhesion was qualitatively tested for squares coated for 0.5 h in the 70˚C water bath. Coating removal was evaluated via ASTM D3359 test method B. Percent removal of the coating after testing was determined to be in the 5-15% range, earning a 3B rating. (Fig. 4.6) This suggested that the coating had above average adherence.

Al foam cubes were processed at 70˚C for 1 and 0.5 h (Zeo11-13). Coatings appeared uniform from visual inspection and were apparent throughout the foams. Comparison between un-coated and coated foams was observed via optical microscopy

and FESEM. (Fig. 4.7) A notable increase in surface texture was seen via low magnification images of the un-coated and coated foam. (Fig. 4.7 a and b) The coated surface was imaged at higher magnification, Figs. 4.7 c and d, showing an abundance of sites for interlock of infiltrated suspension particles. Polycrystalline tubular growths were also observed, possible indicating that an intermediary structure preceded crystallization. A polished cross-section of the coated Al Foam (Zeo13) displayed a few features of the coating. (Fig. 4.8) First, there appeared to be good contact between the coating and the foam along the majority of the interface, however the coating was not continuous across the entirety of the interface. Second, the coating extended about ~50 µm from the Al surface. Third, the coating had porosity throughout and at different scales. Pores of about 1 to 10 µm were prevalent across the observed area.

Anodized Al

The corrosion rate of aluminum in 2 M H_2SO_4 was simulated. (Fig. 4.9) At the processing temperature, 20˚C, a corrosion rate of ~2.375 mm/yr was predicted. At 30˚C, the corrosion rate was ~3.125 mm/yr. Thus, a 10˚C increase in processing temperature resulted in about a 31% increase in corrosion rate.

Table 4.2 summarizes the effect of the processing variables on mass gain. Very little mass gain was observed across all conditions. All samples processed at 1.2 A/dm^2 (An1-3, An10) and 1.8 A/dm^2 (An7-9, An12) did not exceed 0.1% mass gain, regardless of the duration. The samples processed at 1.5 A/dm^2 (An4-6, An11) gained the most mass with increases of 0.03, 0.09, 0.17, and 0.39% at 5, 15, 30, and 60 min respectively.

Based on the mass gain for An11, and assuming a 3.95 g/cm^3 density of Al_2O_3, the volume of this coating was 3.29x10^{-9} m^3. Assuming uniform growth on all sides of the square and only outward from the initial square size, this equated to a 1.11 µm thick coating.

Optical images of the anodized squares processed at varying current density over increasing time were also recorded. (Fig. 4.10) Little change was observed for the samples processed at 1.2 and 1.8 A/dm^2. Some surface scratches, pitting and defects were present across these samples, but were not attributed to the anodizing process. Samples processed at 1.5 A/dm^2 did present observable change with increasing duration. Between 5-15 min of processing, the striations from factory surface finishing became occluded. At 30 min a fairly continuous coating with a high number of pores became apparent. At 60 min, the number of pores appeared to decrease, possibly due to continued thickening of the coating. The formation or lack of formation of the coatings appeared to follow the mass gain data presented in Table 4.2.

XRD of An11 did not show any crystalline aluminum oxide. (Fig. 4.11) The dominant peaks at 38, 44, and 64 2-Theta corresponded to Al, PDF#97-024-0129. A hump between 20 and 30 2-Theta was apparent, suggesting the presence of an amorphous or poorly crystalline phase.

SEM images of the 1.5 A/dm^2 current density processed squares (An4,5,6 and 11) were also collected. (Fig. 4.12) At 5 min of processing time, ~1 µm channels and pits were prevalent on the surface. (Fig. 4.12 a) At 15 min of processing time, the channels

and pits appeared to have increased roughness within them. (Fig. 4.12 b) At 30 min of processing time, the channel and pore roughness was replaced by smooth surface. (Fig. 4.12 c) After 60 min of anodizing, the channels and pits of the surface appeared to have somewhat filled in from coating growth. (Fig. 4.12 d)

Adhesion of coatings applied at 1.5 A/dm^2 for 60 min was assessed by an ASTM D3359 Tape Peel Test Method B. (Fig. 4.13) Very little coating was removed, with only small chips along the razor blade cut. This earned the coating a 4B rating for less than 5% removal. This indicated that the coating was very well adhered to the Al surface.

The 1.5 A/dm^2 current density anodizing process as the highest mass gain was observed with this condition on the Al squares. A 60 min run resulted in 0.28% mass gain. The anodic coated Al foam was compared to an uncoated foam with SEM. (Fig. 4.14) Low magnification showed long cracks running parallel with the respective Al strut axis on the coated foam, whereas the uncoated foam had shallow striations seemingly randomly oriented. (Fig. 4.14 a and b) Closer examination of a continuous portion of the coated surface revealed periodic 'dimpling' with occasional plateau regions, both on the order of ~10 µm. (Fig. 4.14 c) Along the cracks in the coating, the morphology varied. A comparably smooth layer appeared to cover the 'dimpled' surface observed in the non-crack region. (Fig. 4.14 d)

A polished cross-section of the anodic coated foam revealed a thick, dense Al oxide layer. (Fig. 4.15) EDS elemental mapping showed a region of Al and O between the bulk Al and mounting epoxy indicated by C. The layer was about 30 µm in thickness.

Cracking was apparent at the contact between the Al oxide layer and the mounting epoxy. The crack likely formed during the polishing procedure.

HCl Acid Etch

Simulation predicted a rapidly increasing corrosion rate as temperature increased. (Fig. 4.16). Processing was carried out at ambient temperature, 20-25˚, indicating a corrosion rate of 3-4 mm/yr. Surface removal rates of about 35mm/yr were predicted if the etching solution was heated to 100˚C.

Table 4.3 detailed the effects of immersing Al squares in 4M HCl for increasing time. As expected, extending the immersion time led to an increase in mass loss with 1, 2, 3, 4, and 5 min resulting in -0.029, -0.030, -0.060, -0.109, -0.216% mass lost respectively. Mass loss was calculated in terms of the Al square surface to provide some inference for the higher surface area cubes. Etch times of 1, 2, 3, 4, and 5 min produced 0.923, 0.932, 1.86, 3.467, and 6.75 g/m^2 removal respectively.

Optical images of the Al squares etched for 1-5min were recorded. (Fig. 4.17) Little change could be observed from 1 to 4 min. At 5 min some pitting became apparent. Thus, the surface change due to the observed mass *loss* was deemed to be on the order of a μm or smaller for the Al squares.

XRD of the 5 min etched Al square showed no evidence of any crystalline phases other than Al. (Fig. 4.18) The peaks at 38, 44, 64, and 78 2-Theta were matched with Al PDF# 97-024-0129.

Comparison of an untreated Al foam and an Al foam etched for 5 min was conducted with optical microscopy and SEM. (Fig. 4.19) The foam lost 1.946 g, about 10% of its initial mass during the etching process. At low magnification a stark difference was observed between the untreated and etched Al foam surface. (Fig. 4.19. a and b) The etched surface appeared to have two relative sizes of pitting. A few large pits, ~100 μm diameter, penetrating deeply into the Al were situated between sections of numerous smaller, more superficial pits ranging from <1-10 μm in diamter. In contrast, the untreated surface was relatively smooth, with prevalent shallow grooves running in all directions. At higher magnification, the region between the deep pits had many squared terrace-ledge-step features. (Fig. 4.19 c,e, and g) This sharp edged and angled crystalline microstructure ranged in size from about 10 μm to <1 μm, and had voids and openings about 1 μm in diameter as well. Within the deep pits, a smooth surface was exposed, with the sharp edged, angular terrace-ledge-step features surrounding and beneath it. (Fig. 4.19 d,f, and h) Overall diameter of the pits varied greatly, with some areas 200 μm across and others less than 50 μm. The smooth surface appeared to be relatively thin and layer-like in structure. A polished cross-section of the HCl etched foam showed that the surface roughness was about 5-10 μm from peak to trough. (Fig. 4.20) Lateral protrusions and voids were also observed along the entire surface, about 1 μm in size. EDS of the cross-section indicated that the surface was predominantly Al with no significant oxide growth. Si and O were present adjacent to the Al region due to silica reinforcing particles in the mounting epoxy.

4.4 Discussion

Zeolite Coating

Formation of the coating required relatively mild conditions. Initial attempts in hydrothermal conditions (100-200˚C) caused extensive dissolution of the Al surface, resulting in flaking and surface layer removal. This suggested that the corrosive action of the NaOH was enhanced at these increased temperatures, and the increased rate of liberation of Al and Al_2O_3 from the surface was far greater than any coating deposition. Solids precipitate formation simulated below 100˚C temperature predicted various sodium aluminate species to be possible. (Fig. 4.1) Processing at lower temperature, 95˚C, demonstrated that precipitate formation was evident at the surface. Short processing durations showed many individual nucleation sites, leading to local polycrystalline growths reaching tens of μm in diameter prior to impingement of neighboring clusters. (Fig. 4.2 Zeo5) Cluster growth appeared to continue, filling in open surface until the majority of the Al was covered. (Fig. 4.2 Zeo6) Second layer growth began between 1-2 h of processing time, and was easily separated from the surface layer, indicating that the shorter duration was favorable for the purpose of providing increased surface roughness. (Fig. 4.2 Zeo3 and 4)

Closer examination of the surface at short reaction duration, 0.5 h, showed that increasing the heating rate lead to much better coverage and more uniform cluster size. (Fig. 4.5) Additionally, some indication of the formation mechanism was apparent in the SEM images. In particular, tubular structures more easily observed on the surface of the

coated Al foam (Fig. 4.7 d) were also observed on the coated Al square surface. (Fig. 4.5 d). Scrutiny of the surface structure reveals that many of the crystal clusters were oriented in tube shape, suggesting that they were likely preceded by a smooth, cohesive tube. This deviates from findings in the literature using similar process parameters. Calabrese et al. described a formation mechanism from observation of samples reacted in the same synthesis solution for 8 h at 95˚C.[133] The authors reported homogeneous growth, suggesting that all portions of the surface were coated simultaneously. TEA was suggested to act as a complexing agent, orienting aluminate and silicate ions in solution, as well as mediating nucleation at the Al surface. From this viewpoint, coating growth was attributed to chemical reaction between the aluminate and silicate species, leading to intergrown, packed crystal zeolites. The observed tubules in the current work suggest a somewhat different formation mechanism. First, during mixing of the precursor solution, TEA likely mediated the coordination of Si and Al ions, as similarly suggested by the literature. Upon addition of the Al square, a favorable site for coordination of the TEA-Si-Al intermediary on the Al surface was exposed via the dissolution action of the NaOH, potentially mediated by sodium ions.[106,132] Next, additional polymeric TEA-Si-Al compounds likely joined the surface group, forming a tube network. With increasing temperature and time the sub-units of the tube began to crystallize, resulting in polycrystalline tubular structures. At the same time as the tube growth and crystallization, zeolite precipitates likely form in solution, resulting in non-tubular shaped particles and clusters accruing on the surface as well. This proposed mechanism may also account for the significant, multi-scale porosity observed in the

coated Al foam cross-section images. (Fig. 4.8) Briefly, if each cluster was the culmination of many tube-like structures intersecting and connecting, there would have to be spacing between them similar to that observed in packing of high aspect ratio particles. Fortunately, the scale of the spacing observed in the cross-section suggests that the pores may be large enough to accept and entrap infiltrated $CaSiO_3$ particulate.

Anodized Coating

The tested range of process parameters indicated that a current density of 1.5 A/dm^2 was ideal, with increasing mass and coating coverage expected over longer durations. (Table 4.2 & Figs. 4.10 and 12) The lack of mass gain and coating at the 1.2 A/dm^2 and 1.8 A/dm^2 current densities may be explained due to the formation mechanism of anodic coatings. First, clusters of oxide nuclei initially form at high energy sites on the Al substrate surface, driven by the applied potential. These initial clusters grow outward at the same time that more oxide nuclei form across the surface.[147] Once the surface is fully covered, growth begins upward, away from the substrate, with central pores in the each oxide cluster allowing charge to continue flowing. Throughout the coating process, sulphuric acid attacks the oxides, counteracting their formation and growth.[148] If the applied current density is too low, the rate of oxide formation may not be sufficient to overcome the acid attack, resulting in little net coating deposited. Conversely, larger current density might allow for oxide coating formation to greatly exceed sulphuric acid dissolution, resulting in a very dense initial coating. Too dense of an oxide coating would result in high resistance and secession of charge flow, also resulting in little net coating deposition. The higher current density may also cause

excessive local heating of the Al surface and nearby solution. As shown in Fig. 4.9, increasing temperature would in turn increase the corrosive action of the H_2SO_4, reducing the amount of non-dense oxide formed and forming. A middling current density would allow for oxide formation to exceed acid dissolution, but still allow the needed pores to form for continued current.

Comparison of the uncoated foam and anodized foam surfaces showed a relatively small change in surface roughness. (Fig. 4.14) The majority of the coating did not have large sites that might entrap infiltrated particles. Only the axially running cracks presented large enough structure for large particle inclusion. The rest of the anodized surface appeared to have many concave 'dimples'. These features were likely oxide 'cells' as reported in the literature.[149] The polished cross-section also showed that the coating only had superficial features, with no deep pores or features apparent across the oxide layer. (Fig. 4.15) Thus, the anodized surface represents a very small change from the inherent roughness of the untreated Al foam surface, and infiltrated particles will likely only anchor at the more macroscopic layer cracks.

HCl Acid Etch

Etching for 5 min removed a significant amount of material from the Al foam surface, ~10% mass loss, compared to the Al square surface mass loss of ~0.2%. Based on the mass lost per surface area of the 5 min etched Al square, the foam was expected to lose closer to 2%. The large difference was likely due to a few factors. First, the porous nature of the foams likely led to some local areas of increased temperature

inside the foam. As seen in Fig. 4.16, an increase in temperature would certainly put the amount of mass lost well beyond the expected amount. Second, since the entire surface of the Al foam was curved, and since it had about 2 orders of magnitude greater surface area than the squares ($2.7x10^{-2}$ vs $3.2x10^{-4}$ m^2 respectively) , there was likely a higher density of energetically favorable surface cites for corrosion to initiate at.[150] Thus, the rate of corrosion would be comparably higher for the Al foam then the same amount of Al square.

The structure obtained through etching should allow for particle entrapment. The large pitting, ~50-200 µm, may allow for clusters of $CaSiO_3$ to become anchored at the Al surface, and the smaller, more superficial pitting, ~1 µm, may be suitable for finer particle entrainment. (Fig. 4.19) The observed terrace-ledge-step features were likely a consequence of differing rates of corrosion across the surface. Crystal and phase boundaries, line and point defects, and increased concentrations of alloying elements are all sites of higher surface energy that would corrode at a higher rate than a bulk surface site.[151, 152] This local difference in corrosion rates would also account for the lateral protrusions and voids observed in cross-sections of the etched Al. (Fig. 4.20) These features should also serve as excellent anchoring sites should suspension particles fill those locations.

4.5 Conclusions

The Al foam surface was modified via three separate methods yielding three distinct surface morphologies. Zeolite and anodic oxide coatings were successfully

deposited on Al foams and HCl was used to etch Al foams. Optimal processing conditions for the zeolite coating were found to be 70˚C for 15-30 min. Coatings processed at these conditions had 50 µm thick, highly porous structure situated at the Al surface, suitable for entrapping $CaSiO_3$ particles. Optimal processing conditions for the anodized coatings were found to be 1.5 A/dm^2 current density for 30 min. Anodic oxide coatings processed in these conditions provided cracks running parallel to the Al struts and smaller dimpling across the surface that may improve mechanical interlock with infiltrated $CaSiO_3$. Optimal HCl etch conditions were 4 M HCl at room temperature for 5 min. Mass removal left behind multi-scale pitting suitable for trapping clusters of $CaSiO_3$ particles. Each of the applied processes produced comparatively unique surface structure on the Al foam. These differences were expected to result in appreciable changes in the IPC mechanical behavior.

Table 4.1. Zeolite Coating Process Conditions

Sample		Solution	Temperature	Time	Mass			Coating
					Before	After	Δ	
#	Type	ml	˚C	h	g	g	%	
Zeo1	square	50	100 (oven)	8	3.19	3.10	-2.82	flaking, poorly adhered
Zeo2	square	50	200 (oven)	8	3.24	2.56	-20.83	flaking, poorly adhered
Zeo3	square	50	95 (oven)	2	3.36	3.38	0.67	rough, 2nd layer forming
Zeo4	square	50	95 (oven)	5	3.18	3.27	3.01	rough, 2nd layer formed
Zeo5	square	50	95 (oven)	0.5	3.17	3.18	0.32	patchy, rough
Zeo6	square	50	95 (oven)	1	3.39	3.41	0.68	rough, single layer
Zeo7	square	50	25 (ambient)	0.5	3.21	3.21	-0.02	no change
Zeo8	square	50	25 (ambient)	1	2.98	2.98	-0.01	no change
Zeo9	square	50	70 (bath)	1	3.33	3.35	0.64	rough, single layer
Zeo10	square	50	70 (bath)	0.5	3.27	3.29	0.67	rough, near complete single layer
Zeo11	foam	250	70 (bath)	1	19.45	21.75	11.82	complete, cracks
Zeo12	foam	250	70 (bath)	0.5	19.87	20.46	2.94	complete, cracks
Zeo13	foam	250	70 (bath)	0.5	19.28	20.34	5.50	complete, cracks

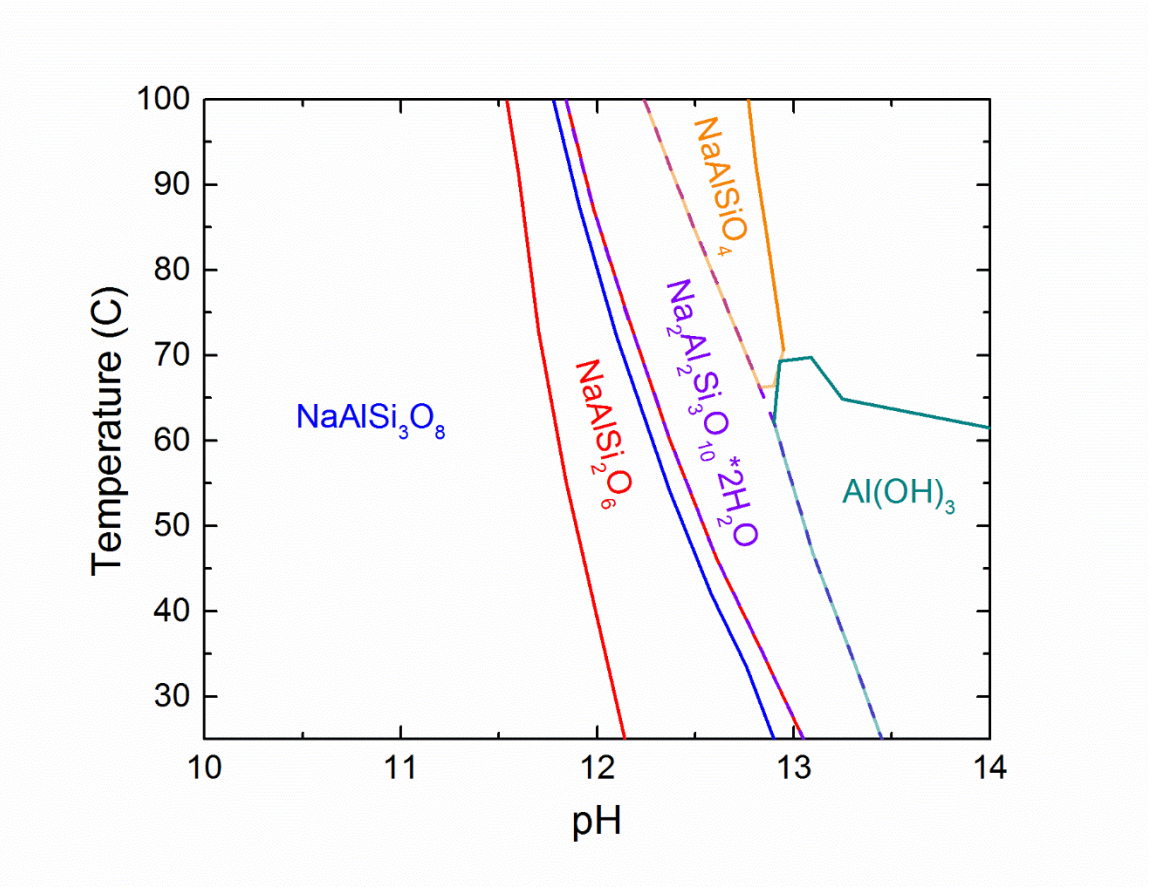

Figure 4.1. OLI thermodynamic chemical diagram predicting precipitated solids at 1 atm.

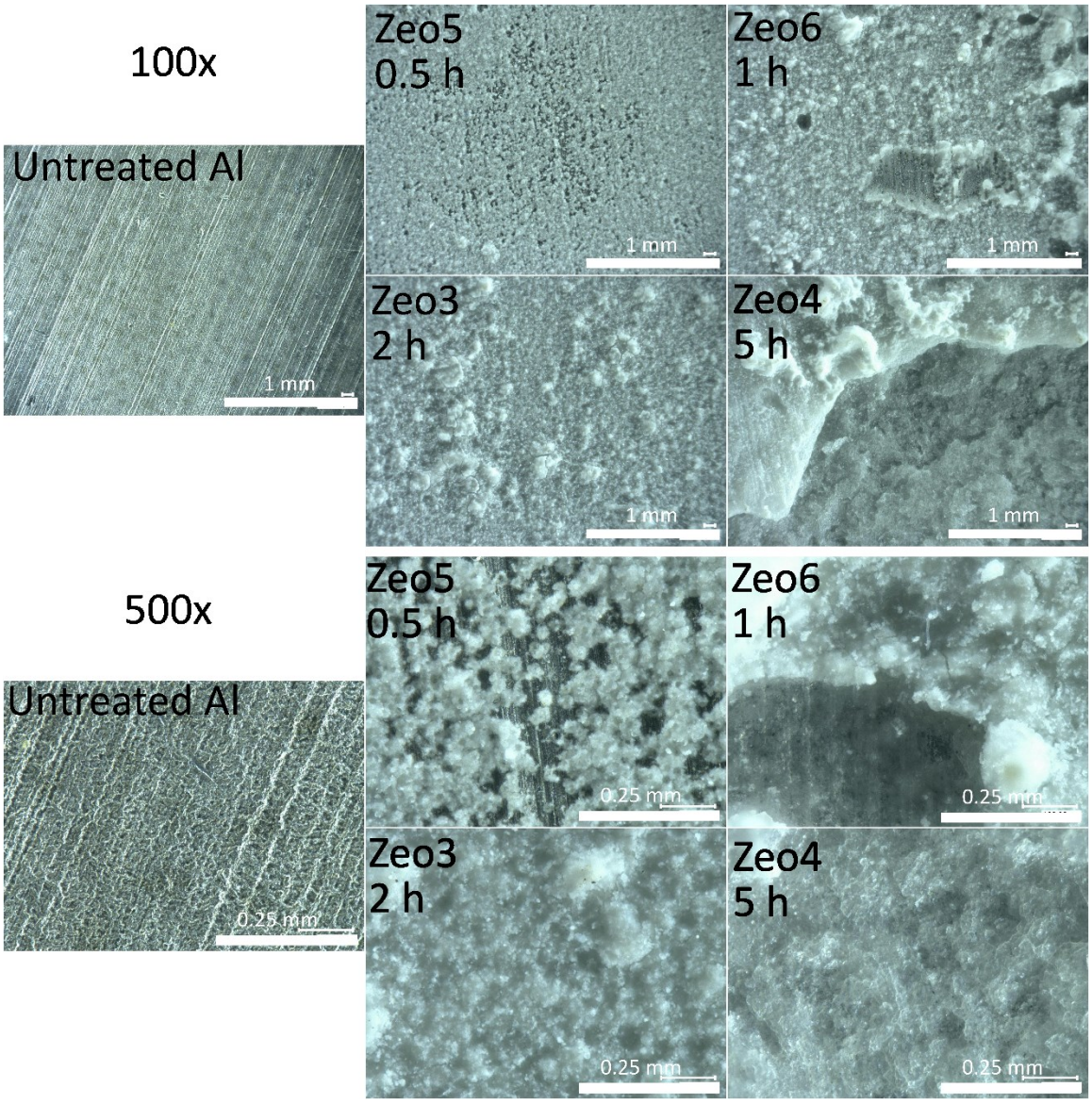

Figure 4.2. Effect of reaction time on zeolite coating at 95˚C.

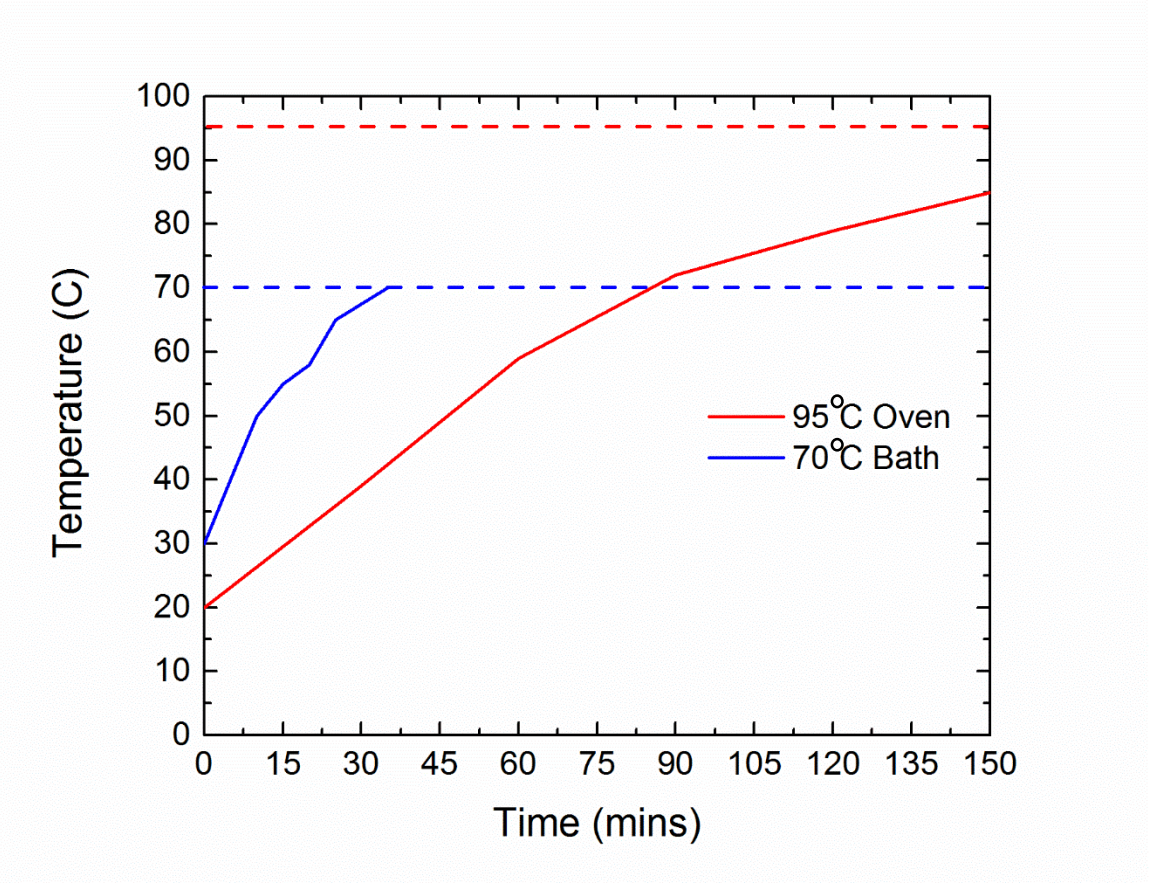

Figure 4.3 Heating profile for reaction containers in 95˚C oven and 70˚C water bath.

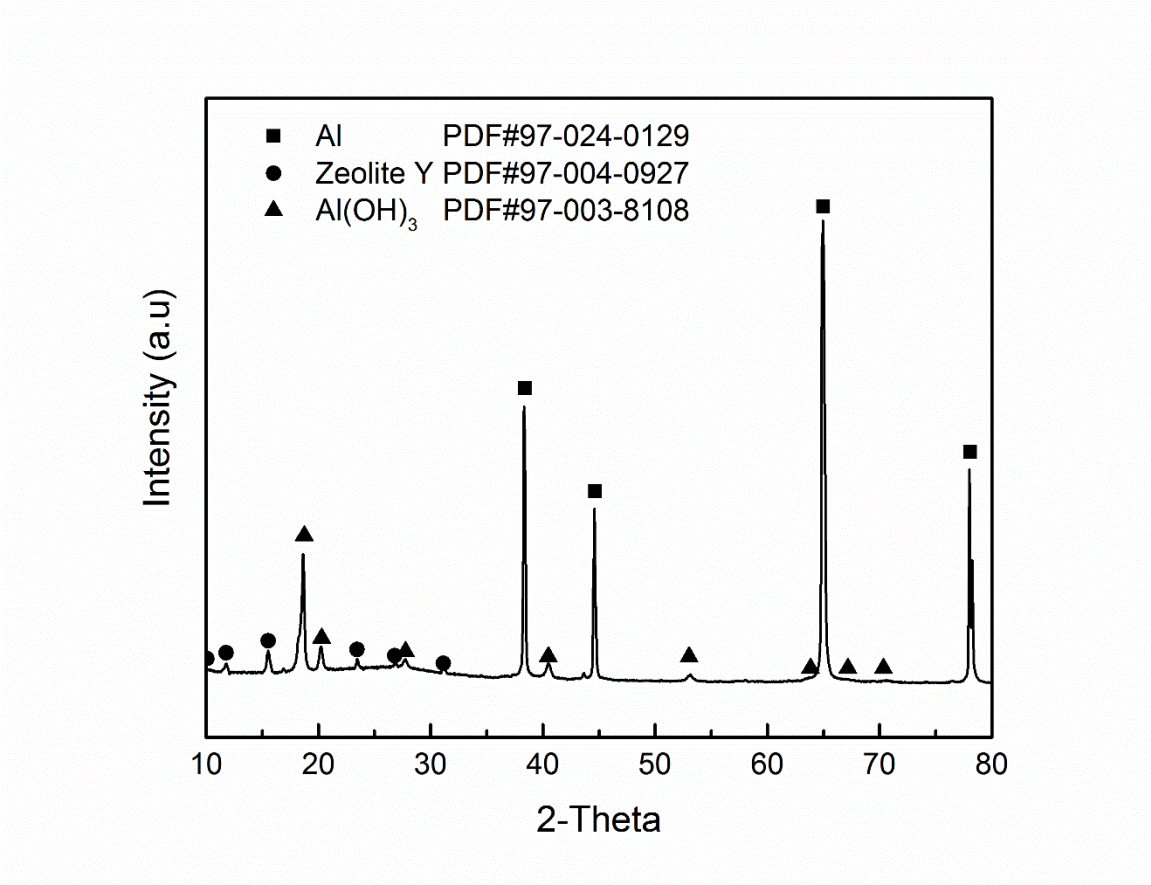

Figure 4.4. XRD pattern for Zeo4.

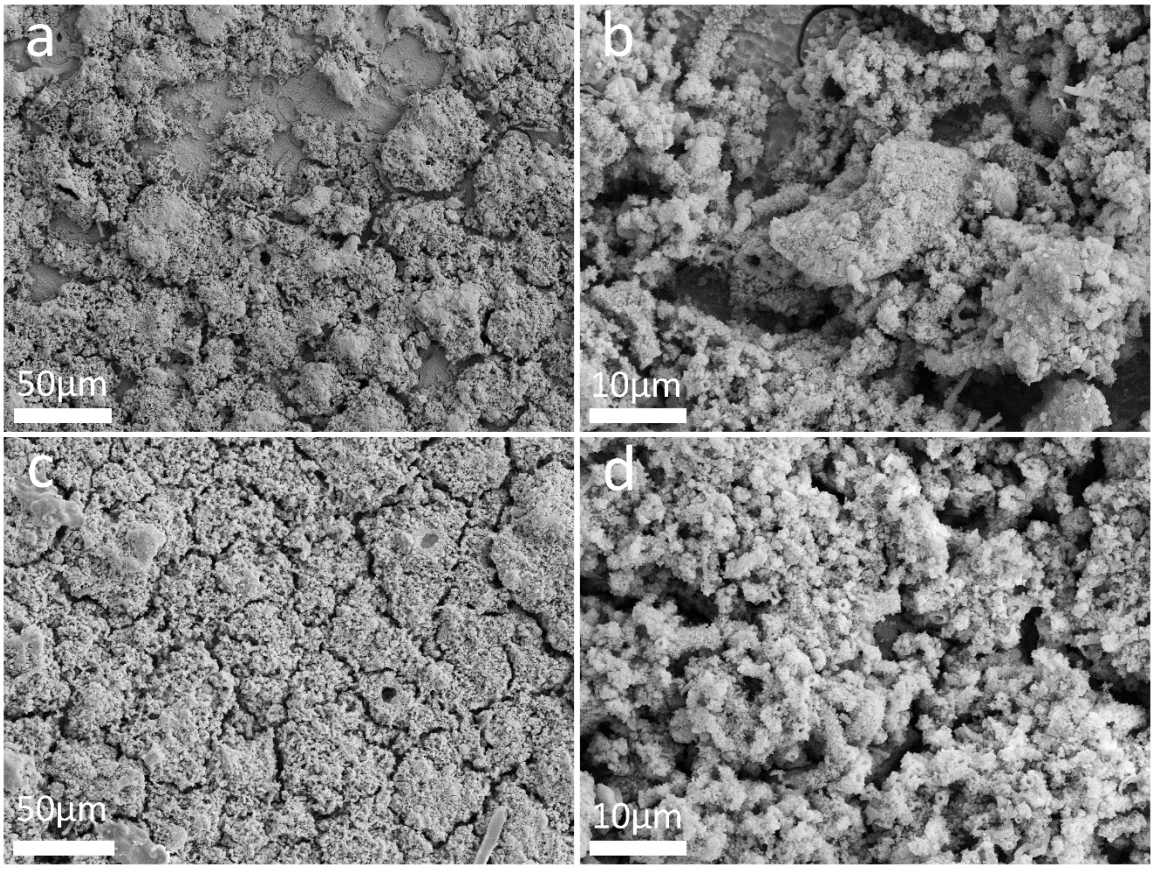

Figure 4.5. Comparison of 0.5 h reaction in 95˚C oven, a and b, and in 70˚C water bath, c and d.

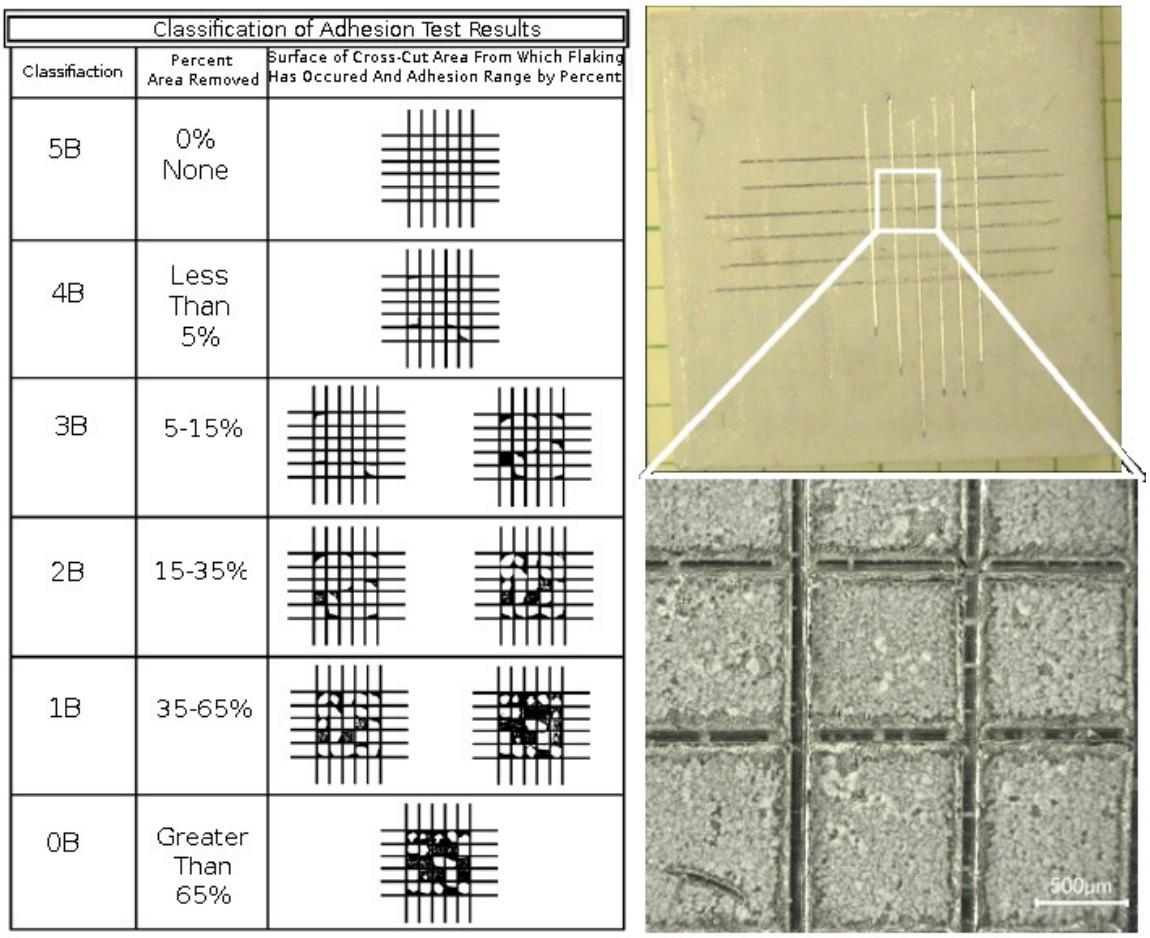

Figure 4.6. Tape peel test of 0.5 h @ 70˚C Zeo 10 sample. Slight removal of coating along edges yielded a 3B, 5-15% removed rating.

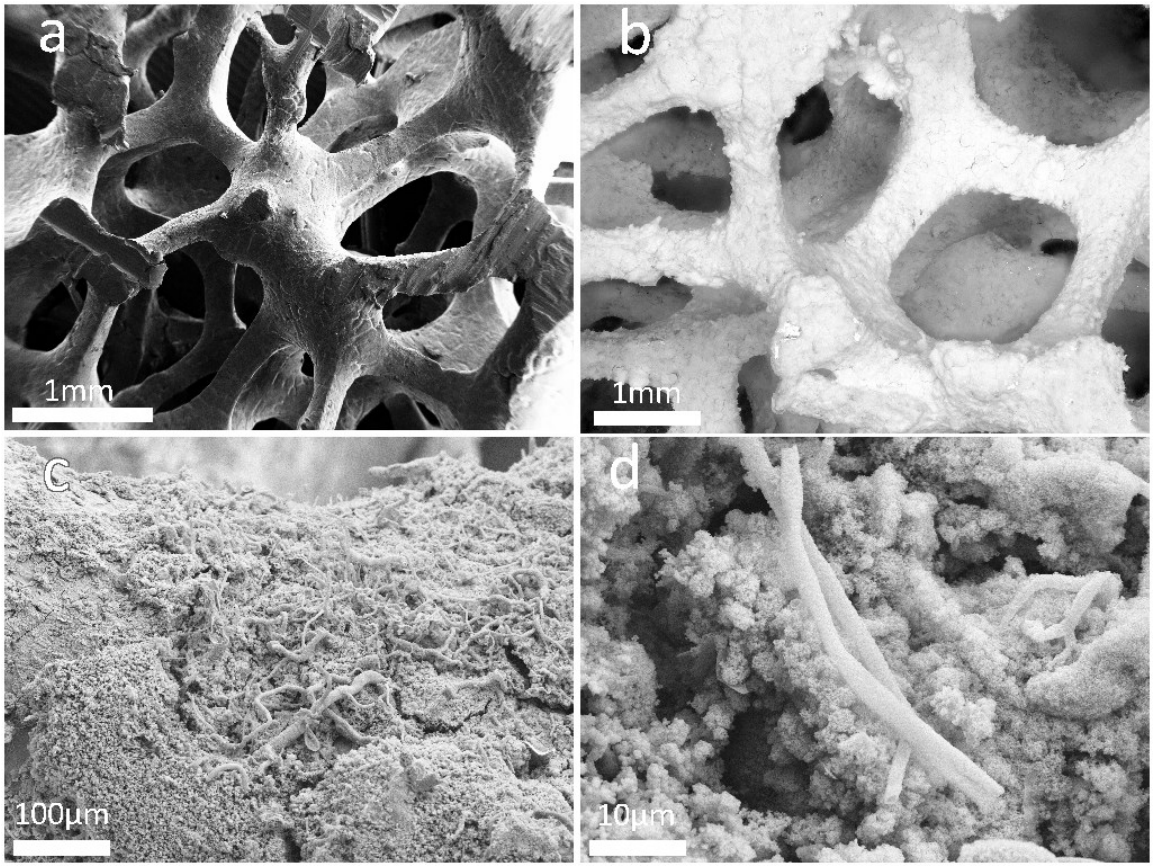

Figure 4.7. Zeolite coating on Al foam. a, un-coated, b, coated, c, coated Al strut surface, and d, high magnification of coated Al strut.

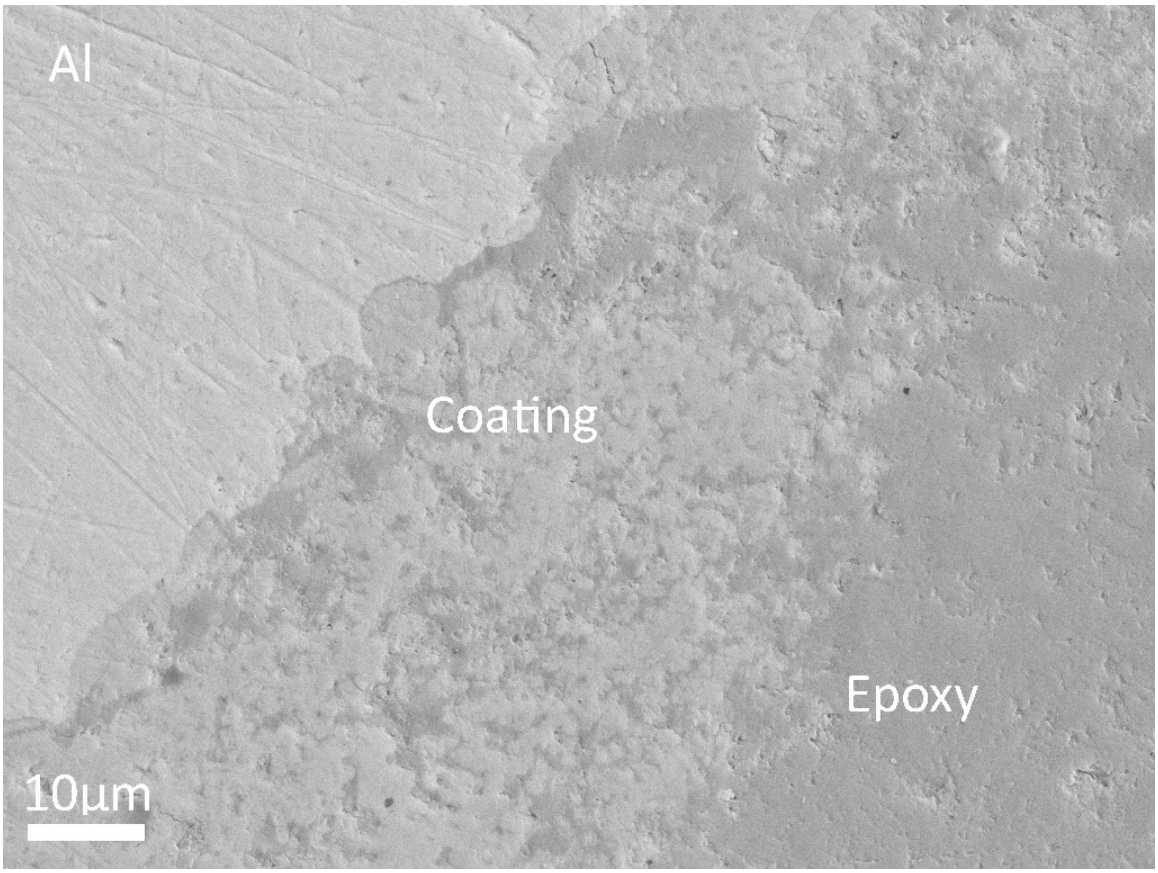

Figure 4.8 Polished cross-section of Zeo13.

Table 4.2. Anodizing Process Conditions

Sample #	Current Density A/dm^2	Current A	Time min	Mass before g	Mass after g	Δ %
An1	1.2	0.116	5	3.095	3.094	-0.032
An2	1.2	0.116	15	3.267	3.268	0.031
An3	1.2	0.116	30	3.358	3.360	0.060
An4	1.5	0.145	5	3.272	3.273	0.031
An5	1.5	0.145	15	3.254	3.257	0.092
An6	1.5	0.145	30	3.486	3.492	0.172
An7	1.8	0.174	5	2.731	2.732	0.037
An8	1.8	0.174	15	3.126	3.127	0.032
An9	1.8	0.174	30	3.197	3.198	0.031
An10	1.2	0.116	60	3.008	3.010	0.066
An11	1.5	0.145	60	3.287	3.300	0.389
An12	1.8	0.174	60	3.101	3.101	0.000

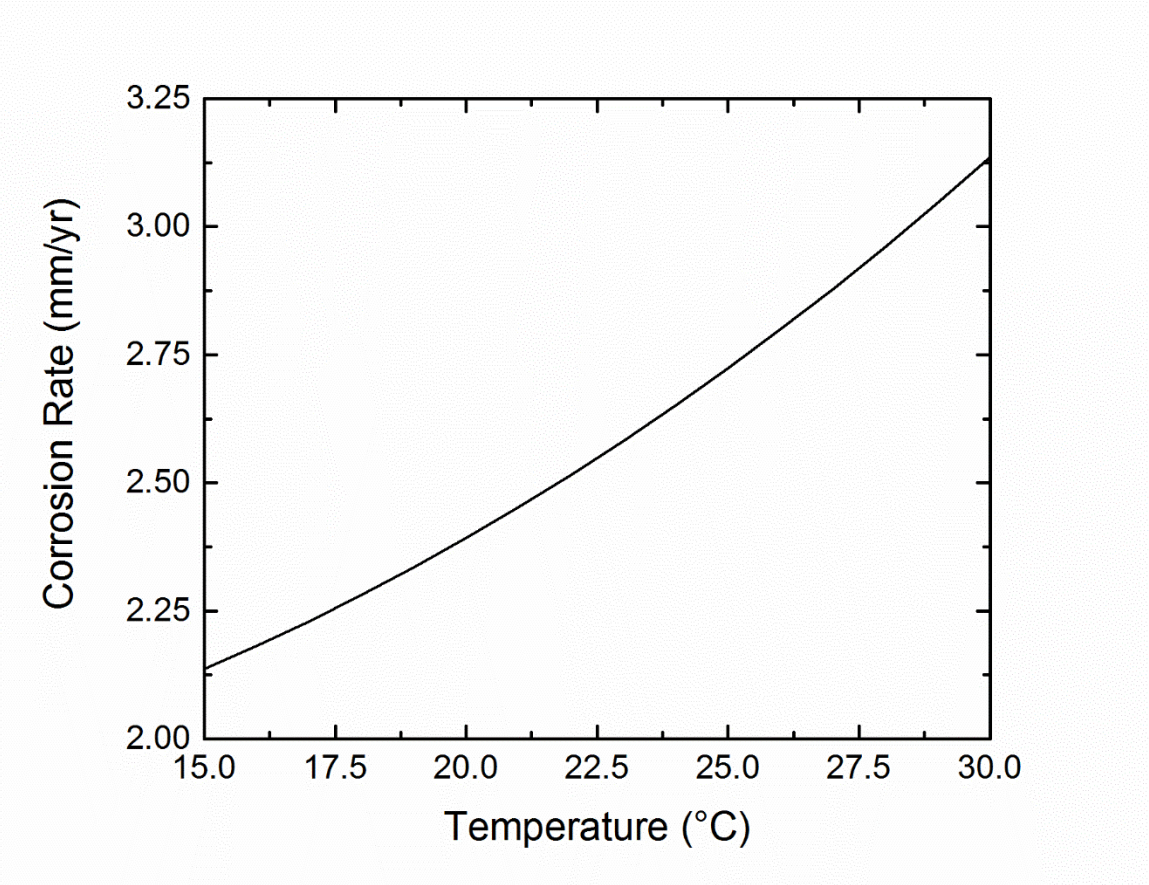

Figure 4.9. Simulated corrosion rate of Al in H2SO4.

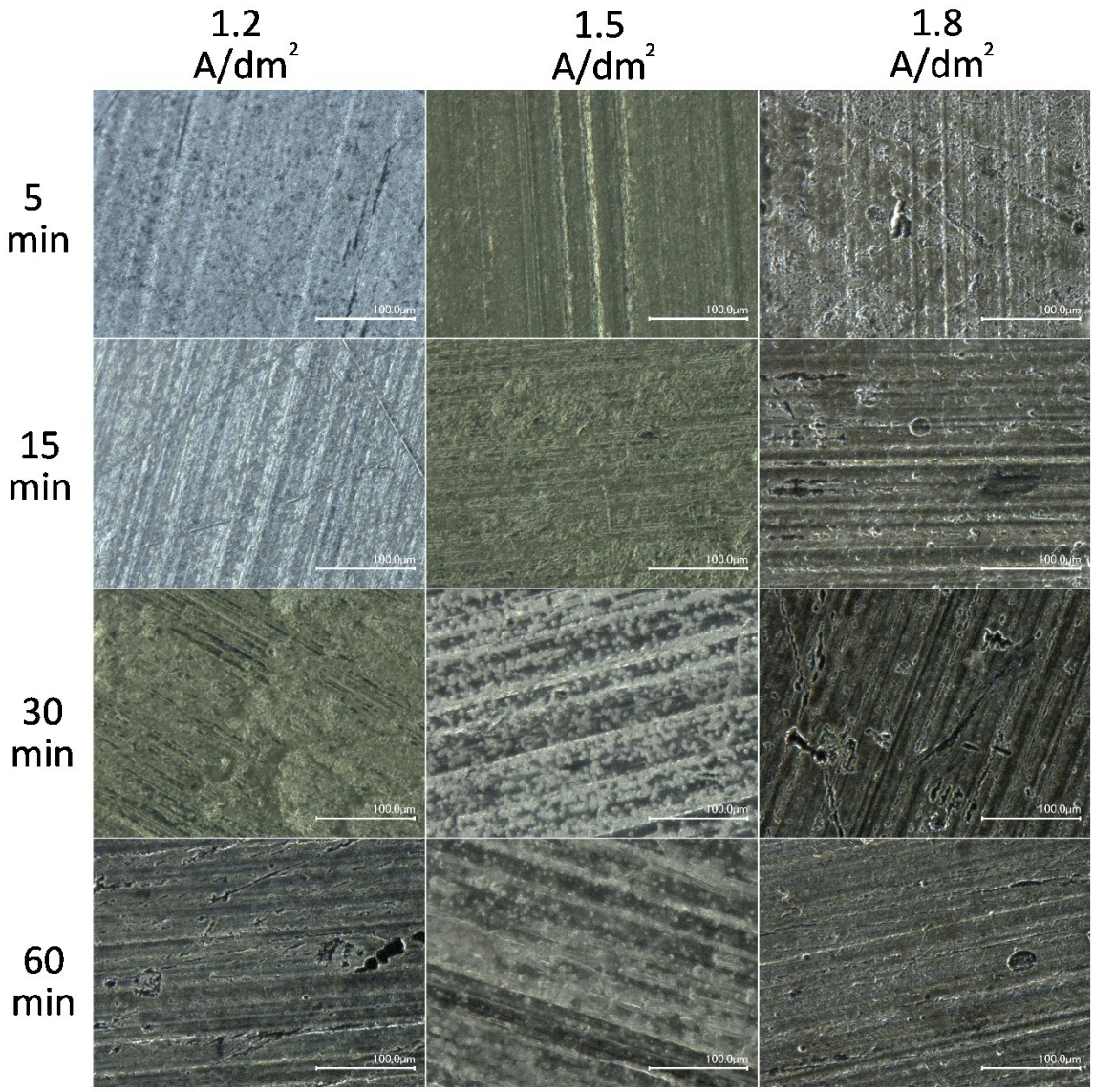

Figure 4.10. Optical images at 1000x magnification of anodized Al squares.

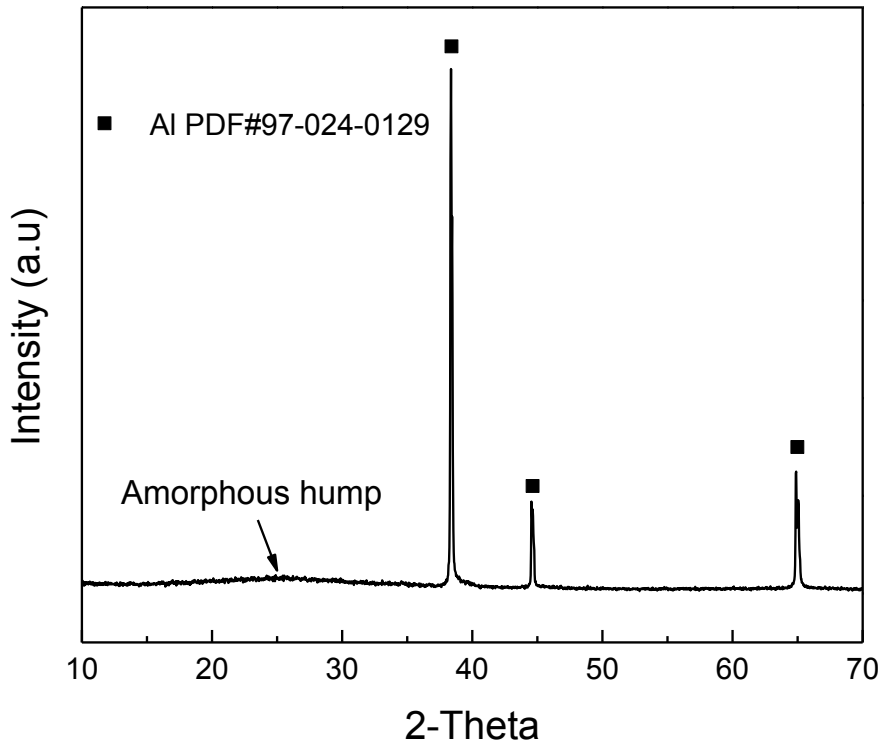

Figure 4.11. XRD pattern of An11.

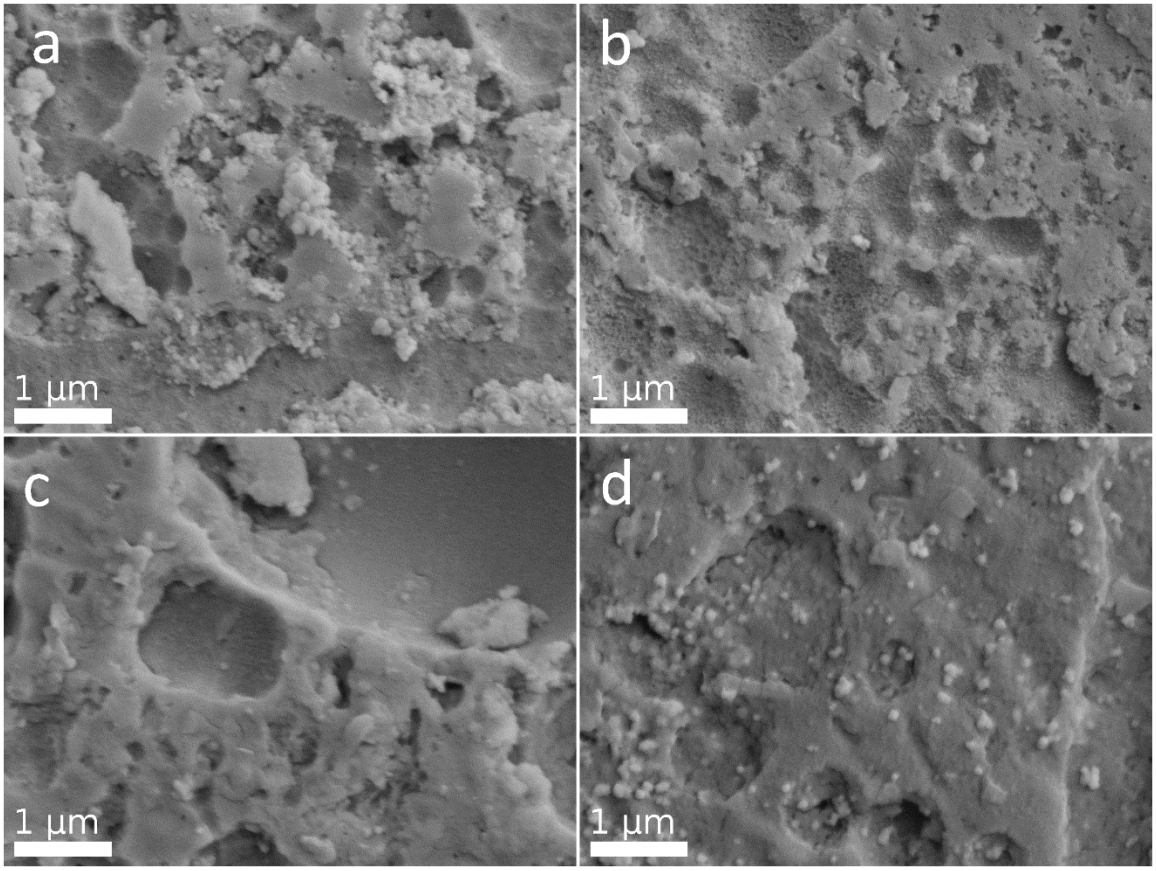

Figure 4.12. SEM comparison of Al squares anodized at 1.5 A/dm^2 applied current density for 5, 15, 30, and 60 min.

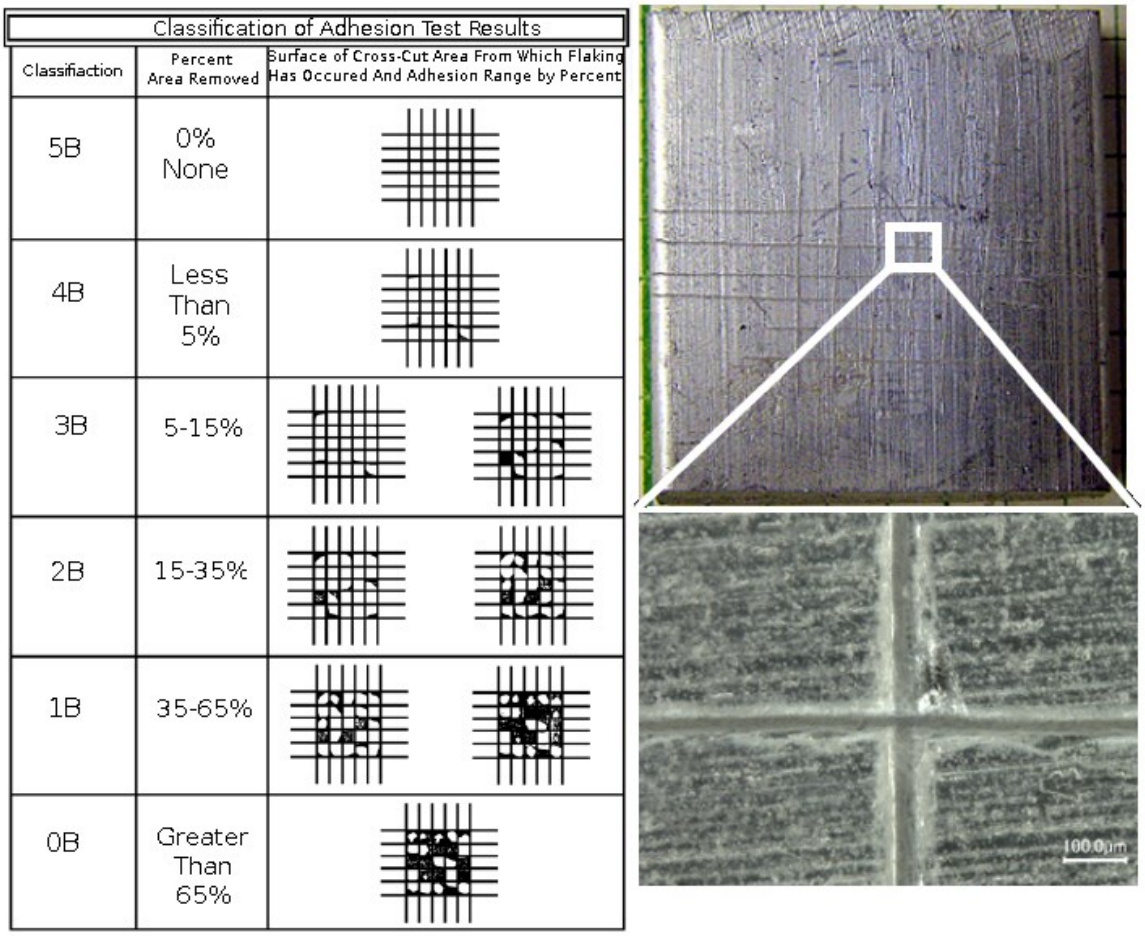

Classification of Adhesion Test Results		
Classifiaction	Percent Area Removed	Surface of Cross-Cut Area From Which Flaking Has Occured And Adhesion Range by Percent
5B	0% None	
4B	Less Than 5%	
3B	5-15%	
2B	15-35%	
1B	35-65%	
0B	Greater Than 65%	

Figure 4.13. Tape peel test of Al square anodized at 1.5 A/dm^2 for 60 min (An11).

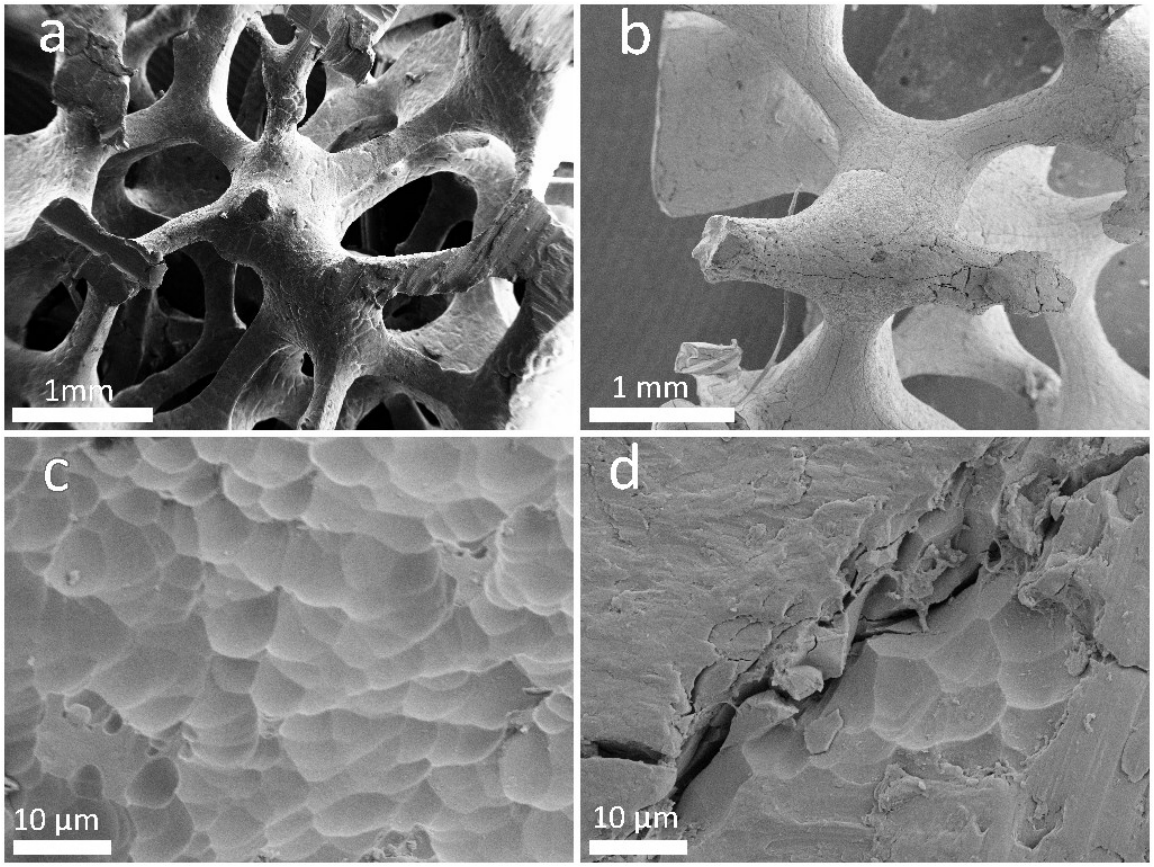

Figure 4.14. Anodic oxide coating on Al foam. a, un-coated, b, coated, c, coated Al strut surface, and d, crack in coating along Al strut.

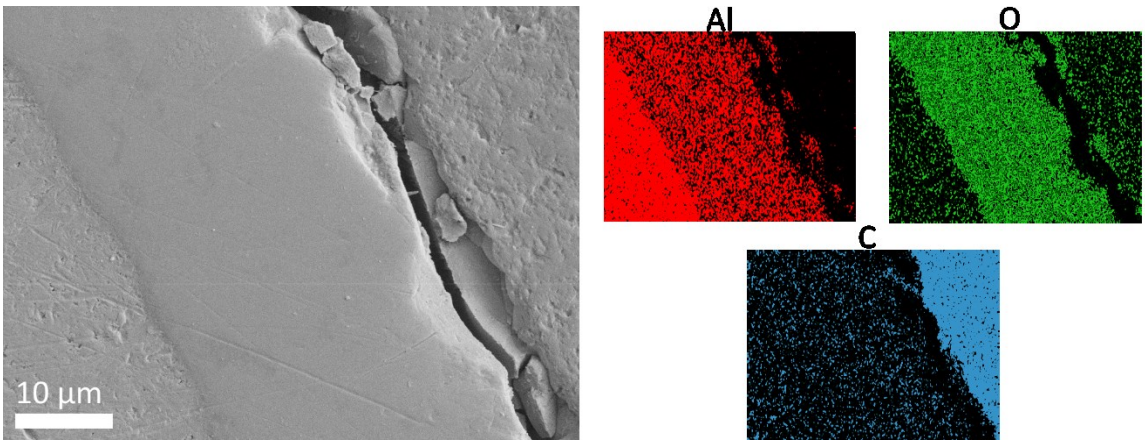

Figure 4.15. Polished cross-section of anodized Al foam at 1.5 A/dm^2 for 60 min.

Table 4.3 4 M HCl Etch of Al Squares

Sample	Time	Mass			Mass Loss per Area
		Before	After	Δ	
	min	g	g	%	g/m^2
Etch 1	1	3.399	3.398	-0.02942	0.923
Etch 2	2	3.346	3.345	-0.02989	0.932
Etch 3	3	3.385	3.383	-0.05908	1.86
Etch 4	4	3.668	3.664	-0.10905	3.467
Etch 5	5	3.244	3.237	-0.21578	6.75

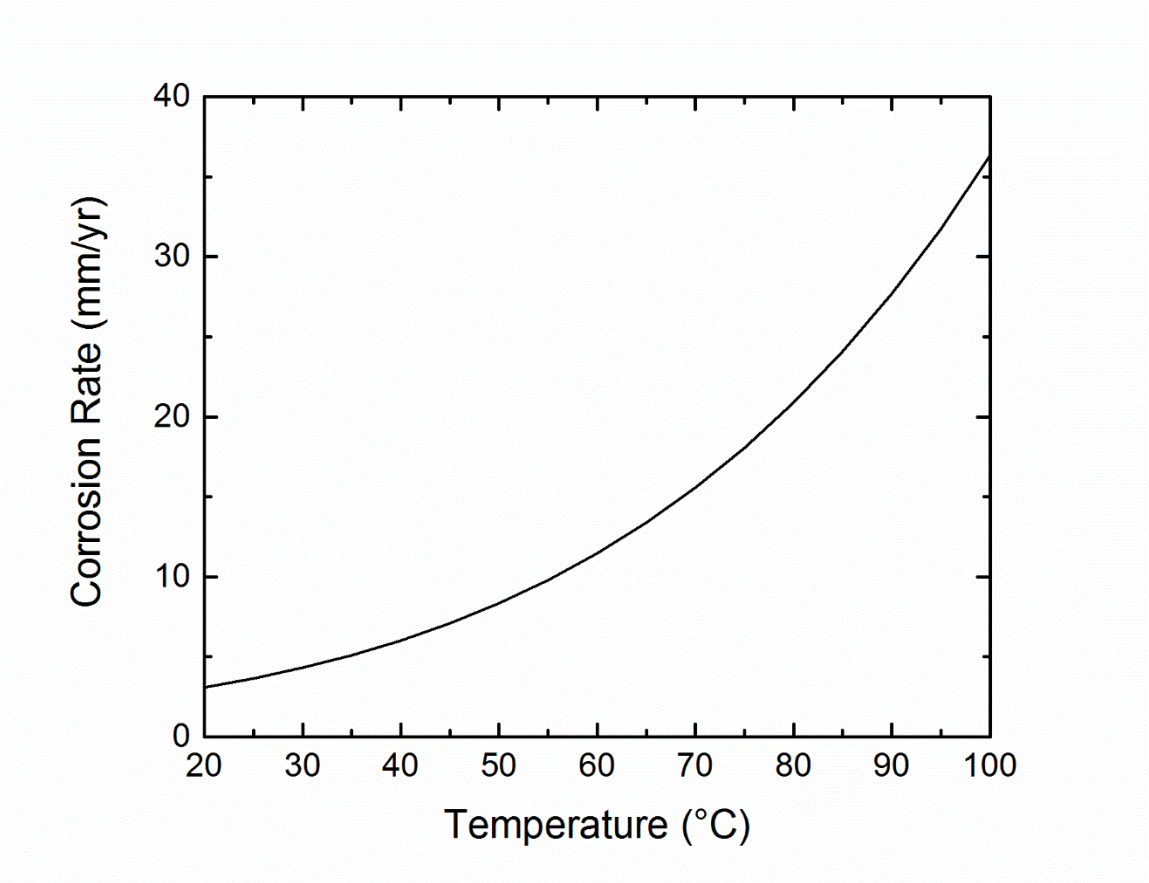

Figure 4.16. Simulated corrosion rate of Al in 4 M HCl.

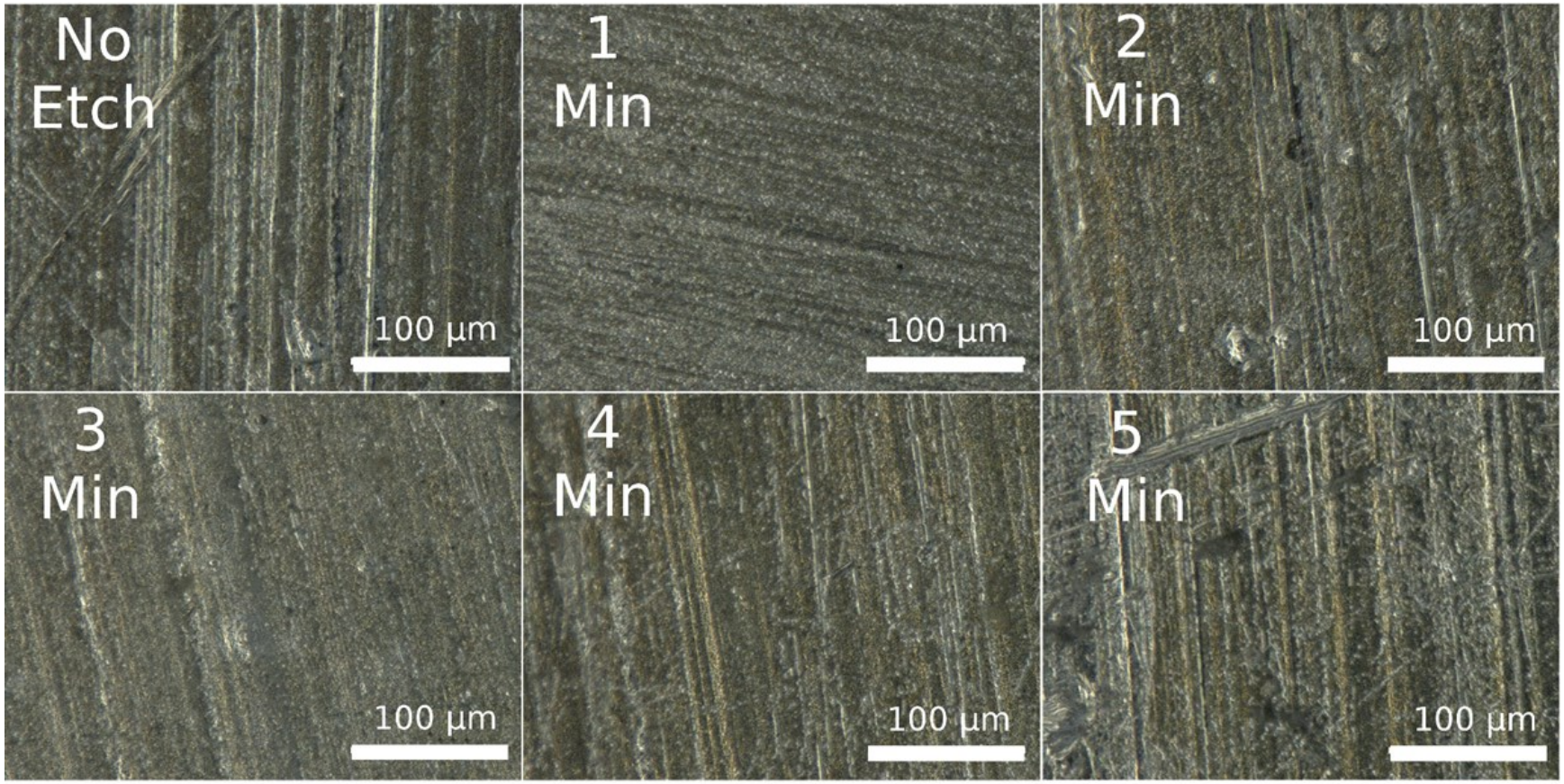

Figure 4.17. Optical images of 4 M HCl etched Al squares.

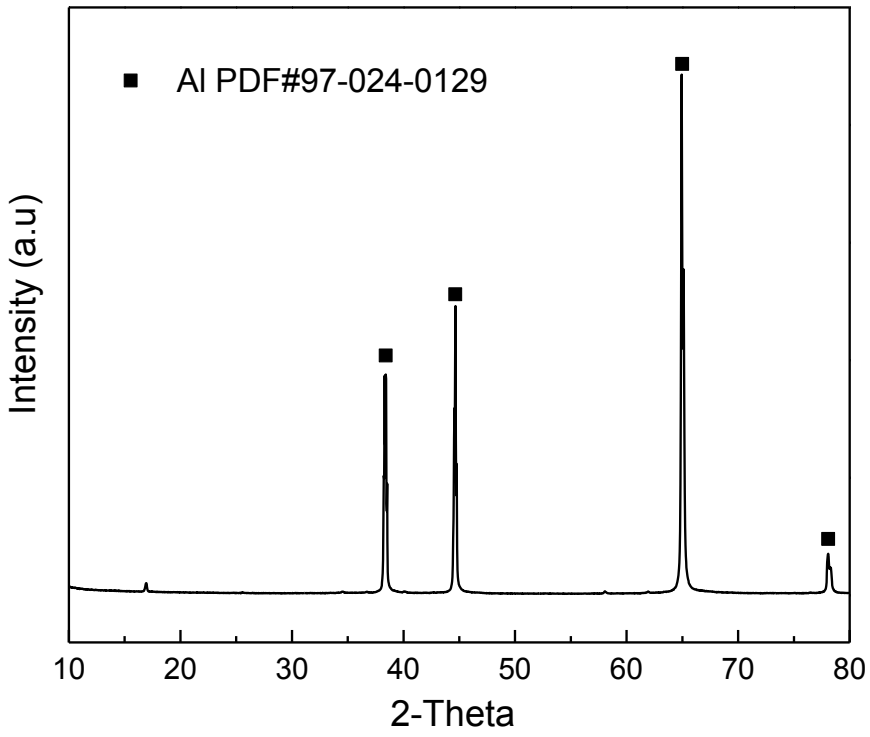

Figure 4.18. XRD pattern of Etch 5.

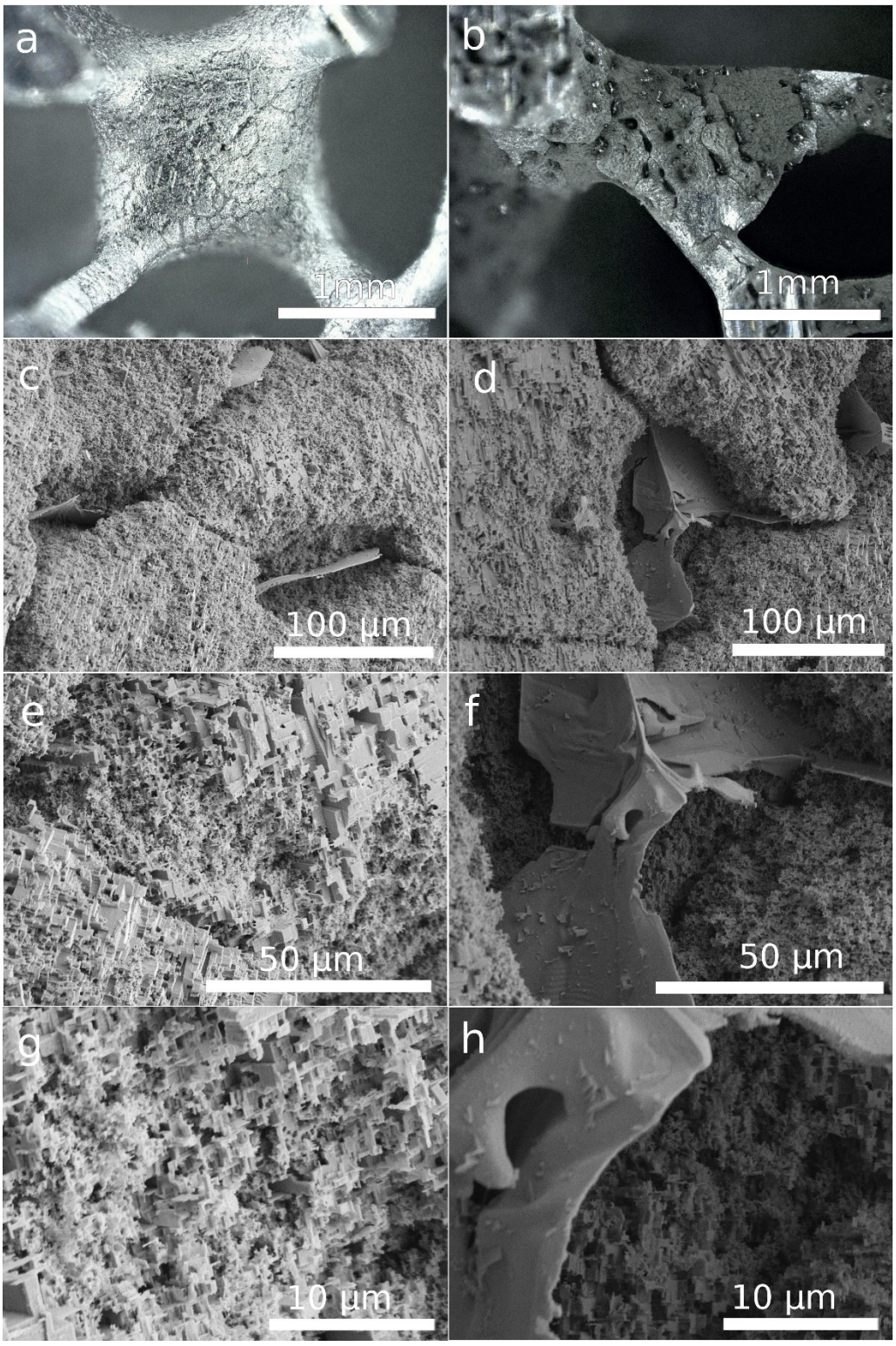

Figure 4.19. Comparison of unetched Al foam (a), with etched Al foam. Increasing magnification of area between large pit (c,e,g) and at large pit (d,f,h).

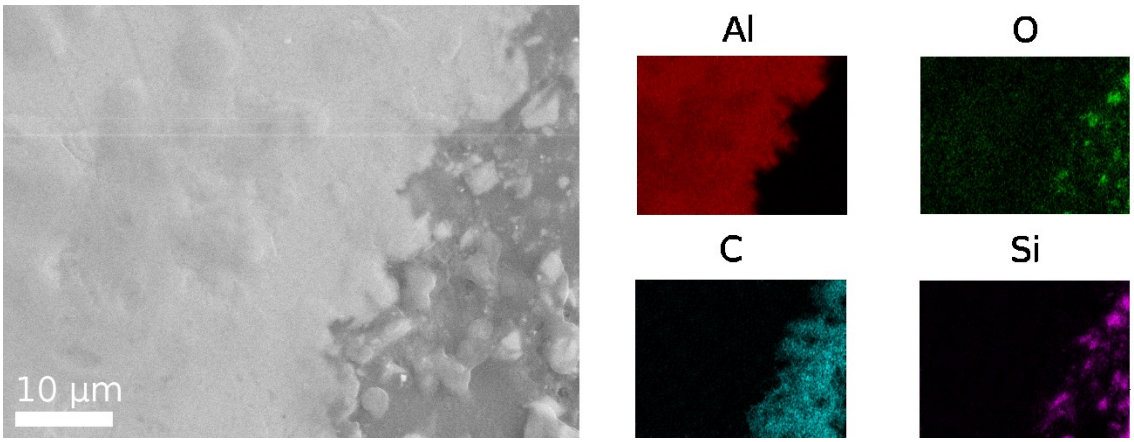

Figure. 4.20. Polished cross-section of etched Al foam with EDS showing a rough Al surface.

5. Treated Al-Carbonated $CaSiO_3$ IPC Mechanical Properties

5.1 Introduction

Al IPCs formed via an infiltration route have a range of mechanical properties dependent on composition. As previously shown, the compressive strength vs density property space for Al IPCs has an open region between polymer infiltrated Al scaffolds and Al infiltrated ceramic scaffolds. [30, 80–85] Results from Al-carbonated $CaSiO_3$ IPCs tested in chapter 3 were shown to fit within this open region, thus demonstrating the viability of the infiltration and g-rHLPD process. Interaction between the ceramic and metal components of the IPC was found to be mechanical, likely mediated by the Al surface structure. This observation suggested that manipulation of the Al surface might change the interface interaction, thereby affecting the bulk properties of the composite.

Surface modification was achieved via treatment of the Al surface as detailed in chapter 4. Two coatings were selected, a zeolite coating and an anodic oxide coating. The zeolite coating was thick, ~50 µm, and highly porous with a range of opening sizes, ~1-10 µm, potentially serving as location for suspension particle entrapment. The anodic oxide coating was thinner, ~30 µm, with periodic dimpling, but no evident porosity. Thus the anodic coating was a comparably small change to the Al surface compared to that of the zeolite coating. HCl acid etching of the Al foams removed material to provide an increase in surface roughness. Two scales of surface structure

were created, large 200 µm pits and fine 1 µm terrace-step-ledge spacing. These starkly different surface morphologies on the Al foam are expected to create differences in the bulk mechanical response of the Al-carbonated $CaSiO_3$ IPC.

The objective of this chapter is to evaluate whether or not a change in mechanical bulk properties of the Al-carbonated $CaSiO_3$ composite can be induced by modification of the Al surface topology. Compressive testing will be used to determine any change in mechanical response. The cause or lack thereof of any effect will be scrutinized via observation of the fracture interface, along with cross-section of the treated Al-carbonated $CaSiO_3$ IPC. Conclusions will be drawn on the ability of the treatments to change the IPC's mechanical properties and how the IPC's place in Al infiltrated IPC property space might be altered.

5.2 Experimental

Experimental Strategy

10 PPI Al foams will be treated with the three surface modification processes detailed in Chapter 4: zeolite coating, anodizing, and HCl etching. $CaSiO_3$ will be infiltrated into the foams and carbonated in accordance with the procedure in Chapter 2 and 3 to produce treated Al-carbonated $CaSiO_3$ IPCs. Green density and extent of carbonation of the infiltrated $CaSiO_3$ will be monitored to assess any effect of the modified Al surface. Mechanical properties of the untreated, zeolite coated, anodized, and HCl etched Al foams will be collected and compared. Mechanical properties of the untreated Al-carbonated $CaSiO_3$, zeolite coated Al-carbonate $CaSiO_3$, anodized Al-

carbonate $CaSiO_3$, and HCl etched Al-carbonated $CaSiO_3$ IPCs will be collected and compared. Any significant difference in the mechanical response of the various composites will be assessed. Polished cross-sections and fracture surfaces of each sample type will be observed to understand the microstructure of the interface. Damage and cracking will be noted, and inferences will be drawn about how the modified Al surfaces affect the interface failure behavior.

Sample preparation

Al foams were coated with zeolite and anodic oxide and etched with HCl as detailed in Chapter 4. The treated foams were infiltrated and carbonated via the procedures in Chapter 2 and 3. An extra step was necessary for infiltration of the zeolite coated Al foams. The coating was found to be hydrophilic, and held a substantial amount of water. TGA measurements (TA Q5000 TGA, TA Instruments, New Castle, DE) on a water saturated zeolite coated foam piece were performed to understand the amount of water the coating can take in. (Fig. 5.1) Temperature was held at ambient for 120 min, then ramped to 100˚C and held for 120 min, then ramped to 250˚C and held for 120 min, and finally ramped to 400˚C and held for 120 min. 20 ml/min of nitrogen was passed through the sample chamber during the entire test. The prominent mass loss during the initial ambient temperature hold amounted to 3.59 mg. This value divided by the final mass of the coated Al, 25.71 mg, indicated a water absorption of about 14% g H_2O/g coated Al. A dried zeolite coated Al foam would pull water from the infiltrating suspension, likely inhibiting total infiltration. Thus, the zeolite coated foams were first pre-wet with water to avoid dehydration of the $CaSiO_3$ suspension. The

resulting cube samples were cut with a precision cutter (PICO 155 precision cutter, PACE Technologies, Tucson, AZ) into quarters and the top face was cut parallel when necessary. Three of the four quarters were used for destructive testing. Portions of the destroyed samples were kept to observe the fracture surface. The remaining quarter was sectioned to observe the interior structure.

Samples were prepared for imaging and chemical analysis via polishing. Representative pieces of samples were first cut to small size using the precision cutter. After drying, the samples were placed in 1" diameter cylindrical molds and infiltrated with mounting epoxy (EpoThin 2 Epoxy System, Buehler, Lake Bluff, IL). Vacuum was then pulled on the freshly poured epoxy/sample containing molds using a Cast N' Vac 1000 Vacuum Impregnation System (Buehler, Lake Bluff, IL) for ~5 min, then left in ambient conditions for 24 h to harden. The hardened epoxy mounted samples were then ground and polished on an EcoMet 250 Grinder-Polisher (Buehler, Lake Bluff, IL). The typical polishing schedule used was as follows: 1) 320 grit SiC paper, 30 1/s head speed, 240 1/s base speed, complementary head/base direction, 5 min. 2) 6 µm polycrystalline diamond suspension (DIAMAT, Pace Technologies, Tucson, AZ) on Tri-Dent cloth (Buehler, Lake Bluff, IL), 30 1/s head speed, 150 1/s base speed, complementary head/base direction, 6 min. 3) 3 µm polycrystalline diamond suspension (DIAMAT, Pace Technologies, Tucson, AZ) on Tri-Dent cloth, 30 1/s head speed, 150 1/s base speed, complementary head/base direction, 4 min. 4) 0.05 µm polycrystalline diamond suspension (DIAMAT, Pace Technologies, Tucson, AZ) on Micro-Cloth (Buehler,

Lake Bluff, IL), 30 1/s head speed, 150 1/s base speed, contra head/base direction, 2 min. After polishing, the epoxy was cut away from the samples

Green Density and Carbonation

Density was calculated simple by dividing sample mass by volume. Mass of samples was measured via scales. Volume was calculated from caliper measurements of sample dimensions. The procedure for calculating the green density of $CaSiO_3$ within the pores of the Al foam was as follows: First, the mass of $CaSiO_3$ in the composite was determined by subtracting the mass of the foam from the mass of the composite. Then the volume of the foam was calculated by multiplying the foam mass by the theoretical density of Al, 2.7 g/cm^3. Next, the $CaSiO_3$ volume was found by subtracting the foam volume from the caliper measured bulk volume. Finally, the $CaSiO_3$ mass was divided by the $CaSiO_3$ volume to yield the green density within the Al pores.

Mass gain of each sample type, untreated, zeolite coated, anodized, and HCl etched, was recorded after carbonation. This quantity was solely attributed to the uptake of CO_2 during carbonation reaction, as shown in Eqn. 5.1

$$CaSiO_3(s) + CO_2(g) \rightarrow CaCO_3(s) + SiO_2(s) \quad \text{(Eqn. 5.1)}$$

Thus the percent of $CaSiO_3$ carbonated was determined by Eqn. 5.2.

$$Rxn.Completion = \left(1 - \frac{\frac{m_i}{M_{CaSiO_3}} - \frac{\Delta m}{M_{CO_2}}}{\frac{m_i}{M_{CaSiO_3}}}\right) \times 100 \quad \text{(Eqn. 5.2)}$$

$$m_i = initial\ CaSiO_3$$

$$\Delta m = mass\ gain$$

$$M_{CaSiO_3} = molecualr\ mass\ of\ CaSiO_3$$

$$M_{CO_2} = molecular\ mass\ of\ CO_2$$

Mechanical Testing

Samples were tested in compression on a 100 kN capacity load frame (Instron, MA) at 2 mm/min. The test run end condition was set to a lower threshold of 0.5 kN. Due to slight differences in sample pre-loading, all strain values were normalized to ensure that the stress vs. strain plots were comparable. The elastic modulus for each sample was determined by selecting a linear portion of its the stress vs strain plot, applying a linear fit, and taking the resulting slope as the elastic modulus. In all cases the adjusted R-square of the fit was greater than 0.995.

Interface and Fracture Surface Observation

Sample microstructure at fracture surfaces and polished sections were observed using a VHX-1000 digital microscope (Keyence, NJ) and a field emission scanning electron microscopy (FESEM) (Zeiss Sigma FESEM, Carl Zeiss, Oberkochen, Germany). Sample surfaces were sputter coated with 10 nm thick gold coatings (Electron Microscopy Sciences, model# EMS 150T ES, PA) using a sputtering current of 20 mA for 5 min. Energy dispersive spectroscopy (EDS) was also used to ascertain chemical composition of the observed surfaces. In the case of polishing fracture surfaces, vacuum epoxy infiltration was used to reinforce the cracked/damaged structure.

5.3 Results

Treatment, Infiltration, and Carbonation

The mass of each foam was compared before and after each treatment to affirm that the desired surface modification had occurred. Both the zeolite coated and anodized Al foams increased in mass by 0.315 and 0.305 g respectively. The etched Al foam lost 1.946 g during treatment. These small changes in mass indicated little change to the overall pore structure of the foams. Thus, overall infiltration was not expected to vary between sample types.

Green density of the infiltrated $CaSiO_3$ suspensions was measured to ensure the starting structure of each sample was relatively comparable. (Fig. 5.2) No significant variation amongst the untreated, zeolite, anodized, and etched sample types was observed with values of 1.87, 1.88, 1.88, and 1.86 g/cm^3 respectively. Consistent green density across all samples suggested a comparable amount of porosity and internal voids within each sample.

Carbonation of the infiltrated $CaSiO_3$ was also monitored to assess any effect of the Al surface treatments. (Fig. 5.3) The untreated and zeolite samples had similar reaction completions, 46.1 and 44.6 % respectively. The anodized and etched samples exceeded the untreated and zeolite sample carbonation at 51.8% and 50.2 % reaction completion respectively. The difference in reaction completion was attributed to variability in the carbonation reactors, such as heat and gas gradients and pore

saturation by water. A slight increase in compression strength was expected for the higher reaction completions.

Mechanical Testing

Compression tests of untreated Al foam showed typical foam deformation behavior. (Fig. 5.4) An initial, brief elastic period led to an average local maximum strength of 2.32 MPa. A period of relatively constant stress was then held up to about 30% strain, corresponding to the collapsing of the foam cells. At increasing strain, stress again increases as the collapsed foam begins to densify. Zeolite coated Al foam showed very similar behavior to the untreated foam. (Fig. 5.5) After the elastic region, an average initial maximum stress of 2.39 MPa was recorded. Constant stress was then held up to about 25% strain, after which stress increased. Anodized Al foam deviated from the untreated foam behavior. (Fig. 5.6) The elastic region and initial average local maximum of 2.26 MPa were similar to the untreated foam, but a dissimilar loss of stress resisted immediately following the initial max was observed. Subsequent peaks and losses of stress continued out to about 45% strain. After 45% strain the increasing stress due to densification became apparent. The etched Al foam was weaker over the tested strain compared to the other samples. (Fig. 5.7) The initial average maximum was only 1.65 MPa. The constant stress region was comparatively extended as well, reaching to about 45% strain before signs of densification began.

Compression tests of an infiltrated, untreated Al foam was provided for comparison with the treated foams. (Fig. 5.8) An elastic region extended to an average

of 2.54% strain prior to ultimate strength. After initial failure a rapid decrease in stress occurred. After a minimum stress, the remaining sample structure resisted about 25-50 MPa of stress as it progressively failed at increasing strain. The zeolite coated Al foam – carbonated $CaSiO_3$ IPC samples had very similar compression behavior as the untreated samples. (Fig. 5.9) The elastic region reached up to an average of 2.57% strain. Ultimate strength was followed by a quick loss in stress. After a minimum stress in the 10-15% strain region, stress resisted was in the 20-50 MPa range as the residual structure continued to be destroyed. Note that one of the test runs was interrupted pre-maturely due to an error with the test system and thus was not recorded to higher strain. The anodized Al foam – carbonated $CaSiO_3$ IPC samples had similar behavior compared to the untreated samples. (Fig. 5.10) The elastic region persisted further than the other samples at an average of 2.84% strain. The typical sharp drop in stress following ultimate strength was also observed. Residual strength was in the 15-30 MPa range through the extended strain region. The HCl etched Al – carbonated $CaSiO_3$ IPC behaved similarly to the untreated samples. (Fig. 5.11) The elastic region lasted up to an average strain of 2.53%. After peak stress, a sharp drop was observed with stress resisted in the 25-35 MPa range at extended strain.

Average ultimate strength of the Untreated, Zeolite coated, Anodized, and HCl Etched Al – carbonated $CaSiO_3$ IPCs was recorded. (Fig. 5.12) The untreated samples averaged 115.3 MPa with a 12.4 MPa standard deviation. The zeolite coated samples averaged 114.8 MPa with 8.2 MPa standard deviation. The anodize samples averaged 110.8 MPa with a 8.1 MPa standard deviation. The HCl etched samples averaged 106.7

MPa with a 13.7 MPa standard deviation. Average elastic modulus for each sample type was also calculated. (Fig. 5.13) Untreated samples averaged 52.0 GPa with a 5.7 GPa standard deviation. Zeoltie coated samples averaged 49.2 GPa with a 2.8 GPa standard deviation. Anodized samples averaged 43.9 GPa with a 6.7 GPa standard deviation. HCl etched samples averaged 47.2 GPa with a 12.2 GPa standard deviation.

Interface Characterization

Polished cross-sections of untreated Al – carbonated $CaSiO_3$ IPCs were imaged with optical microscopy and SEM to evaluate the metal-ceramic interface. (Fig. 5.14) Optical images showed mostly continuous contact along the interface between the ceramic and metal. (Fig. 5.14 a) The ceramic particles appeared to fill the slight surface roughness of the Al. SEM images indicated that the ceramic and metal were closely oriented, yet a clear delineation between them was also apparent. (Fig. 5.14 b) This region was filled with mounting epoxy, thus the separation might have been introduced during the mounting and polishing process. Polished cross-sections of zeolite coated Al – carbonated $CaSiO_3$ IPCs were imaged with optical microscopy and SEM, and elemental distribution was determined with EDS in order to understand the effect of the coating on interface interaction. (Fig. 5.15) Optical images revealed open voids in the zeolite coating. (Fig. 5.15 a) Closer inspection with SEM images showed some evidence of particle entrapment by the zeolite coating. (Fig. 5.15 b) EDS confirmed that some Ca and Si overlapping regions were inside the zeolite coating. A large amount of C was also observed within the zeolite region, indicative of mounting epoxy. This suggested that much of the porosity of the zeolite layer was not filled with the infiltrated $CaSiO_3$ but

remained open post processing. Polished cross-sections of anodized Al – carbonated $CaSiO_3$ IPCs were imaged with optical microscopy and SEM, and elemental distribution was determined with EDS in order to understand the effect of the coating on interface interaction. (Fig. 5.16) At lower magnification in optical images, the coating appeared continuous and uniform, with the carbonated $CaSiO_3$ flush against it. (Fig. 5.16 a) Occasional voids were noted along the anodized layer – carbonated $CaSiO_3$ interface, likely due to pull-out from polishing. SEM images of the interface showed regions of continuous Al – anodic layer – epoxy – carbonated $CaSiO_3$, occasionally interrupted by regions of fractured anodic layer. (Fig. 5.16 b) Corresponding EDS elemental maps supported this observation, with clearly defined Al and O overlap representing the anodic oxide layer, a band of C indicating the mounting epoxy, and Si and Ca being mostly excluded from those respective regions. The fractured section of the interface appeared to be mostly Al and O, with some Si and Ca, indicating mostly broken up anodic oxide with a small amount of $CaSiO_3$. Notably, there was far less C near the fracture section, which suggested that the anodic oxide broke apart during polishing where the mounting epoxy was not present to support it. Polished cross-sections of etched Al – carbonated $CaSiO_3$ IPCs were imaged with optical microscopy and SEM, and elemental distribution was determined with EDS in order to understand the effect of the etching on interface interaction. (Fig. 5.17) Low magnification images showed good contact between the carbonated $CaSiO_3$ and the etched Al surface. (Fig. 5.17 a) Every site of pitting and roughness on the Al appeared filled with the ceramic. Increasing magnification with SEM showed that the etched surface voids and pits were indeed

filled with ceramic particulate. (Fig. 5.17 b) Close inspection of one surface pit showed mostly small, <1 μm, particles occupying the pit. (Fig. 5.17 c) EDS elemental mapping helped delineate the torturous structure of the Al pit, and confirmed that Si, O, and Ca were appreciably present within the pit. This supported the SEM observation that $CaSiO_3$ particulate was infiltrating the smaller features of the etched surface.

Observation of the fracture surface of each sample post compression testing was conducted with optical microscopy. (Fig. 5.18) The surface of the untreated Al (a) after fracture held small pockets of the ceramic. Separation between the bulk ceramic and metal was evident, and cracking within the bulk ceramic was also present. The zeolite coated Al (b) had much more attached ceramic post fracture compared to the untreated sample. Separation of the bulk ceramic from the Al, as well as cracking through the bulk ceramic was apparent. The anodized Al (c) surface also held more ceramic at its surface compared to the untreated sample. Again, separation between the metal and ceramic, along with cracking in the bulk ceramic was observed. Lastly, the etched Al (d) surface still had ceramic adhered to its surface after failure, more so than the untreated sample. Typical metal-bulk ceramic separation and cracking of the bulk ceramic could be seen on the fracture surface.

Closer inspection of the fracture surface of the untreated Al – carbonated $CaSiO_3$ IPC fracture interface after polishing revealed crack location with respect to the Al surface. (Fig. 5.19) Many cracks through the bulk ceramic were present breaking it into smaller fragments. (Fig. 5.19 a) The cracks ran up to and then along the Al surface, cleanly separating the Al and the carbonated $CaSiO_3$. (Fig. 5.19 b) SEM images again

showed cracking throughout the bulk ceramic, with fragmentation occurring. (Fig. 5.19 c) Incident cracks were observed approaching then running along the interface. (Fig. 19 d)

The polished fracture surface of the zeolite coated Al – carbonated $CaSiO_3$ IPC showed much the same failure behavior as the untreated sample. Fragmentation of the bulk ceramic along the fracture surface was evident. (Fig. 5.20 a) At the Al surface some regions retained zeolite coating/entrapped $CaSiO_3$ particles, while others appeared to have full separation between the coating and the Al. (Fig. 20 b) SEM images showed breakup of the bulk ceramic (Fig. 20 c), with little retained coating and mostly full separation. Higher magnification with EDS elemental mapping showed complete separation, indicated by the thick C layer between the Al and Si/Ca. (Fig. 20 d) This carbon represented the vacuum infiltrated mounting epoxy, which filled the cracks caused by compression.

The anodized Al – carbonated $CaSiO_3$ polished fracture surface showed differing failure behavior to that of the untreated sample. Bulk cracking within the ceramic region was similar (Fig. 21 a), but the cracks did not appear to separate the anodized layer from the Al. Rather, the anodized layer was fractured where cracks were incident from the bulk ceramic. (Fig. 21 b). Nearby the fractured anodic site, the crack propagated along the anodic layer/ceramic interface. (Fig. 21 c and d) Observation of carbon location with EDS showed epoxy filled cracks running from the bulk ceramic to the fractured anodic aluminum oxide region and also separating the Si and Ca region from the Al and O region where the anodic layer appeared intact.

The etched Al – carbonated $CaSiO_3$ polished fracture surface also had different cracking behavior near the metal-ceramic interface. Typical cracking through the bulk ceramic was observed. (Fig. 22 a and c) Near the Al surface, the cracks did not run along the metal-ceramic interface. (Fig. 22 b and d) Rather, the crack split the carbonated $CaSiO_3$ entrapped in the etched surface from the bulk ceramic. A band of C was observed with EDS that did not follow the Al edge. Si and Ca were clearly positioned next to the Al, indicating a region of entrapped carbonated $CaSiO_3$ that had split from the bulk.

5.4 Discussion

Consistent green densities across all the sample types indicated that pretreating the Al surface did not have an effect on the ability of the $CaSiO_3$ suspension to infiltrate the foam. (Fig. 5.2) Modification of the infiltration process was only necessary for the zeolite coated Al foams. A simple pre-wetting was found to be sufficient to avoid dehydration of the $CaSiO_3$ suspension. (Fig. 5.1) Carbonation was also unchanged by modification of the Al surface. (Fig. 5.3) Thus, the infiltration and carbonation process was deemed viable even with highly variable Al foam surfaces.

Changes in the Al foam compression behavior were observed with the different surface treatments. (Figs. 5.4-7) The anodized Al foam had comparably more ‘brittle’ behavior than the untreated Al foam, most notable from the large drop in stress after the initial maximum. The etched Al foam was weaker, but still maintained the same overall behavior as the untreated Al foam. The zeolite coated Al foam did not show any

appreciable change. These changes (or lack thereof) in compression behavior were most likely due to the different nature of each surface treatment.

The zeolite coating was formed from a precursor solution containing an Al source. Dissolution of the Al foam was not needed to generate Al ions required for the zeolite formation. Additionally, the initial growth of the coating was observed to begin quickly, less than 30 min. It followed that once the coating covered a portion of the Al, that region would no longer be susceptible to dissolution by the reaction solution. Overall the zeolite coating did not significantly affect the underlying Al surface. Thus compression behavior would remain very similar to an untreated Al foam.

The 'brittle' behavior of the anodized Al foam was also attributed the manner of its formation. The Al in the anodic oxide layer was generated via dissolution of the Al foam surface by the H_2SO_4 solution. Oxygen ions driven to the cathode surface by the applied field then reacted with the available Al to form an aluminum oxide. The net effect of this process was an anodic coating that grew into the Al surface as it simultaneously grew away from it. Thus two important structural changes occurred through the anodizing process. First, a brittle aluminum oxide coating was formed on the Al foam surface. Second, the overall thickness of the Al foam struts was reduced, effectively lowering the local ductility of the material. These structure differences account for the compression behavior. The initial maximum and subsequent steep reduction in stress likely corresponded to cracking and failure of some of the brittle anodic coating. The repeated peak – trough stress vs. strain suggested that stress concentrated at certain regions of the foam and brittle anodic coating. Once an area

failed, another one would then take the concentrated load. Eventually, the behavior appeared to be that of a typical densifying foam, indicating that enough Al remained for high strain ductile behavior.

The lower strength of the etched Al foam was simply explained by a decrease in Al strut thickness from mass loss during HCl etching. Thinner Al struts would experience an increased stress at the same applied load due to a reduction in cross-sectional area. Thus, the bulk stress vs. strain response showed a lower yield and initial maximum stress. The etched Al foam was still ductile and displayed the typical increasing strain response: a period of constant stress resistance as its cells collapsed, followed by stress increase at high strain associated with densification.

The infiltrated Al foams all displayed similar compression behavior. (Figs. 5.8-11) Average ultimate strength and elastic moduli were also very similar, with all the standard deviations overlapping. (Figs. 5.12-13) The lack of significant difference between the samples suggested that the surface modifications did not play an appreciable role in bulk mechanical properties. The microstructure of the interface was observed to provide insight into why changing surface roughness did not correlate with changes in bulk strength. Three potential issues were proposed that might negate enhancement by surface modification. 1) The infiltrated $CaSiO_3$ particles may not have been able to embed at the roughened surface. 2) Sufficient entrapment occurred, but the anchoring protrusions of the surface were too weak to provide any interlock. 3) Particle entrapment was sufficient, but the connection between the anchored particles and the bulk was too weak.

Comparison between the untreated and zeolite sample interfaces suggested that both issue #2&3 were responsible for the lack of change in bulk behavior for this treatment type. Prior to fracture, carbonated $CaSiO_3$ was observed intermingled with the zeolite coating, which was adjacent to the Al surface. (Fig. 5.15) After failure, some material remained connected with the Al. (Fig. 5.18) However, closer inspection revealed many regions of complete separation between the Al and zeolite/entrapped $CaSiO_3$ particulate. (Fig. 5.20) Thus, both the adhesion between the zeolite coating and the Al surface, and the connection between the bulk $CaSiO_3$ and the $CaSiO_3$ within the zeolite coating was insufficient to creates an appreciable change in bulk mechanical behavior of the IPC.

The anodized Al – carbonated $CaSiO_3$ IPC interface suffered from issue #1. Inspection of the interface clearly showed no intermingling of the $CaSiO_3$ and the anodic aluminum oxide coating. (Fig. 5.16) After failure, damage to the anodic layer was apparent, and cracking in the bulk of the ceramic coincided with the damaged regions. (Fig. 5.21) This suggested that either an incident crack from the bulk caused fracturing of the anodic layer, or that initial damage at the anodic layer served as a stress concentrated crack origination location. Separation was also apparent along the anodic layer and carbonated $CaSiO_3$ after failure. Thus, the lack of interaction between the anodic layer and the bulk ceramic, along with the anodic layer potentially initiating/being damaged from incident cracks resulted in no enhancement in compression response.

The etched Al – carbonated $CaSiO_3$ IPC interface failed in accordance with issue #3. Good entrapment of $CaSiO_3$ particles was observed before failure. (Fig. 5.17) After failure, cracks did not reach the Al surface, but instead split the bulk ceramic from that trapped in the etched surface roughness. (Fig. 5.22) These cracks may have originated in the ceramic bulk at a stress concentration, or near the Al surface. During bulk compression, many portions of the metal-ceramic interface would be off-axis with the applied load. Locally, the ceramic likely experienced a shearing effect, where the applied load acted against the retaining 'normal' force of the etched surface. As previously shown in chapter 3, the ceramic was weak in bending, and it was believed that it was comparably weak in shear as most brittle materials are. Thus, since the area of ceramic experiencing the shearing force was small, the effective shear stress was likely high enough to initiate failure.

From the three different sample types and respective inferences on failure, the following requirements for an improved interface were drawn. The coating must be well adhered to the Al surface to avoid removal with the bulk ceramic. The coating must also have adequate sites for interlock, otherwise splitting between the coating and bulk ceramic will occur. Finally, the features providing interlock should be large enough to allow significant entrapment of the infiltrated ceramic. Small features risk reducing the effective area under shear loading, thus increasing the likelihood of locally exceeding the max shear stress of the ceramic.

5.5 Conclusion

Infiltration and carbonation of a $CaSiO_3$ suspension into surface modified Al foams was successfully conducted. Little modification of processing was required to achieve comparable green density of about 1.8 g/cm^3 and carbonation extent of 45-50%. Etching produced the greatest amount of particle entrapment, followed by zeolite coatings. Anodized Al did not appreciably hold infiltrated $CaSiO_3$ particles. In all treatments, no appreciable change in compression behavior was observed with all maximum strengths in the 106-115 MPa range and elastic moduli between 44-52 GPa. While cracking behavior at the metal-ceramic interface did vary, the typical cracking and fragmentation of the bulk carbonated $CaSiO_3$ remained unchanged between the sample types. Thus it was concluded that the applied Al surface modifications did not change the IPC mechanical properties.

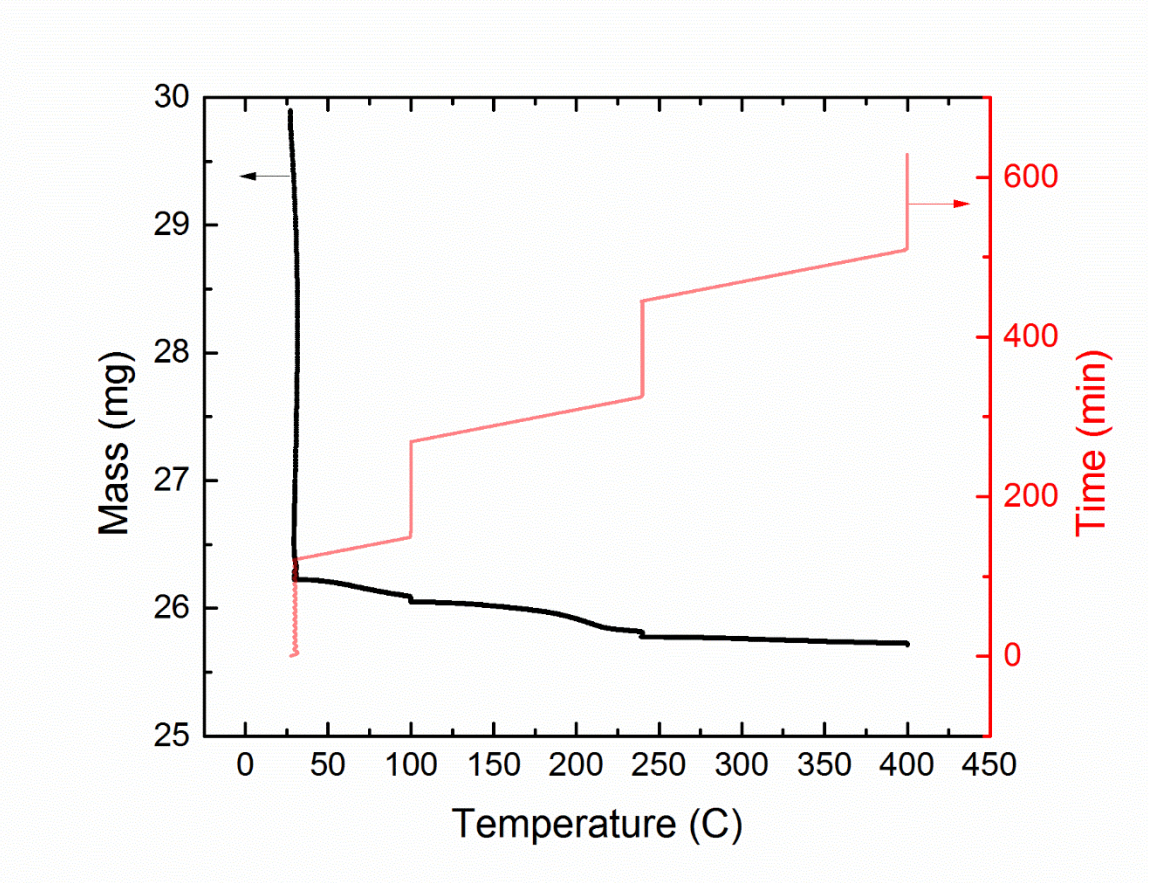

Figure 5.1. TGA plot of water saturated zeolite coated Al foam. Long holds were applied at ambient, 100, 250, and 400˚C.

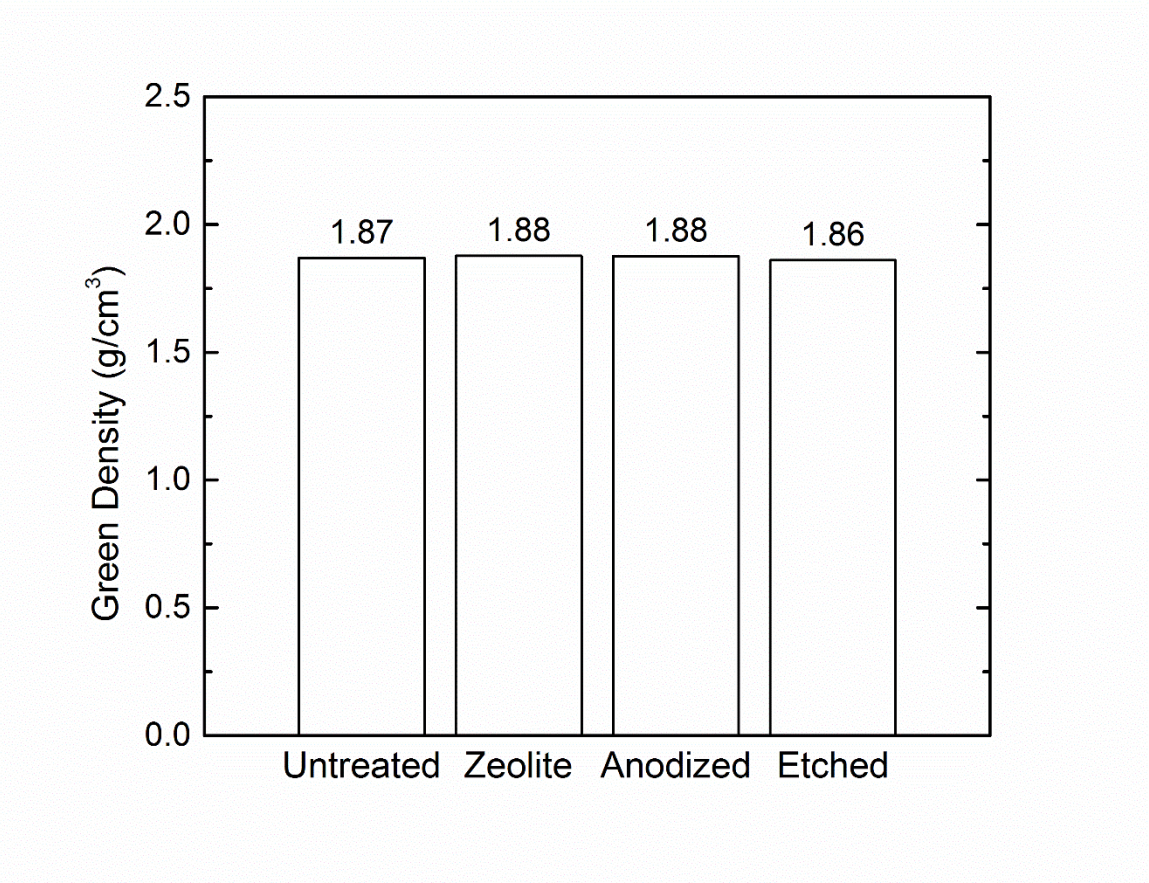

Figure 5.2. Green density of the infiltrated $CaSiO_3$ within the untreated, zeolite coated, anodized, and etched Al foams.

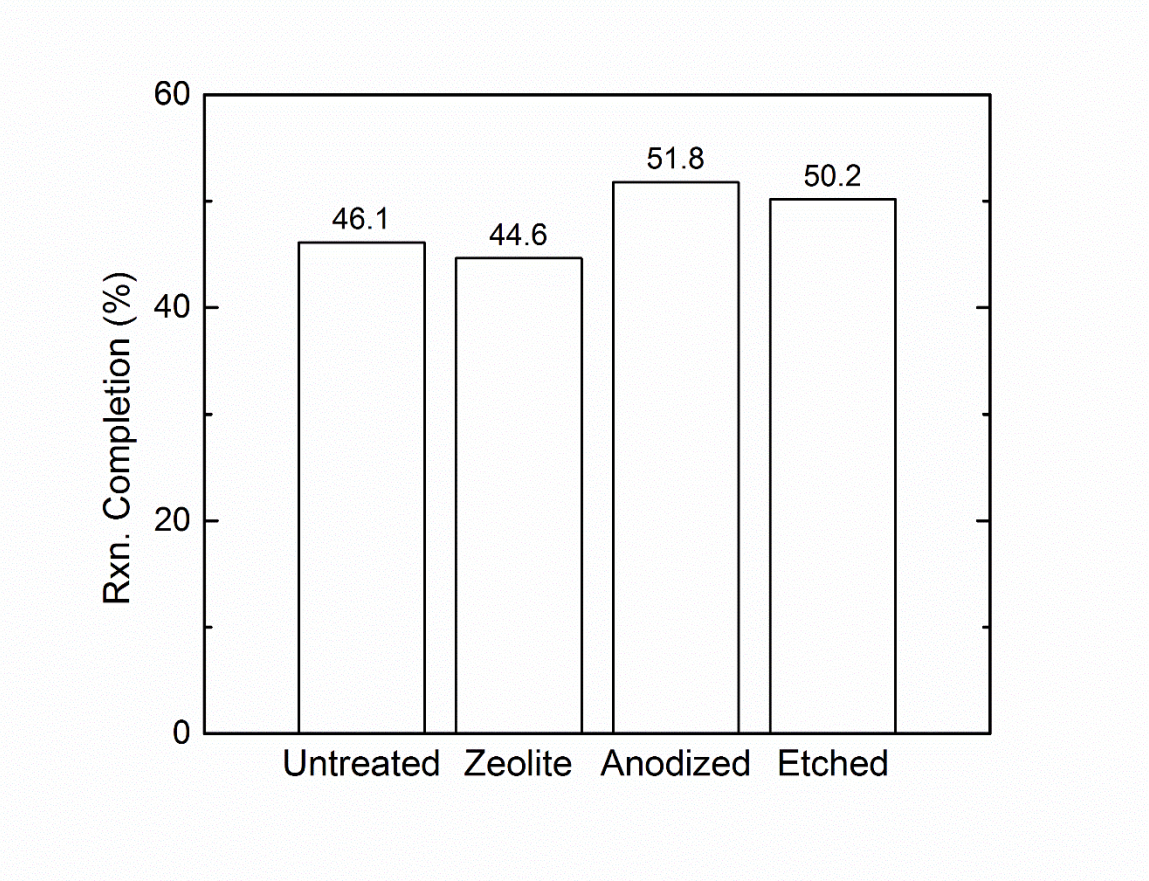

Figure 5.3. Reaction completion of infiltrated CaSiO3 within untreated, zeolite coated, anodized, and etched Al foam.

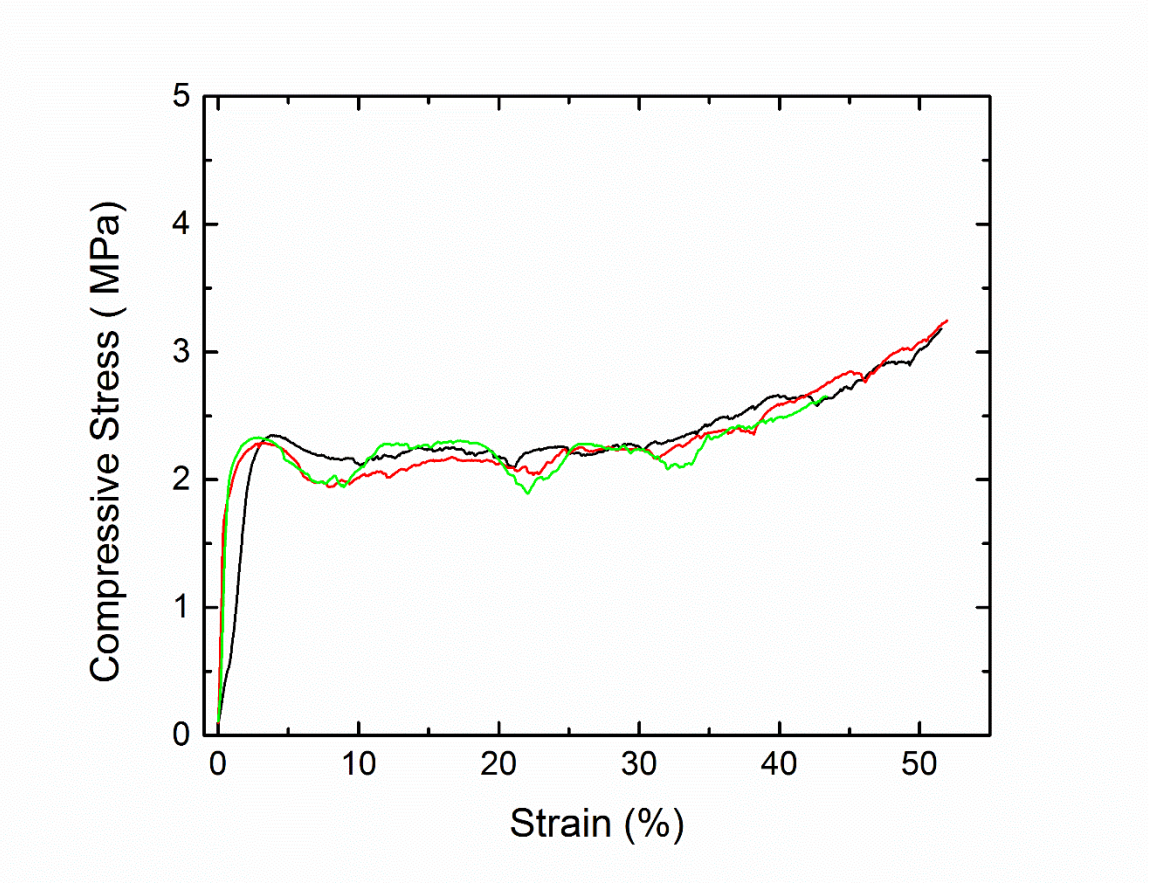

Figure 5.4. Compression behavior of untreated Al foam.

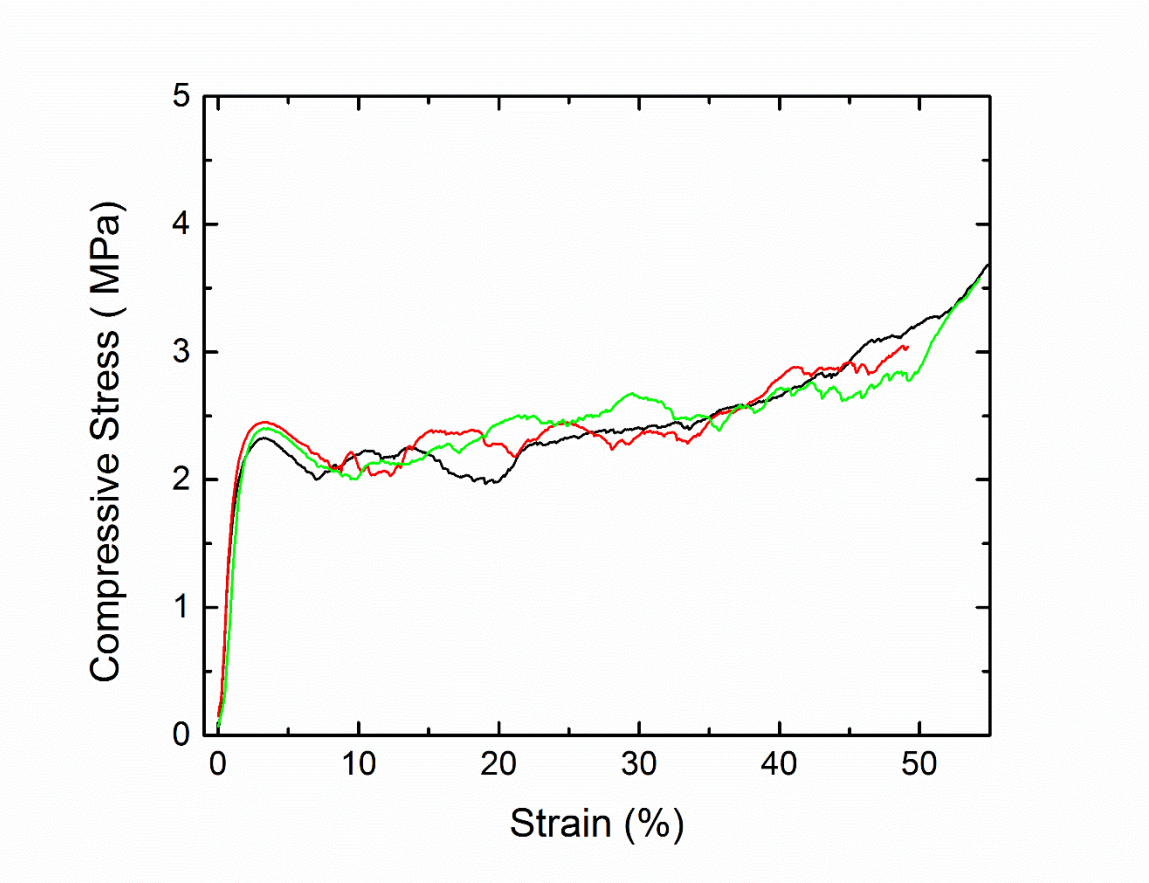

Figure 5.5. Compression behavior of zeolite coated Al foam.

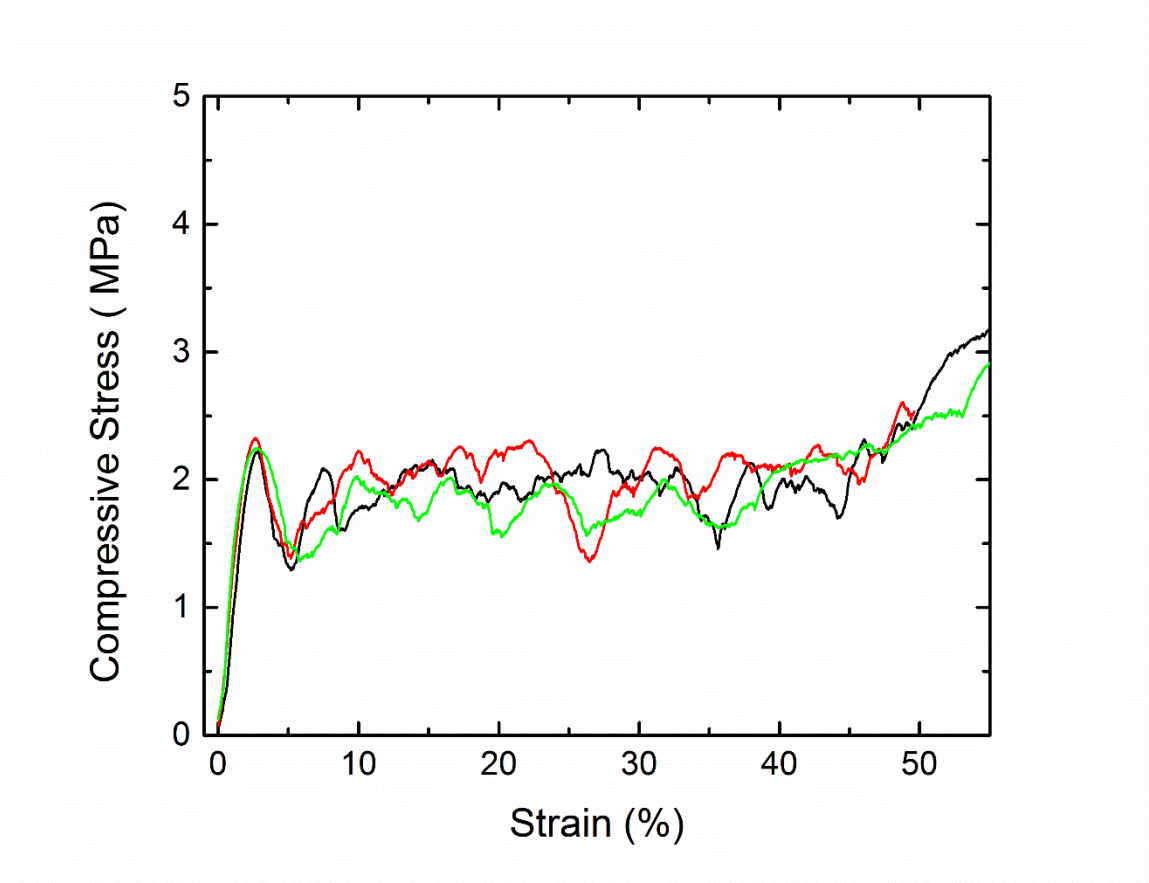

Figure 5.6. Compression behavior of anodized Al foam.

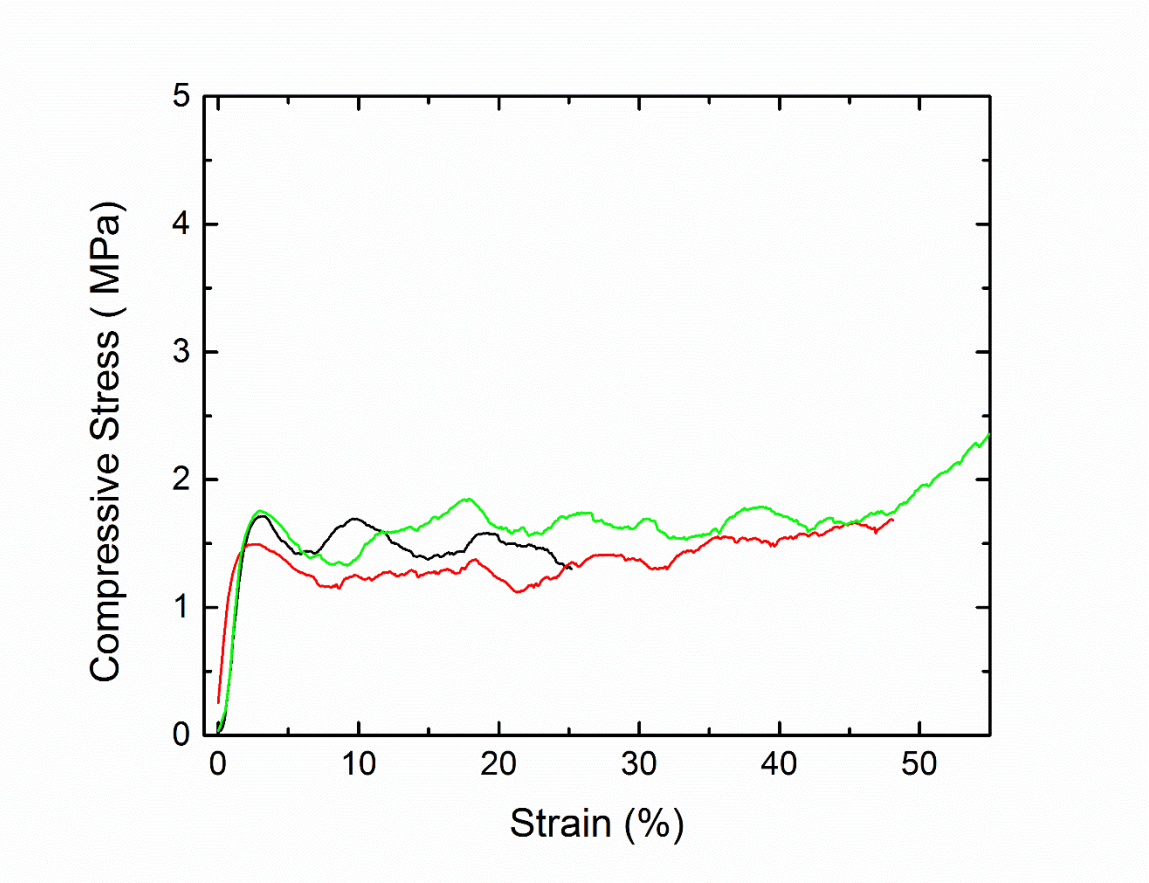

Figure 5.7. Compression behavior of HCl etched Al foam.

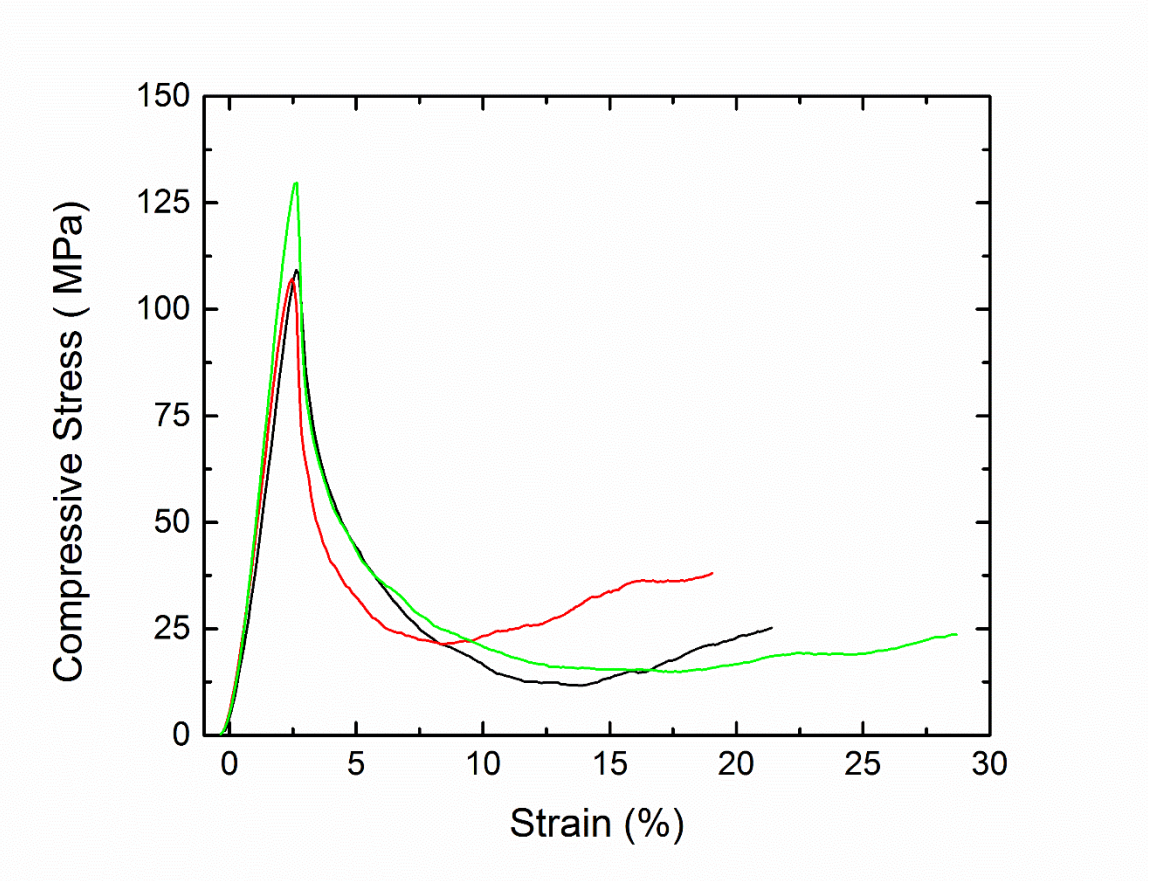

Figure 5.8. Compression behavior of an untreated Al – carbonated $CaSiO_3$ IPC.

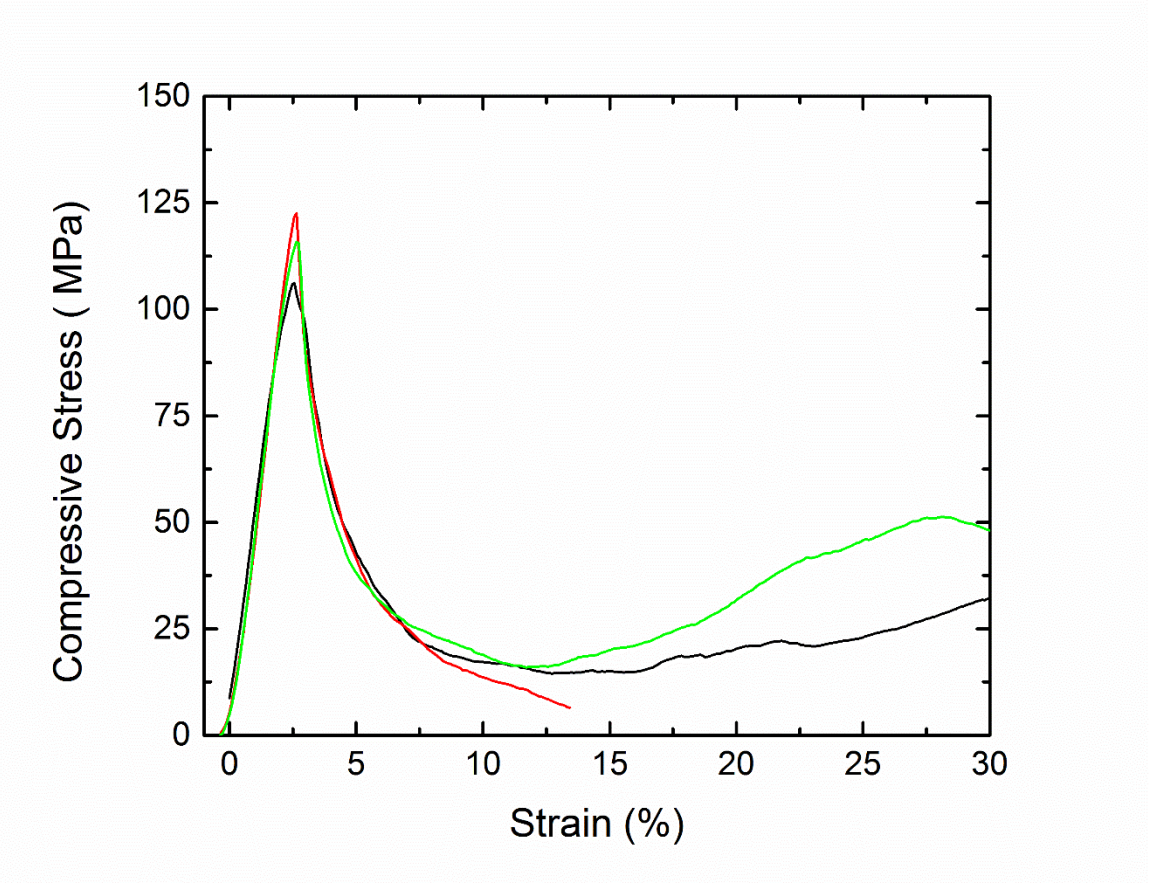

Figure 5.9. Compression behavior of zeolite coated Al-carbonated $CaSiO_3$ IPC.

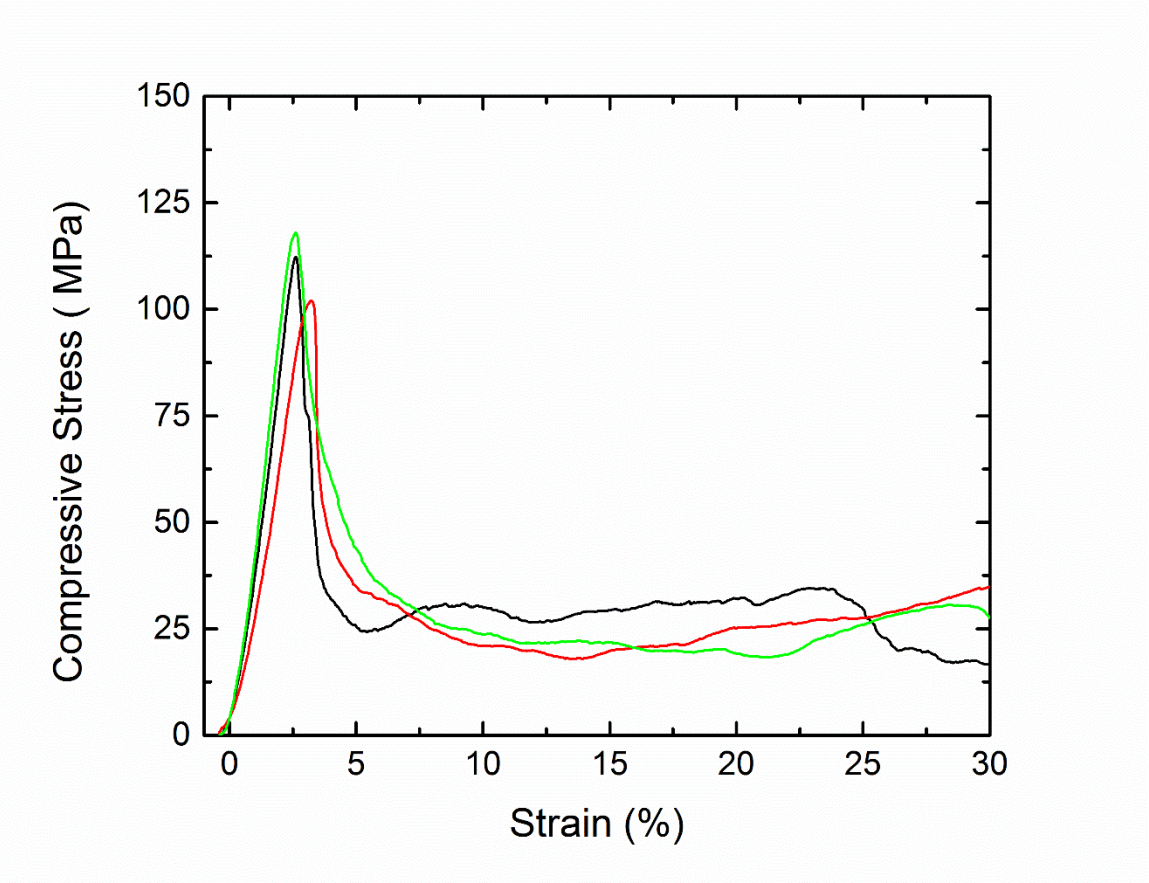

Figure 5.10. Compression behavior of an anodized Al – carbonated $CaSiO_3$ IPC.

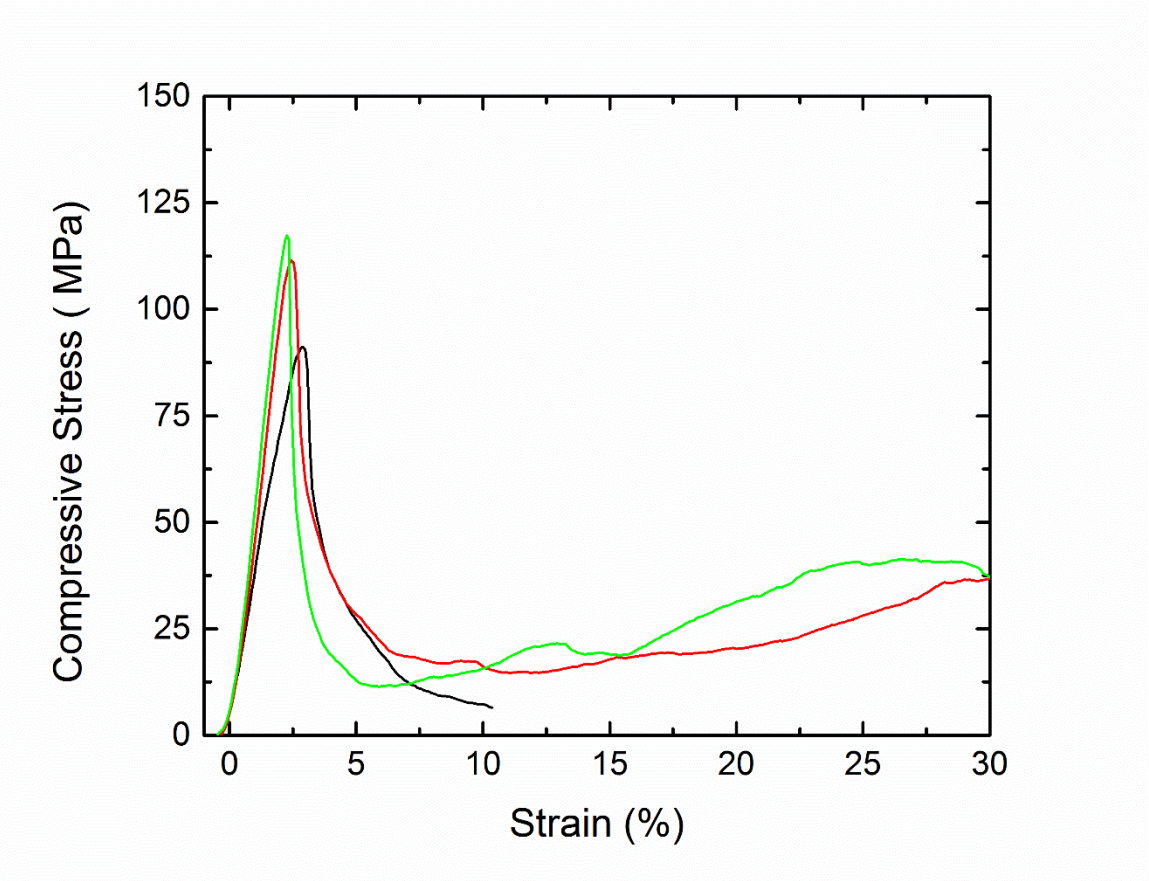

Figure 5.11. Compression behavior of HCl etched Al foam – carbonated $CaSiO_3$ IPC.

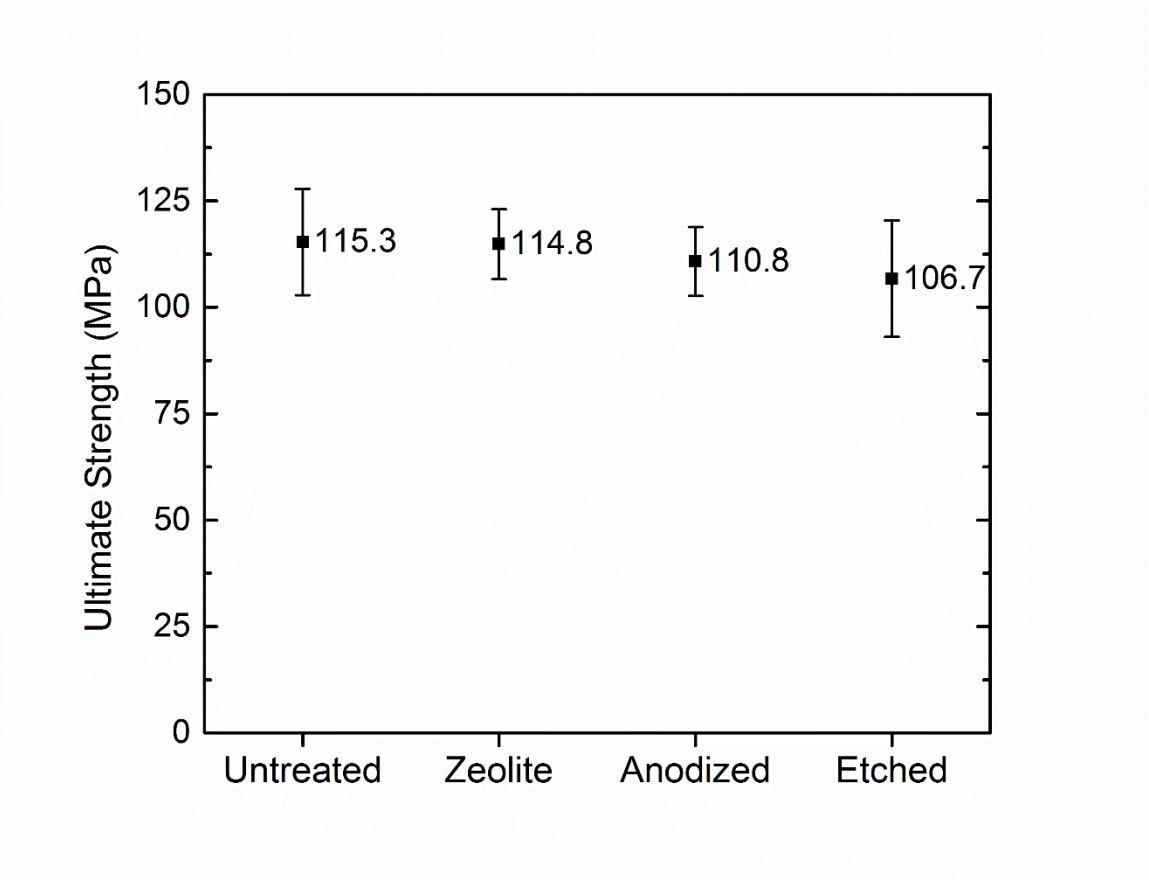

Figure 5.12. Maximum strength of the untreated, zeolite coated, anodized, and HCl etched Al – carbonated $CaSiO_3$ IPCs.

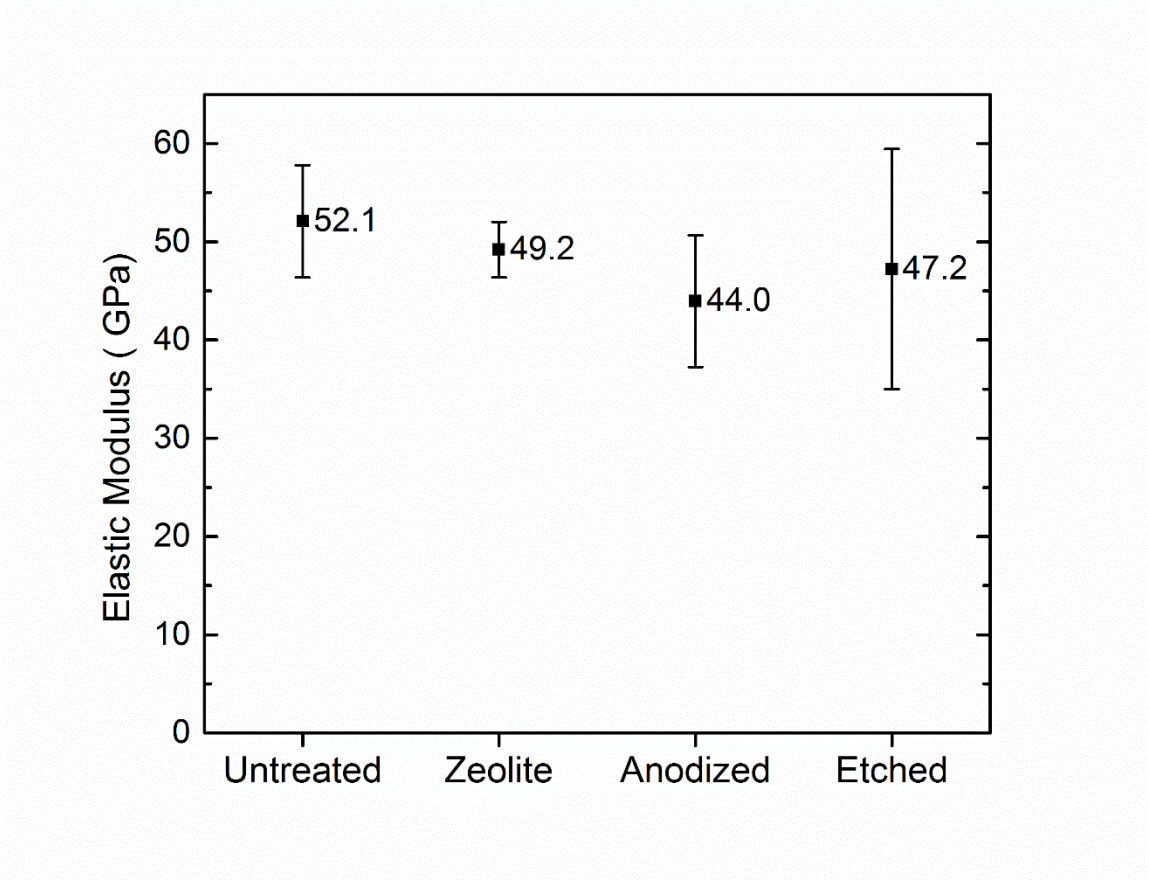

Figure 5.13. Elastic modulus of the untreated, zeolite coated, anodized, and HCl etched Al – carbonated $CaSiO_3$ IPCs.

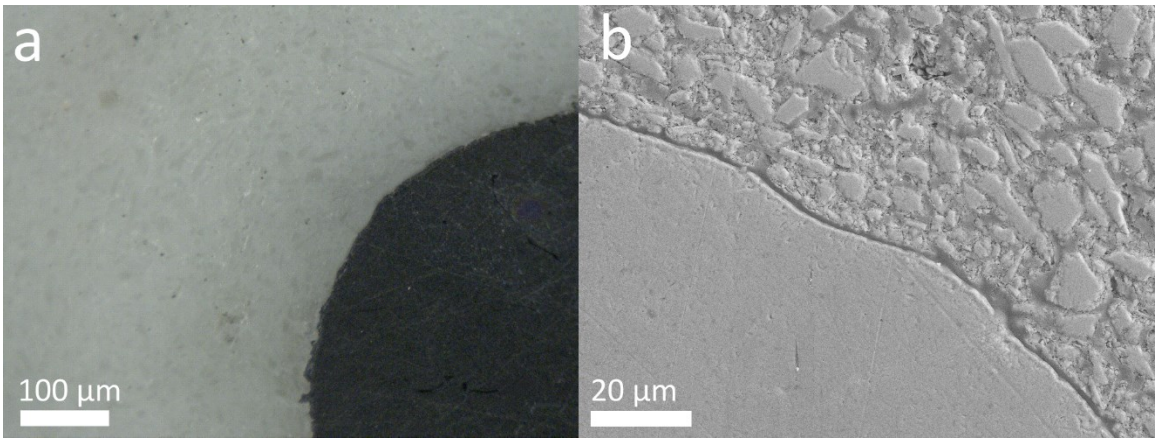

Figure 5.14. Optical (a) and SEM (b) images of the untreated Al – carbonated $CaSiO_3$ IPC interface.

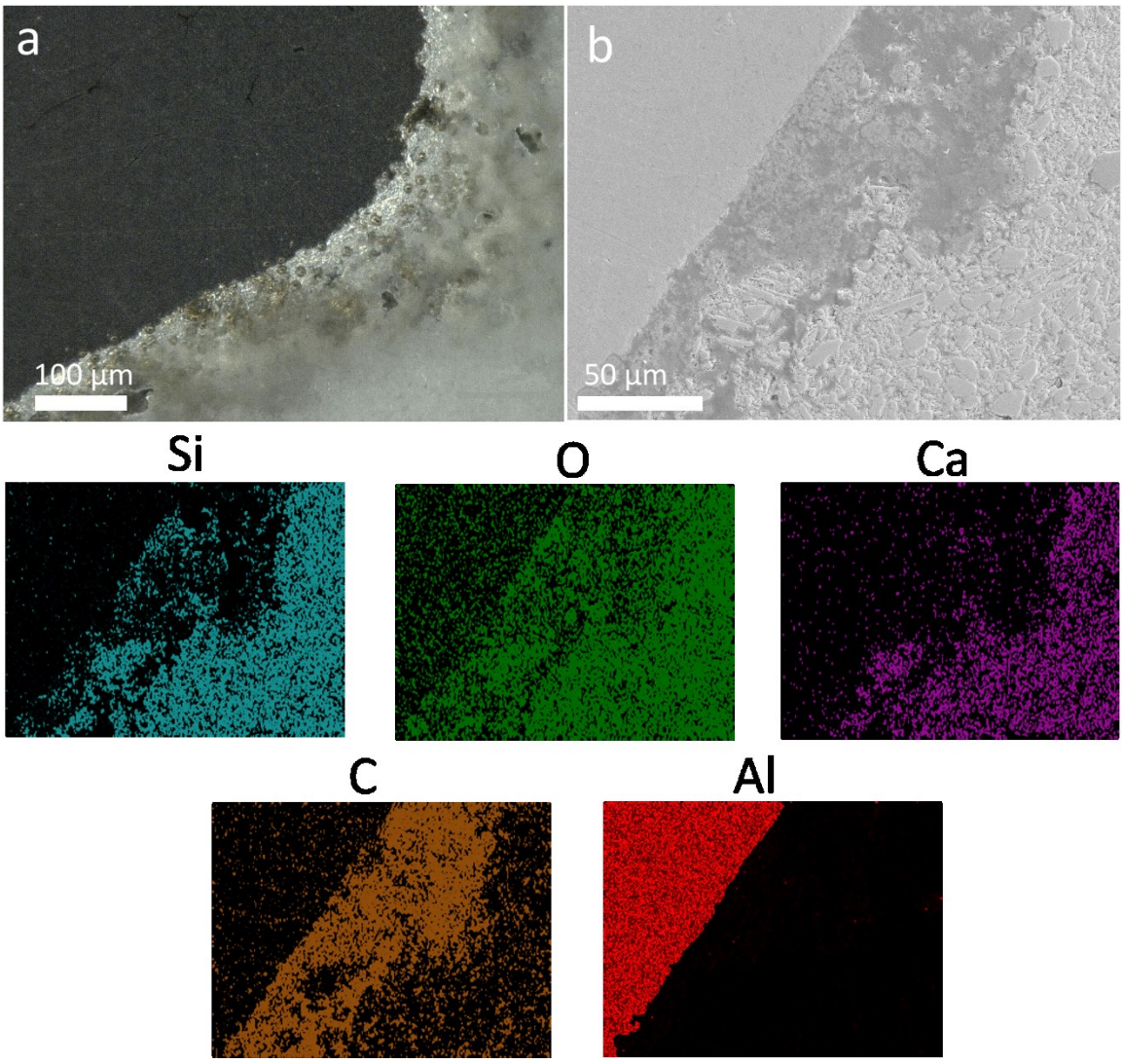

Figure 5.15. Optical (a) and SEM (b) images of the zeolite coated Al – carbonated $CaSiO_3$ IPC interface. EDS elemental mapping showed relative positioning of the infiltrated $CaSiO_3$ with the zeolite coating and Al surface.

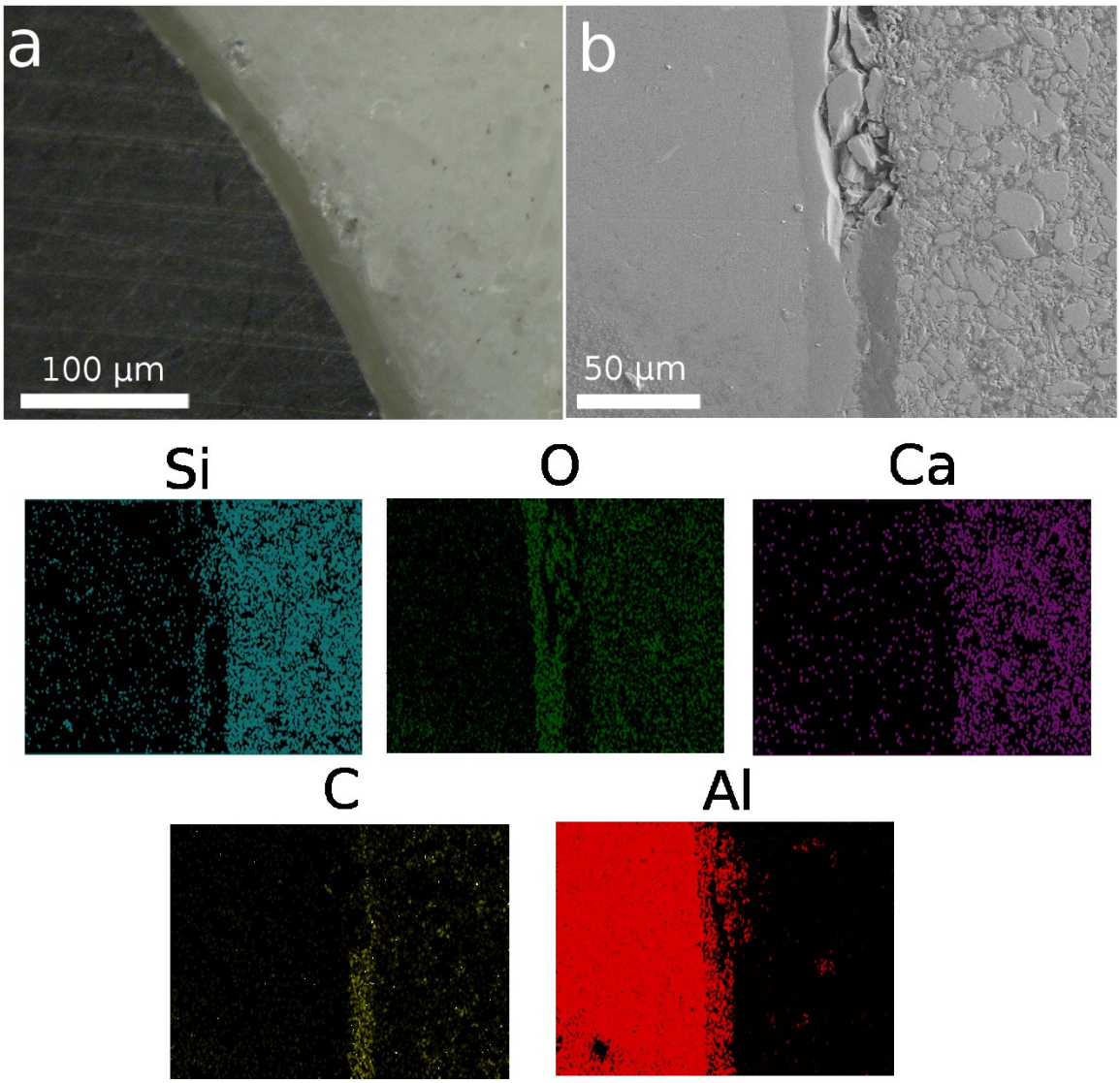

Figure 5.16. Optical (a) and SEM (b) images of the anodized Al – carbonated $CaSiO_3$ IPC interface. EDS elemental mapping showed relative positioning of the infiltrated $CaSiO_3$ with the anodic aluminum oxide layer and Al surface.

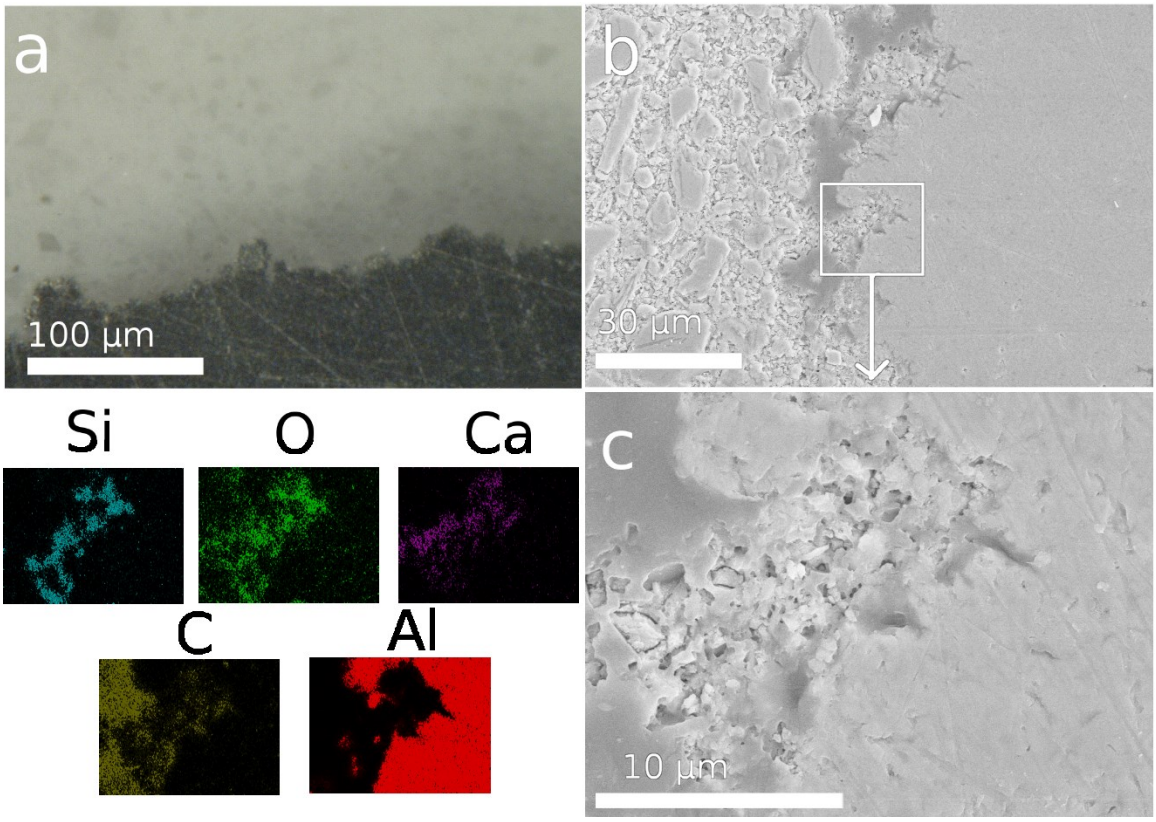

Figure 5.17. Optical (a) and SEM (b and c) of the etched Al – carbonated $CaSiO_3$ IPC interface. A region of (b) was magnified (c) to highlight the incorporation of $CaSiO_3$ particles in the etched regions. EDS elemental mapping showed relative positioning of the infiltrated $CaSiO_3$ within the structure of the etched Al surface.

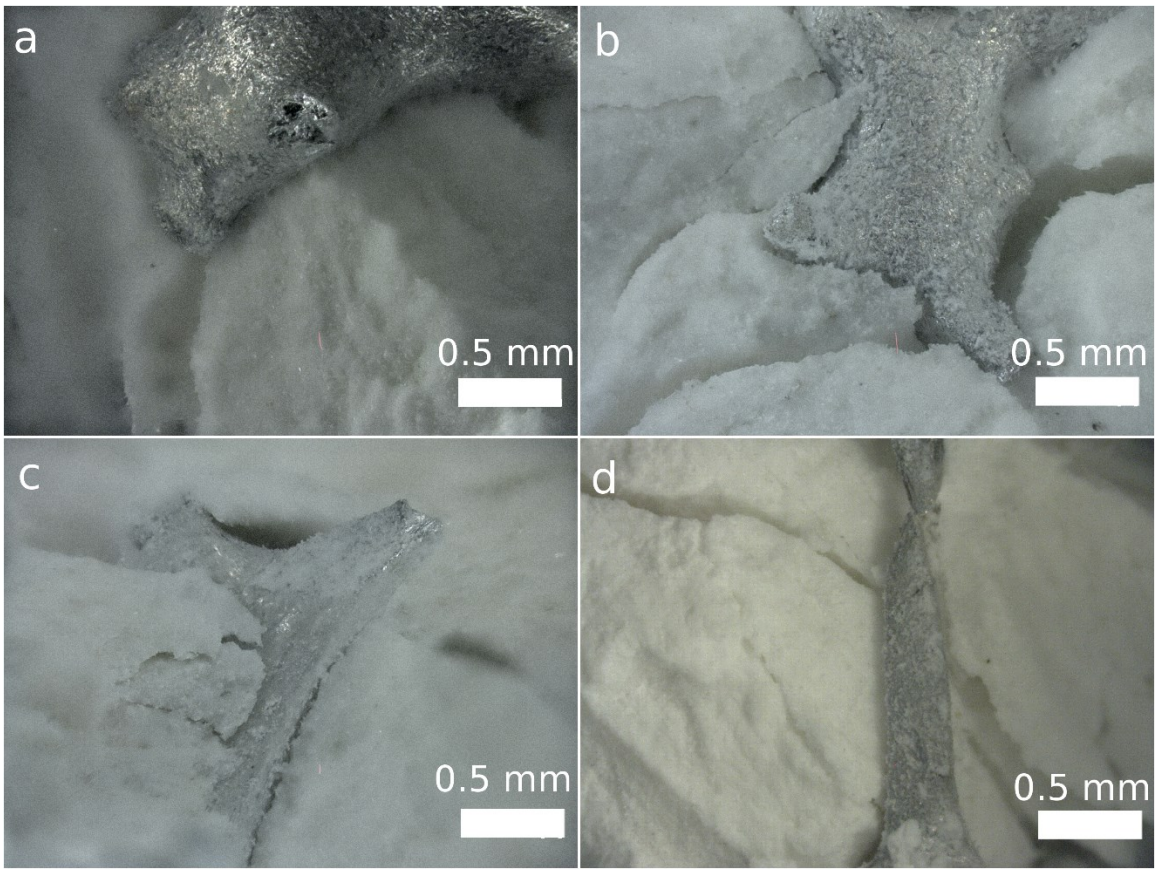

Figure 5.18. Optical image comparison of the (a) untreated, (b) zeolite coated, (c) anodized, and (d) etched Al – carbonated $CaSiO_3$ IPC fracture surfaces. Typical separation between the ceramic and metal was observed along with cracking in the ceramic bulk. Zeolite coated (b) and etched (d) samples had more ceramic still adhered to the Al surface compared to the (a) untreated samples. Anodized (c) samples had a slightly more ceramic adherence than the (a) untreated samples.

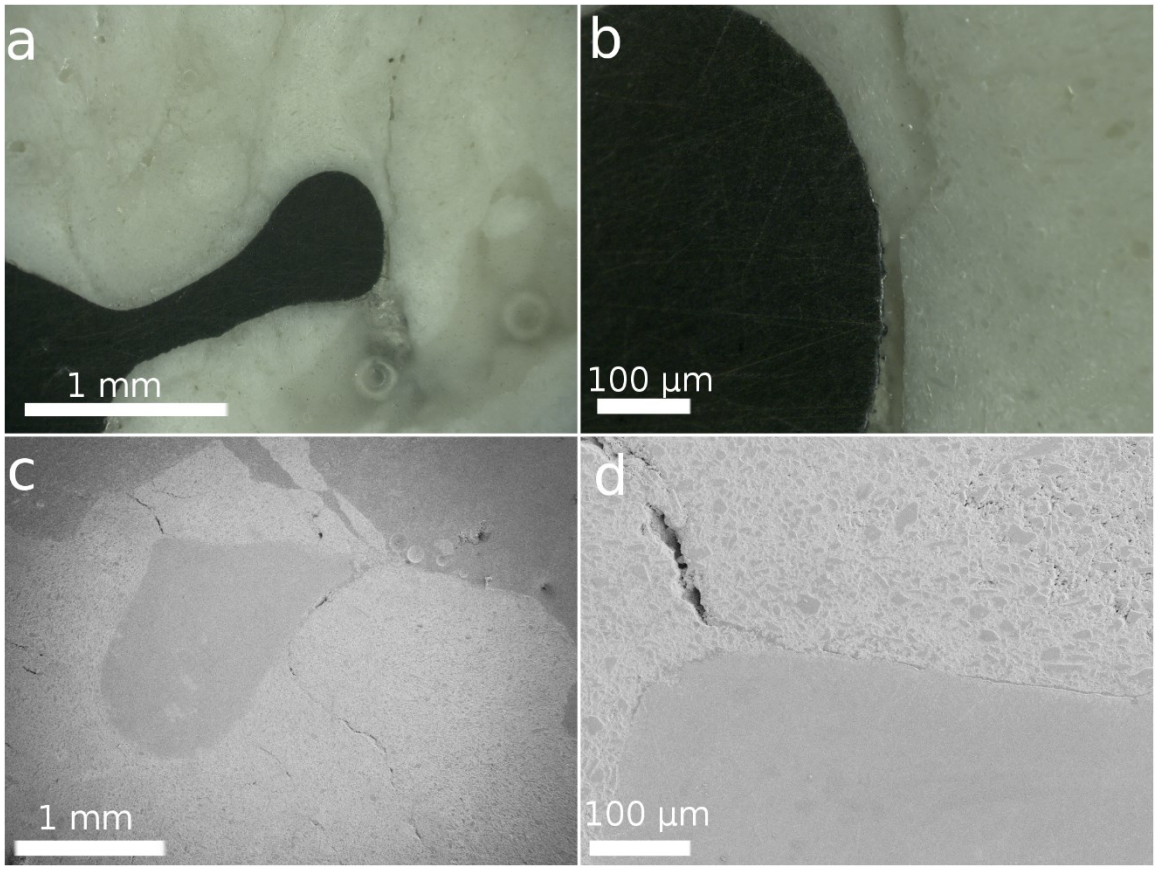

Figure 5.19. Optical (a and b) and SEM (c and d) images of the polished fracture surface of an untreated Al – carbonated $CaSiO_3$ IPC. The lower magnification images showed cracks running throughout the ceramic regions and along the edge of the Al (a and c). Higher magnification showed complete separation of the ceramic and metal where cracks meet the Al surface (b and d).

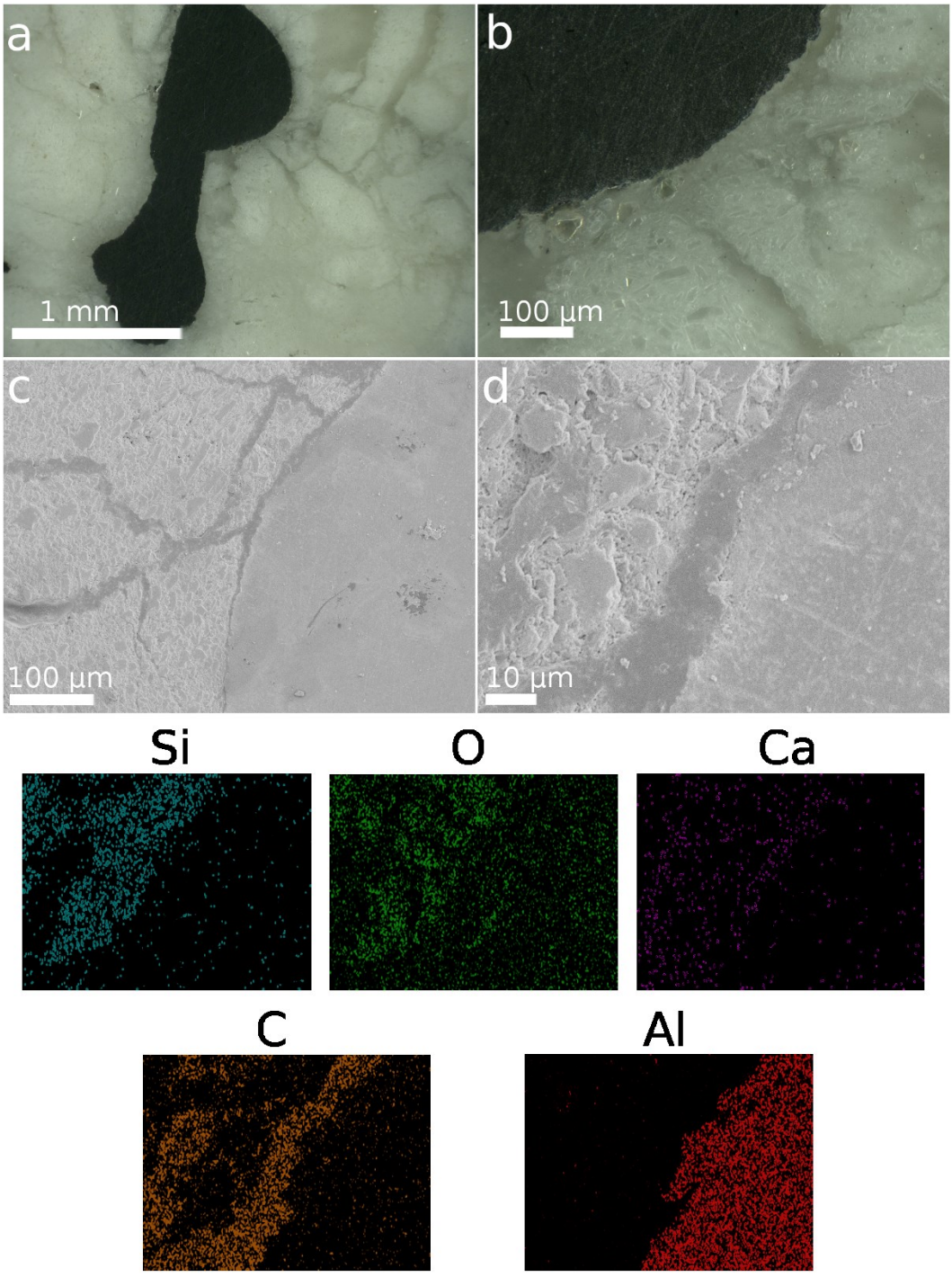

Figure 5.20. Optical (a and b) and SEM (c and d) images with EDS elemental mapping of (d) of the zeolite coated Al – carbonated $CaSiO_3$ IPC polished fracture surface. Some material remained attached to the Al surface (b), however full removal of the coating and carbonated $CaSiO_3$ was also evident along many cracks (c and d). Carbon fully separating the Al from carbonated $CaSiO_3$ was noted from EDS.

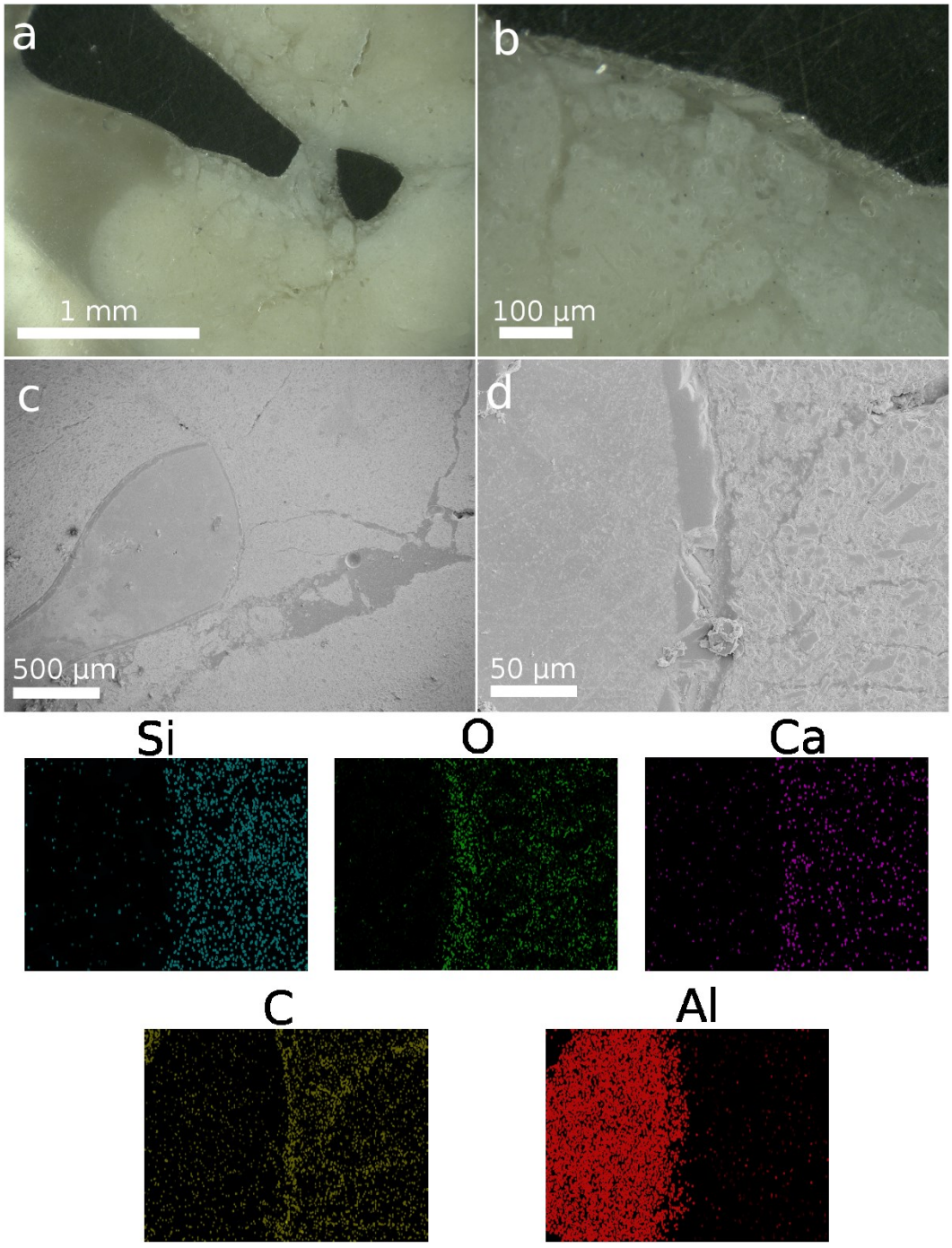

Figure 5.21. Optical (a and b) and SEM (c and d) images with EDS elemental mapping of (d) of anodized Al – carbonated $CaSiO_3$ IPC polished fracture surface. Cracks appeared to run into the anodic oxide layer, and damage of the anodic layer was apparent at the intersection (a-d). Separation was also apparent

between anodic oxide layer and the carbonated $CaSiO_3$ as seen in (d) and by the presence of carbon in between.

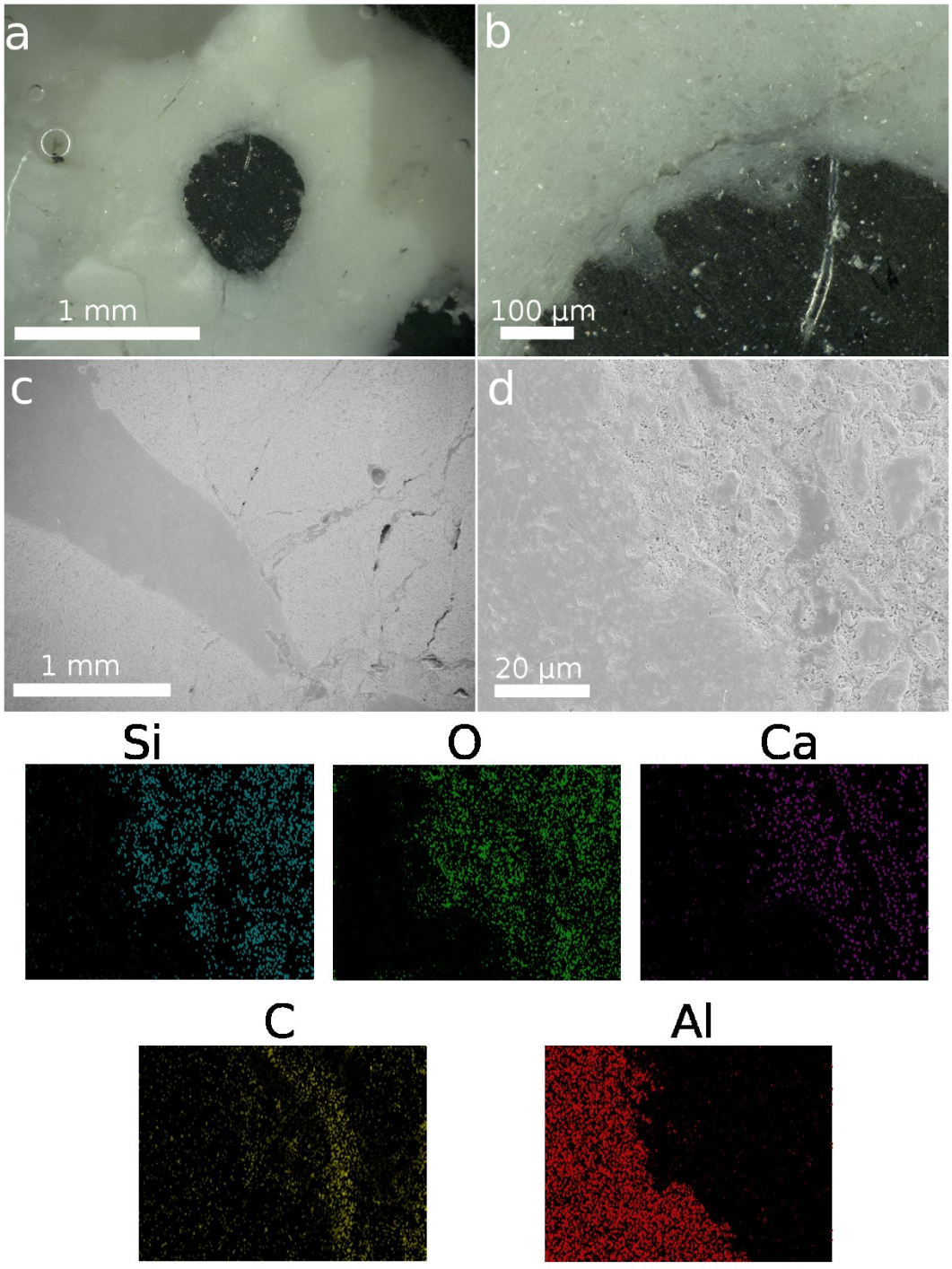

Figure 5.22. Optical (a and b) and SEM (c and d) images with EDS elemental mapping of (d) of the etched Al – carbonated CaSiO3 IPC polished fracture surface. Cracking did not reach the Al surface, instead approaching then running parallel to the Al surface with a portion of carbonated CaSiO3 in between. A

carbon filled crack was apparent running through the ceramic region, separating entrapped carbonated $CaSiO_3$ particles from the bulk.

6. Conclusions

The goal of this dissertation was to produce and characterize an Al-carbonated $CaSiO_3$ metal-ceramic IPC using processes that fit the new fabrication paradigm. Four overlapping studies were conducted. First, a novel process for fabrication of metal-ceramic IPCs was covered, detailing the creation of $CaSiO_3$ suspensions, infiltration of Al foams, and carbonation of the composite. Second, the mechanical behavior and interface characteristics of the formed IPCs was examined. Third, modification of the Al foam surface was performed with the aim of improving the metal-ceramic interaction of the IPC. Finally, the effect of Al modification on mechanical behavior and interface characteristics of the IPC was evaluated.

The aim of the first study was to engineer a $CaSiO_3$ suspension capable of infiltrating an Al foam and assess uniformity of the green density and carbonation extent of the infiltrated $CaSiO_3$. Suspensions were manipulated via pH adjustment to 12-12.5 and addition of <1% sodium polyacrylate dispersant leading to increased particle repulsion resulting in lowered suspension viscosity. High solids (58 vol%) $CaSiO_3$ suspensions with flow properties suitable for pressureless infiltration were formed. Subsequent infiltration into Al foam yielded comparable green density (~1.8 g/cm^3) and carbonation (~45%) to ceramic only samples. This total process was conducted at temperatures ≤ 90˚C, no applied pressure, and ≤ 20 psig CO_2 reactor pressure. Thus, the high temperatures, high pressures, wetting agents, and stringent atmospheric control

normally associated with infiltration formed metal-ceramic IPCs were avoided and the process fit the paradigm for more sustainable IPC fabrication.

The aim of the second study was to determine the mechanical properties of and characterize the metal-ceramic interface of the formed Al-carbonated $CaSiO_3$ IPCs. Samples were formed via the infiltration and carbonation procedure and tested in compression and in bending. Optical and SEM imaging of sample cross-sections and fracture surfaces were performed to observe the metal-ceramic interface. EDS and XPS were used to evaluate the chemical nature of the interface. Compression strength averaged ~116 MPa across the three IPC types and load was resisted after failure past 35% strain. Both properties were markedly improved over the individual composite components. With average bulk density of 2.2 g/cm^3 and 116 MPa strength, the IPC fit between Al-polymer and Al-ceramic IPC property space. Evidence of chemical interaction between the aluminum and carbonated wollastonite was not found, suggesting that any adhesion was mechanical in nature.

The objective of the third study was to adapt processing routes for roughening the Al foam surface of an Al-carbonated $CaSiO_3$ IPC using three established methods: (1) zeolite growth, (2) anodizing Al, and (3) HCl etching. Zeolite coatings were grown in a solution with precursor molar ratios of $5Na_2O$: 1 Al_2O_3: 10 SiO_2: 300 H_2O: 5 TEA at 70˚C for 15-30 min. Coatings processed at these conditions had 50 µm thick, highly porous structure, suitable for entrapping $CaSiO_3$ particles. Anodized coatings were grown in a 2 M H_2SO_4 solution at 20˚C with 1.5 A/dm^2 current for 30 min. Anodic oxide coatings processed in these conditions provided cracks running parallel to the Al struts and

smaller dimpling across the surface that may improve mechanical interlock with infiltrated $CaSiO_3$. HCl etching was performed in a 4 M HCl solution at ambient temperature for 5 min. Mass removal from the etching left behind multi-scale pitting suitable for entrapping clusters of $CaSiO_3$ particles. Each of the applied processes produced comparatively unique surface structure on the Al foam.

The purpose of the fourth study was to evaluate the mechanical properties of the treated Al-carbonated $CaSiO_3$ IPCs, observe the treated metal-ceramic interface, and determine what affect the Al surface modification had on the bulk IPC properties. Infiltration and carbonation of a $CaSiO_3$ suspension into surface modified Al foams was successfully conducted. Little modification of processing was required to achieve comparable green density of about 1.8 g/cm^3 and carbonation extent of 45-50%. Etching produced the greatest amount of particle entrapment, followed by zeolite coatings. Anodized Al did not appreciably hold infiltrated $CaSiO_3$ particles. In all treatments, no appreciable change in compression behavior was observed with all maximum strengths in the 106-115 MPa range and elastic moduli between 44-52 GPa. While cracking behavior at the metal-ceramic interface did vary, the typical cracking and fragmentation of the bulk carbonated $CaSiO_3$ remained unchanged between the sample types. Thus it was concluded that the applied Al surface modifications did not change the IPC mechanical properties.

In summary, this dissertation demonstrates that metal-ceramic IPCs with novel mechanical properties can be fabricated using far more sustainable conditions than current conventional processes. More specifically, low temperature (<90˚C) and

pressure (<20 psi) utilized by the g-rHLPD carbonation processing allows for densification of $CaSiO_3$ infiltrated into an Al scaffold, resulting in a strong, damage tolerant IPC. Microstructural differences of the Al surface did not cause significant changes to the bulk mechanical properties of the IPC, allowing for a variety of scaffolds to be used. Based on a review of the literature, the formed Al-carbonated $CaSiO_3$ IPC occupies a unique area of the Al IPC strength vs density property space. Therefore, it may be concluded that these properties, combined with the inherent damage tolerance of the IPC, make it a suitable candidate for replacing conventional FOB structural materials.

7. Future Work

Many interesting questions have arisen through the development and investigation of Al-carbonated $CaSiO_3$ IPCs. Notably, what range of scaffold materials can be combined with carbonated $CaSiO_3$, and are there openings in those property spaces for such an IPC to fill? How do the suspended $CaSiO_3$ particles orient during the infiltration process? Can a chemically bonded interface between the metal and ceramic be designed within the new fabrication paradigm? What is the formation mechanism of the tubules observed in the zeolite coating synthesis, can they be preferentially grown, and do they have any interesting properties? From these questions, the following routes of future work are proposed.

Exploratory research on other potential metal and plastic scaffolds should be conducted in order to identify potential openings in those materials property spaces. Suitable candidate scaffold materials can then be combined with carbonated $CaSiO_3$ via the established infiltration and carbonation procedure. This would extend the proven range of carbonated $CaSiO_3$ IPCs, and further support that the new processing paradigm is achievable in many different systems.

Closer investigation of how the $CaSiO_3$ particles interact with the Al foam during the infiltration and carbonation process should be conducted. In particular, careful, periodic sectioning of the formed composite could reveal how the $CaSiO_3$ particles orient at the Al surface, and establish if the spatial distribution of the $CaSiO_3$ particles is uniform or variable across the composite. Manipulation of the $CaSiO_3$ particle size

distribution and particle morphology might then be carried out to influence particle orientation during infiltration. Spatial mapping of carbonation extent via XRD could accompany this work as well, determining if the Al foam and $CaSiO_3$ particle orientation/distribution is uniform or variable throughout the composite.

Development of a chemically binding interface between the ceramic and metal should be studied. Cursory literature research suggests that there is not a single compound that could provide this chemical bridge, but perhaps multiple surface layers of different compounds could bind the two component-materials. Perhaps the carbonation process could be used favorably to this end.

An expansive literature review should be conducted regarding the growth of large tubule structures given the zeolite synthesis chemistry. Initial brief review of the literature did not show any reports of the observed structure. If it is actually a unique observation, an opportunity exists for research into understanding its formation, identifying ideal synthesis conditions, and characterizing the tubule to identify any useful properties.

8. References

[1] Y. Kajikawa, "Research core and framework of sustainability science," *Sustain. Sci.*, **3** [2] 215–239 (2008).

[2] World Commision on Environment and Development, *Our common future*, (1987).

[3] W. Ascher, "Policy sciences contributions to analysis to promote sustainability," *Sustain. Sci.*, **2** [2] 141–149 (2007).

[4] J.G. Canadell, C. Le Quéré, M.R. Raupach, C.B. Field, E.T. Buitenhuis, P. Ciais, T.J. Conway, N.P. Gillett, *et al.*, "Contributions to accelerating atmospheric CO2 growth from economic activity, carbon intensity, and efficiency of natural sinks.," *Proc. Natl. Acad. Sci. U. S. A.*, **104** [47] 18866–18870 (2007).

[5] C. Gardi and F. Sconosciuto, "Evaluation of carbon stock variation in Northern Italian soils over the last 70 years," *Sustain. Sci.*, **2** [2] 237–243 (2007).

[6] H. Haberl, K.H. Erb, F. Krausmann, V. Gaube, A. Bondeau, C. Plutzar, S. Gingrich, W. Lucht, *et al.*, "Quantifying and mapping the human appropriation of net primary production in earth's terrestrial ecosystems.," *Proc. Natl. Acad. Sci. U. S. A.*, **104** [31] 12942–12947 (2007).

[7] C.D. Keeling, S.C. Piper, R.B. Bacastow, M. Wahlen, T.P. Whorf, M. Heimann, and H. a. Meijer, "Exchanges of atmospheric CO2 and CO2 with the terrestrial biosphere and oceans from 1978 to 2000," *SIO Ref.*, 1–28 (2001).

[8] R. a. Houghton, "Balancing the Global Carbon Budget," *Annu. Rev. Earth Planet. Sci.*, **35** [1] 313–347 (2007).

[9] USEPA, *Carbon Dioxide Emissions*, *Overview of Greenhouse Gases*, www.epa.gov/climatechange (2014).

[10] US Army, *The Army Strategy for the environment*. 2004.

[11] Department of Defense, *Strategic Sustainability Performance Plan*. 2012.

[12] K. Dalton, *Army scientists improve garbage to energy prototype device*, www.army.mil/article/92383/ (2012).

[13] E. Worrell, L. Price, N. Martin, C. Hendriks, and L.O. Meida, "Carbon Dioxide Emissions From the Global Cement Industry," *Annu. Rev. Energy Environ.*, **26** 303–329 (2001).

[14] P.A. Lanser and A.M. Burger, "Carbon dioxide as a stimulus for life cycle thinking in cement and carbon neutral concrete building," *Concr. Prod.*, 53–58 (2008).

[15] M.F. Ashby and Y.J.M. Bréchet, "Designing hybrid materials," *Acta Mater.*, **51** [19] 5801–5821 (2003).

[16] E. Arzt, M.E. Ashby, and K.E. Easterling, "Practical Applications of Hot-lsostatic Pressing Diagrams : Four Case Studies," **14** [February] (1983).

[17] A. Bunde and W. Dieterich, "Percolation in Composites," *J. Electroceramics*, **5** [2] 81–92 (2000).

[18] R.E. Newnham, D.P. Skinner, and L.E. Cross, "Connectivity and piezoelectric-pyroelectric composites.," *Mater. Res. Bull.*, **13** [5] 525–536 (1978).

[19] M. Rosso, “Ceramic and metal matrix composites: Routes and properties,” *J. Mater. Process. Technol.*, **175** [1-3] 364–375 (2006).

[20] A.C. Allen, “The Composite Concept,” *Ceram. Ind. Mag.*, 53–59 (1966).

[21] S. Skirl, M. Hoffman, K. Bowman, S. Wiederhorn, and J. Rödel, “Thermal expansion behavior and macrostrain of Al2O3/Al composites with interpenetrating networks,” *Acta Mater.*, **46** [7] 2493–2499 (1998).

[22] Y. Huang, N. Ridley, F.J. Humphreys, and J. Cui, “Diffusion bonding of superplastic 7075 aluminium alloy,” *Mater. Sci. Eng. A*, **266** 295–302 (1999).

[23] M. Muratoğlu, O. Yilmaz, and M. Aksoy, “Investigation on diffusion bonding characteristics of aluminum metal matrix composites (Al/SiCp) with pure aluminum for different heat treatments,” *J. Mater. Process. Technol.*, **178** 211–217 (2006).

[24] H. Chen, J. Cao, X. Tian, R. Li, and J. Feng, “Low-temperature diffusion bonding of pure aluminum,” *Appl. Phys. A*, **113** [1] 101–104 (2013).

[25] H. Pierson, “The CVD of Metals;” pp. 147–184 in *Handb. Chem. Vap. Depos.* 1999.

[26] R. Fix, R.G. Gordon, and D.M. Hoffman, “Chemical Vapor Deposition of Titanium, Zirconium, and Hafnium Nitride Thin Films,” *Chem. Mater.*, **13** [34] 1138–1148 (1991).

[27] V.S.R. Murthy and B.S. Rao, “Microstructural development in the directed melt-oxidized (DIMOX) Al-Mg-Si alloys,” *J. Mater. Sci.*, **30** [12] 3091–3097 (1995).

[28] X. Zhou and Y. Tan, “Fabrication of Ceramic Composites by Directed Metal Oxidation,” *J. Wuhan Univ. Technol. Sci. Ed.*, **19** [1] 3–5 (2004).

[29] G. Cooper, “Forming processes for metal- matrix cornposites,” *Composites*, 153–159 (1970).

[30] C. San Marchi, M. Kouzeli, R. Rao, J. a. Lewis, and D.C. Dunand, “Alumina–aluminum interpenetrating-phase composites with three-dimensional periodic architecture,” *Scr. Mater.*, **49** [9] 861–866 (2003).

[31] X. Zhang, C. Hong, J. Han, and H. Zhang, “Microstructure and mechanical properties of TiB2/(Cu, Ni) interpenetrating phase composites,” *Scr. Mater.*, **55** [6] 565–568 (2006).

[32] M.N. Rahaman, *Ceramic Processing and Sintering*. CRC Press, Boca Raton, 2003.

[33] M.N. Rahaman, *Sintering of Ceramics*. CRC Press, Boca Raton, 2007.

[34] T.C. Lu, J. Yang, Z. Suo, A.G. Evans, R. Hecht, and R. Mehrabian, “Matrix Cracking in Intermetallix Composites Caused by Thermal Expansion Mismatch,” *Acta Met. mater.*, **39** [8] 1883–1892 (1991).

[35] S. Ho and Z. Suo, “Microcracks Tunneling in Brittle Matrix Composites Driven by Thermal Expansion Mismatch,” *Acta Met. mater.*, **40** [7] 1685–1690 (1992).

[36] R.K. Bordia and G.W. Scherer, “On constrained sintering—III. Rigid inclusions,” *Acta Metall.*, **36** [9] 2411–2416 (1988).

[37] K.K. Chawla, *Composite Materials Science and Engineering*, 3rd ed. Springer, 2012.

[38] I.P. Tuersley, A. Jawaid, and I.R. Pashby, “Review: Various methods of machining advanced ceramic materials,” *J. Mater. Process. Technol.*, **42** [4] 377–390 (1994).

[39] J. Warren, D.M. Elzey, and H.N.G. Wadley, "Fiber Damage During Consolidation of PVD Ti-6Al-4V Coated Nextel 610TM Alumina Fibers," *Acta Met. mater.*, **43** [10] 3605–3619 (1995).

[40] W.G. Fahrenholtz, "Reactive Processing in Ceramic-Based Systems," *Int. J. Appl. Ceram. Technol.*, **3** [1] 1–12 (2006).

[41] S. Kaur, R. Riedel, and E. Ionescu, "Pressureless fabrication of dense monolithic SiC ceramics from a polycarbosilane," *J. Eur. Ceram. Soc.*, **34** [15] 3571–3578 (2014).

[42] L. Liu, X. Li, X. Xing, C. Zhou, and H. Hu, "A modified polymethylsilane as the precursor for ceramic matrix composites," *J. Organomet. Chem.*, **693** [6] 917–922 (2008).

[43] Y. Ma and Z. Chen, "Microstructures and Properties of the C/Zr-O-Si-C Composites Fabricated by Polymer Infiltration and Pyrolysis," *J. Mater. Eng. Perform.*, **22** [9] 2510–2514 (2013).

[44] D.R. Clarke, "Interpenetrating Phase Composites," *J. Am. Ceram. Soc.*, **75** [4] 739–59 (1992).

[45] N. Travitzky, "Processing of ceramic–metal composites," *Adv. Appl. Ceram.*, **111** 286–300 (2012).

[46] R. Asthana, M. Singh, and N. Sobczak, "Infiltration Processing of Ceramic-Metal Coposites- the role of wettability reaction and capillary flow," *J. Korean Ceram. Soc.*, **42** [11] 703–717 (2005).

[47] H. Prielipp, M. Knechtel, N. Claussen, S.K. Streiffer, H. Miillejans, M. Rfihle, and J. Rded, "Strength and fracture toughness of aluminum / alumina composites with interpenetrating networks," *Mater. Sci, Eng. A.,* **197** 19–30 (1995).

[48] D.A. Weirauch, "Interfacial phenomena involving liquid metals and solid oxides in the Mg-Al-O system," *J. Mater. Res.,* **3** [4] 729-739 (1988).

[49] A.S. Nagelberg, "Observations on the role of Mg and Si in the directed oxidation of Al-Mg-Si alloys," *J. Mater. Res.,* **7** [2] 265-268 (1992).

[50] M.S. Newkirk, A.W. Urquhart, and H.R. Zwicker, "Formation of Lanxide ™ ceramic composite materials," *J. Mater. Res.,* **1** [1] 81-89 (1986).

[51] S. Wu, A.J. Gesing, N.A. Travitzky, and N. Claussen, "Fabrication and properties of Al-infiltrated RBAO-based composites," *J. Eur. Ceram. Soc.*, **7** [5] 277–281 (1991).

[52] W.G. Fahrenholtz, K.G. Ewsuk, D.T. Ellerby, and R.E. Loehman, "Near-Net-Shape Processing of Metal-Ceramic Composites by Reactive Metal Penetration," *J. Am. Ceram. Soc.*, **79** [9] 2497–2499 (1996).

[53] A.G. Merzhanov, "The chemistry of self-propagating high-temperature synthesis," *J. Mater. Chem.*, **14** [12] 1779 (2004).

[54] G. Xanthopoulou and G. Vekinis, "An overview of some environmental applications of self-propagating high-temperature synthesis," *Adv. Environ. Res.*, **5** [2] 117–128 (2001).

[55] M.M. Schwartz, *Brazing*, 2nd ed. ASM International, Materials Park, 2003.

[56] R.E. Riman, V. Atakan, J.P. Kuppler, and K.M. Smith, Precursors and Transport Methods For Hydrothermal Liquid Phase Sintering; US 2014/0093659 A1, 2014.

[57] R.E. Riman and V. Atakan, Method of Hydrothermal Liquid Phase Sintering of Ceramic Materials and Products Derived Therefrom; US 20090142578, 2009.

[58] R.E. Riman, Q. Li, S. Gupta, C. Vakifahmetoglu, V. Atakan, L. Tang, and A. Krugler, "Carbonate Ceramics by CO2 Sequestration," *Pending Submiss.*, (n.d.).

[59] S. Mukarjee, S. Mandal, and U.B. Adhikari, "Study on the physical and mechanical property of ordinary portland cement and fly ash paste," *Int. J. Civ. Struct. Eng.*, **2** [3] 731–736 (2012).

[60] *Introduction to Material Selection Charts*, www.materials.eng.cam.ac.uk/mpsite/physics/introduction/ (2014).

[61] M.F. Ashby, "On the engineering properties of materials," *Acta Metall.*, **37** [5] 1273–1293 (1989).

[62] W. Rosen, "Mechanics of Composite Strengthening;" pp. 37–75 in *Fiber Compos. Mater.* Metals Park, Ohio, 1964.

[63] J.D. Walton and W.J. Corbett, "Metal Fiber Reinforced Ceramics;" pp. 223–237 in *Fiber Compos. Mater.* Metals Park, Ohio, 1964.

[64] R.H.M. Burte, F.R. Bonanno, and J.A. Herzog, "Metal Matrix Composite Materials," *Am. Soc. Test. Mater.*, 59–92 (1966).

[65] A. Kelly, "The Nature of Composite Materials," *Sci. Am.*, 160–176 (1967).

[66] A. Moore and C.A. Calow, "What the engineer should know about composite materials," *Reinf. Plast.*, **12** 6–29 (1967).

[67] J. Binner, H. Chang, and R. Higginson, "Processing of ceramic-metal interpenetrating composites," *J. Eur. Ceram. Soc.*, **29** [5] 837–842 (2009).

[68] S. Roy, J. Gibmeier, V. Kostov, K. a. Weidenmann, a. Nagel, and a. Wanner, "Internal load transfer in a metal matrix composite with a three-dimensional interpenetrating structure," *Acta Mater.*, **59** [4] 1424–1435 (2011).

[69] R.E. Riman and V. Atakan, Systems and Methods For Carbon Capture and Sequestration and Compositions Derived Therefrom; US 8114367 B2, 2012.

[70] R. Moreno, "Colloidal processing of ceramics and composites," *Adv. Appl. Ceram.*, **111** [5&6] 246–253 (2012).

[71] E.J. Weissbart and J.D. Rimstidt, "Wollastonite: Incongruent dissolution and leached layer formation," *Geochim. Cosmochim. Acta*, **64** [23] 4007–4016 (2000).

[72] E. Green and A. Luttge, "Incongruent dissolution of wollastonite measured with vertical scanning interferometry," *Am. Mineral.*, **91** [2-3] 430–434 (2006).

[73] J. Schott, O.S. Pokrovsky, O. Spalla, F. Devreux, A. Gloter, and J. a. Mielczarski, "Formation, growth and transformation of leached layers during silicate minerals dissolution: The example of wollastonite," *Geochim. Cosmochim. Acta*, **98** 259–281 (2012).

[74] R. Hellmann, J.M. Penisson, R.L. Hervig, J.H. Thomassin, and M.F. Abrioux, "An EFTEM/HRTEM high-resolution study of the near surface of labradorite feldspar altered at acid pH: Evidence for interfacial dissolution-reprecipitation," *Phys. Chem. Miner.*, **30** [4] 192–197 (2003).

[75] E.H. Oelkers, S. V. Golubev, C. Chairat, O.S. Pokrovsky, and J. Schott, "The surface chemistry of multi-oxide silicates," *Geochim. Cosmochim. Acta*, **73** [16] 4617–4634 (2009).

[76] Vanderbilt Minerals, LLC. *Minerals and Chemicals for Ceramics Industry*. 2014.

[77] M. Turesson, C. Labbez, and A. Nonat, "Calcium mediated polyelectrolyte adsorption on like-charged surfaces," *Langmuir*, **27** [22] 13572–13581 (2011).

[78] A.A. Zaman, R. Tsuchiya, and B.M. Moudgil, "Adsorption of a low-molecular-weight polyacrylic acid on silica, alumina, and kaolin," *J. Colloid Interface Sci.*, **256** [1] 73–78 (2002).

[79] C. Flood, T. Cosgrove, Y. Espidel, I. Howell, and P. Revell, "Sodium polyacrylate adsorption onto anionic and cationic silica in the presence of salts," *Langmuir*, **23** [11] 6191–6197 (2007).

[80] M. Wang, H. Geng, X. Ge, J. Li, and D. Kou, "Polymer / Metal Interpenetrating Phase Composites Prepared via c -Ray Initiated In-Situ Emulsion Polymerization," *Polym. Compos.*, 1258-1264 (2009).

[81] L. Hu, A. Kothalkar, M. O'Neil, I. Karaman, and M. Radovic, "Current-Activated, Pressure-Assisted Infiltration: A Novel, Versatile Route for Producing Interpenetrating Ceramic–Metal Composites," *Mater. Res. Lett.*, **2** [3] 124–130 (2014).

[82] P. Chabera, A. Boczkowska, A. Ozieblo, Z. Pakiela, and K.J. Kurzydlowski, "MICROSTRUCTURE AND MECHANICAL PROPERTIES OF CERMIC-METAL COMPOSITES OBTAINED BY PRESSURE INFILTRATION," *World J. Eng.*, **11** [3] 202–207 (2011).

[83] M. Potoczek and R. Śliwa, "Microstructure and Physical Properties of AlMg/Al2O3 Interpenetrating Composites Fabricated by Metal Infiltration into Ceramic Foams," *Arch. Metall. Mater.*, **56** [4] 8–12 (2011).

[84] Y.C. Li, J.Y. Xiong, J.G. Lin, M. Forrest, P.D. Hodgson, and C.E. Wen, "MECHANICAL PROPERTIES AND ENERGY ABSORPTION OF CERAMIC PARTICULATE AND RESIN-IMPREGNATION REINFORCED ALUMINIUM FOAMS," *Mater. Forum*, **31** (2007).

[85] H. Cheng, "Compressive behavior and energy absorbing characteristic of open cell aluminum foam filled with silicate rubber," *Scr. Mater.*, **49** [6] 583–586 (2003).

[86] A. Agarwal, I. V. Singh, and B.K. Mishra, "Numerical prediction of elasto-plastic behaviour of interpenetrating phase composites by EFGM," *Compos. Part B Eng.*, **51** 327–336 (2013).

[87] T. Isopu, "Section 8 . Axial Strength of Laterally Confined Concrete;" pp. 8–1 –8–5 in *Thrity-Five Lect. Reinf. Concr.* (2008).

[88] A. Khaleek, R.K. Yadav, and C. Rajeev, "Effect of Lateral Confinement on Strength of Concrete," **1** [1] 40–44 (2012).

[89] J. Mu, Z.W. Zhu, H.F. Zhang, H.W. Zhang, H.M. Fu, H. Li, A.M. Wang, and Z.Q. Hu, "A Ti / Ti-Based-Metallic-Glass Interpenetrating Phase Composite with Remarkable Mutual Reinforcement Effect," *Adv. Mater. Sci. Eng.*, **2014** 1–7 (2014).

[90] R.D. Springer, Z. Wang, A. Anderko, P. Wang, and A.R. Felmy, "A thermodynamic model for predicting mineral reactivity in supercritical carbon dioxide: I. Phase behavior of carbon dioxide–water–chloride salt systems across the H2O-rich to the CO2-rich regions," *Chem. Geol.*, **322-323** 151–171 (2012).

[91] P. Wang, J.J. Kosinski, M.M. Lencka, A. Anderko, and R.D. Springer, "Thermodynamic modeling of boric acid and selected metal borate systems," *Pure Appl. Chem.,* 22–27 (2013).

[92] M.M. Lencka and R.E. Riman, "Thermodynamic Modeling of Hydrothermal Synthesis of Ceramic Powders," *Chem. Mater.*, **5** [1] 61–70 (1993).

[93] R.E. Riman, M.M. Lencka, L.E. Mccandlish, B.L. Gersten, A. Anderko, and S.B. Cho, "Intelligent Engineering of Hydrothermal Reactions," *Rev. High Press. Sci. Technol*, **7** 1358–1361 (1998).

[94] R.E. Riman, W.L. Suchanek, and M.M. Lencka, "Hydrothermal crystallization of ceramics," *Ann. Chim. Sci. Mat.*, **27** [6] 15–36 (2002).

[95] C. Fangjie and Z. Haiwei, "Evolution of Surface Oxide Film of Typical Aluminum Alloy During Medium - Temperature Brazing Process ," *Trans. Tiajin Univ.* **20** [1] 54–59 (2014).

[96] C.D. Wagner, "Auger and photoelectron line energy relationships in aluminum–oxygen and silicon–oxygen compounds," *J. Vac. Sci. Technol.*, **21** [4] 933 (1982).

[97] C.S. Gopinath and S.G. Hegde, "Photoemission studies of polymorphic $CaCO_3$ materials," *Mater. Res. Bull.* **37** 1323–1332 (2002).

[98] C. Aire, R. Gettu, J.R. Casas, S. Marques, and D. Marques, "Estudio experimental y modelo teórico del hormigón confinado lateralmente con polímeros reforzados con fibras (FRP)," *Mater. Construcción*, **60** [297] 19–31 (2010).

[99] F.E. Richart, A. Brandtzaeg, and R.L. Brown, "The Failure of Plain and Spirally Bound Concrete in Compression," *Univ. Illinois Eng. Exp. Stn. Bull.*, **26** [190] 1–74 (1929).

[100] D. Eberl and J. Hower, "Kaolinite synthesis. The role of the Si Al and (ALKALI) (H+) ratio in hydrothermal systems," *Clays Clay Miner.*, **23** [4] 301–309 (1975).

[101] R.A. Swalin, *Thermodynamics of Solids*, 2nd ed. John Wiley and Sons, New York, 1972.

[102] D.E. Packham, "Surface energy, surface topography and adhesion," *Int. J. Adhes. Adhes.*, **23** [6] 437–448 (2003).

[103] J.B. Wactman, W.R. Cannon, and M.J. Matthewson, *Mechanical Properties of Ceramics*, 2nd ed. John Wiley and Sons, 2009.

[104] W. Kim, K. Kim, C. Jang, H. Jung, and J.-J. Lee, "Micro- and nano-morphological modi fi cation of aluminum surface for adhesive bonding to polymeric composites," *J. Adhes. Sci. Technol.*, **27** [15] 1625–1640 (2013).

[105] S.G. Prolongo, G. Rosario, and a. Ureña, "Study of the effect of substrate roughness on adhesive joints by SEM image analysis," *J. Adhes. Sci. Technol.*, **20** [5] 457–470 (2006).

[106] C.M. Abreu, M.J. Cristóbal, R. Figueroa, and G. Pena, "Influence of molybdenum ion implantation on the localized corrosion resistance of a high strength aluminium alloy," *Corros. Sci.*, **54** [1] 143–152 (2012).

[107] T. Chen, W. Li, and J. Cai, "Formation of a chrome-free and coloured conversion coating on AA6063 aluminium alloy," *RSC Adv.*, **1** [4] 607 (2011).

[108] X. Li, S. Deng, and H. Fu, "Sodium molybdate as a corrosion inhibitor for aluminium in H3PO4 solution," *Corros. Sci.*, **53** [9] 2748–2753 (2011).

[109] V. Moutarlier, M.P. Gigandet, L. Ricq, and J. Pagetti, "Electrochemical characterisation of anodic oxidation films formed in presence of corrosion inhibitors," *Appl. Surf. Sci.*, **183** [1-2] 1–9 (2001).

[110] J.H. Osborne, "Observations on chromate conversion coatings from a sol-gel perspective," *Prog. Org. Coatings*, **41** [4] 280–286 (2001).

[111] M. Bethencourt, F.J. Botana, M.J. Cano, and M. Marcos, "Advanced generation of green conversion coatings for aluminium alloys," *Appl. Surf. Sci.*, **238** 278–281 (2004).

[112] B. Davó, a. Conde, and J.J. De Damborenea, "Inhibition of stress corrosion cracking of alloy AA8090 T-8171 by addition of rare earth salts," *Corros. Sci.*, **47** [5] 1227–1237 (2005).

[113] F. Mansfeld and Y. Wang, "Development of 'stainless' aluminum alloys by surface modification," *Mater. Sci. Eng. A*, **198** [1-2] 51–61 (1995).

[114] A.K. Mishra and R. Balasubramaniam, "Corrosion inhibition of aluminium by rare earth chlorides," *Mater. Chem. Phys.*, **103** [2-3] 385–393 (2007).

[115] Y.J. Du, M. Damron, G. Tang, H. Zheng, C.J. Chu, and J.H. Osborne, "Inorganic / Organic Hybrid Coatings for Aircraft Aluminum Alloy Substrates," *Prog. Org. Coatings*, **41** 1–6 (2001).

[116] V. Palanivel, D. Zhu, and W.J. Van Ooij, "Nanoparticle-filled silane films as chromate replacements for aluminum alloys," *Prog. Org. Coatings*, **47** 384–392 (2003).

[117] a. Batan, F. Brusciotti, I. De Graeve, J. Vereecken, M. Wenkin, M. Piens, J.J. Pireaux, F. Reniers, *et al.*, "Comparison between wet deposition and plasma deposition of silane coatings on aluminium," *Prog. Org. Coatings*, **69** [2] 126–132 (2010).

[118] L. Calabrese, L. Bonaccorsi, a. Caprì, and E. Proverbio, "Adhesion aspects of hydrophobic silane zeolite coatings for corrosion protection of aluminium substrate," *Prog. Org. Coatings*, **77** 1341–1350 (2014).

[119] V. Dalmoro, J.H.Z. Dos Santos, E. Armelin, C. Alemán, and D.S. Azambuja, "A synergistic combination of tetraethylorthosilicate and multiphosphonic acid offers excellent corrosion protection to AA1100 aluminum alloy," *Appl. Surf. Sci.*, **273** 758–768 (2013).

[120] J.I. Iribarren-mateos, I. Buj-corral, J. Vivancos-calvet, C. Alemán, J. Ignacio, and E. Armelin, "Progress in Organic Coatings Silane and epoxy coatings : A bilayer system to protect AA2024 alloy," *Prog. Org. Coatings*, **81** 47–57 (2015).

[121] T. Materne, F. Buyl, and G.L. Witucki, "Organosilane Technology in Coating Applications: Review and Perspectives," *Dow Corning*, 1–16 (2010).

[122] D. Wang and G.P. Bierwagen, "Sol-gel coatings on metals for corrosion protection," *Prog. Org. Coatings*, **64** 327–338 (2009).

[123] A.S. Hamdy, D.P. Butt, and a. a. Ismail, "Electrochemical impedance studies of sol-gel based ceramic coatings systems in 3.5% NaCl solution," *Electrochim. Acta*, **52** [9] 3310–3316 (2007).

[124] Z. Wang and Y. Yan, "Oriented zeolite MFI monolayer fillms on metal substrates by in situ crystallization," *Microporous Mesoporous Mater.*, **48** 229–238 (2001).

[125] R. Munoz, D. Beving, Y. Mao, and Y. Yan, “Zeolite y coatings on Al-2024-T3 substrate by a three-step synthesis method,” *Microporous Mesoporous Mater.*, **86** 243–248 (2005).

[126] D.E. Beving, A.M.P. McDonnell, W. Yang, and Y. Yan, “Corrosion Resistant High-Silica-Zeolite MFI Coating,” *J. Electrochem. Soc.*, **153** B325 (2006).

[127] D.E. Beving, C.R. O’Neill, and Y. Yan, “Hydrophilic and antimicrobial low-silica-zeolite LTA and high-silica-zeolite MFI hybrid coatings on aluminum alloys,” *Microporous Mesoporous Mater.*, **108** 77–85 (2008).

[128] R. Cai and Y. Yari, “Corrosion-Resistant Zeolite Coatings,” *Corrosion*, **64** [3] 271–278 (2008).

[129] R. Cai, M. Sun, Z. Chen, R. Munoz, C. O’Neill, D.E. Beving, and Y. Yan, “Ionothermal synthesis of oriented zeolite AEL films and their application as corrosion-resistant coatings,” *Angew. Chemie - Int. Ed.*, **47** 525–528 (2008).

[130] Y. Yan, R. Cai, and M. Sun, AMBIENT PRESSURE SYNTHESIS OF ZEOLITE FILMS AND THEIR APPLICATION AS CORROSION RESISTANT COATINGS; US 2010/0119736 A1, 2010.

[131] L. Calabrese, L. Bonaccorsi, a. Caprì, and E. Proverbio, “Adhesion aspects of hydrophobic silane zeolite coatings for corrosion protection of aluminium substrate,” *Prog. Org. Coatings*, **77** [9] 1341–1350 (2014).

[132] L. Bonaccorsi, L. Calabrese, A. Freni, E. Proverbio, and G. Restuccia, “Zeolites direct synthesis on heat exchangers for adsorption heat pumps,” *Appl. Therm. Eng.*, **50** [2] 1590–1595 (2013).

[133] L. Calabrese, L. Bonaccorsi, D. Di Pietro, and E. Proverbio, “Effect of process parameters on behaviour of zeolite coatings obtained by hydrothermal direct synthesis on aluminium support,” *Ceram. Int.*, **40** [8] 12837–12845 (2014).

[134] R.E. Tucker, Surface Finishing Guidebook*, Metal Finishing Magazine*, 2011.

[135] M. Franco, S. Anoop, R. Uma Rani, and a. K. Sharma, “Porous Layer Characterization of Anodized and Black-Anodized Aluminium by Electrochemical Studies,” *ISRN Corros.*, **2012** 1–12 (2012).

[136] A.W. Brace, “Anodic coating formation on aluminum without a ‘barrier layer,’” *Plat. Surf. Finish.*, **96** [9] 22–30 (2009).

[137] M. García-Rubio, P. Ocón, M. Curioni, G.E. Thompson, P. Skeldon, a. Lavía, and I. García, “Degradation of the corrosion resistance of anodic oxide films through immersion in the anodising electrolyte,” *Corros. Sci.*, **52** [7] 2219–2227 (2010).

[138] X.-W. Li, Q.-X. Zhang, Z. Guo, J.-G. Yu, M.-K. Tang, and X.-J. Huang, “Low-cost and large-scale fabrication of a superhydrophobic 5052 aluminum alloy surface with enhanced corrosion resistance,” *RSC Adv.*, **5** [38] 29639–29646 (2015).

[139] R. Liao, Z. Zuo, C. Guo, Y. Yuan, and A. Zhuang, “Fabrication of superhydrophobic surface on aluminum by continuous chemical etching and its anti-icing property,” *Appl. Surf. Sci.*, **317** 701–709 (2014).

[140] A.M. Escobar and N. Llorca-Isern, “Superhydrophobic coating deposited directly on aluminum,” *Appl. Surf. Sci.*, **305** 774–782 (2014).

[141] S. Ji, P. a. Ramadhianti, T.B. Nguyen, W.D. Kim, and H. Lim, "Simple fabrication approach for superhydrophobic and superoleophobic Al surface," *Microelectron. Eng.*, **111** 404–408 (2013).

[142] M. Ruan, W. Li, B. Wang, Q. Luo, F. Ma, and Z. Yu, "Optimal conditions for the preparation of superhydrophobic surfaces on al substrates using a simple etching approach," *Appl. Surf. Sci.*, **258** [18] 7031–7035 (2012).

[143] Y. Zhang, J. Wu, X. Yu, and H. Wu, "Low-cost one-step fabrication of superhydrophobic surface on Al alloy," *Appl. Surf. Sci.*, **257** [18] 7928–7931 (2011).

[144] B. Qian and Z. Shen, "Fabrication of superhydrophobic surfaces by dislocation-selective chemical etching on aluminum, copper, and zinc substrates," *Langmuir*, **21** [20] 9007–9009 (2005).

[145] U.S. Military, *MIL-A-8625F Anodic Coatings for Aluminum and Aluminum Alloys*. 1993.

[146] ASTM, *D 3359 Standard Test Methods for Measuring Adhesion by Tape Test*. 2007.

[147] P. Csokan, "Mechanism of nucleation and electrochemical transport processes in oxide formation during anodic oxidation of aluminum," *Trans. Inst. Met. Finish.*, **51** [1] 6–12 (973).

[148] F. Keller, M.S. Hunter, and D.L. Robinson, "Structural Features of Oxide Coatings on Aluminum," *J. Electrochem. Soc.*, **100** [9] 411 (1953).

[149] G. Bailey and G.C. Wood, "Morphology of anodic films formed on aluminum in oxalic acid," *Trans. Inst. Met. Finish.*, **52** 187–199 (1974).

[150] L.H. Hihara and R.M. Latanision, "Corrosion of metal matrix composites," *Int. Mater. Rev.*, **39** [6] 245–264 (1994).

[151] N. Saleema, D.K. Sarkar, R.W. Paynter, and X.G. Chen, "Superhydrophobic aluminum alloy surfaces by a novel one-step process," *ACS Appl. Mater. Interfaces*, **2** [9] 2500–2502 (2010).

[152] P. Marcus, *Corrosion Mechanisms in Theory and Practice*, 3rd ed. CRC Press, Boca Raton, 2011.